ENABLING A SCALABLE MANUFACTURING APPROACH TO FABRICATE FUNCTIONAL GRADATED POLYMER THIN FILMS

A Dissertation
Presented to
The Academic Faculty

by

Tae Joong Jeong

In Partial Fulfillment
of the Requirements for the Degree
Doctor of Philosophy in the
School of Mechanical Engineering

Georgia Institute of Technology
August 2022

ENABLING A SCALABLE MANUFACTURING APPROACH TO FABRICATE FUNCTIONAL GRADATED POLYMER THIN FILMS

Approved by:

Dr. Tequila A. L. Harris, Advisor
School of Mechanical Engineering
Georgia Institute of Technology

Dr. YongTae Kim
School of Mechanical Engineering
Georgia Institute of Technology

Dr. Suresh Sitaraman
School of Mechanical Engineering
Georgia Institute of Technology

Dr. Carson Meredith
School of Chemical & Biomolecular Engineering
Georgia Institute of Technology

Dr. Alexander Alexeev
School of Mechanical Engineering
Georgia Institute of Technology

Date Approved: July 18, 2022

To my parents (Tak Jeong and Do Hee Kim) and my brother (Tae Won Jeong) for their relentless support

ACKNOWLEDGEMENTS

I would like to thank my advisor, Dr. Tequila Harris, for her endless support both academically and personally throughout my Ph.D. career. It was an honor to work under an adviser who deeply cares for her students. Without her advises, it would have been impossible for me to finish this journey. Also, I am grateful to all my committee members Dr. Suresh Sitaraman, Dr. Alexander Alexeev, Dr. Yongtae Kim and Dr. Carson Meredith for their expert guidance related to this work.

I would also like to thank Dr. Steven Danyluk and Dr. Peter Hesketh for being so generous for allowing me to use their lab facilities. I would like to thank PACE in Georgia Tech for letting me use their high-speed server for expedited computational works. I would like to thank all the members in my laboratory group, especially Dr. Ara Parsekian and Peter Griffiths for sharing their insights and feedbacks to improve my work as well as the two undergraduate students whom I mentored over my Ph.D. career, Elizabeth Spahn and Xiaoqing (Deemo) Yu, who helped me obtain some crucial experimental data. I would also like to thank Guru Raveendran and Dr. Christine Taylor for helping me setup one of the useful lab facilities. Moreover, I would like to acknowledge Kyungbin Lee, Yue Ji and Dr. Eric Shen for their insights on chemical behaviors of the material. Adding on, I would like to thank Rahul Ventakesh on making last minute verification measurements behalf of me. Finally, I would like to thank all my family, friends and Luna for supporting me in various ways.

TABLE OF CONTENTS

LIST OF TABLES

LIST OF FIGURES

LIST OF SYMBOLS AND ABBREVIATIONS

A	Cross-sectional area
D	Diffusion coefficient
dF	Average momentum
F	External body force
G	Thickness of shim
g	Gravitational acceleration
H	Coating gap
H*	Dimensionless length ratio at die lip
I	Unit tensor
J_f	Mass flux going through the face
J_f^*	Resulting face flux
$\widehat{J_f^*}$	Influence of velocity in cells
L	Length
L_u	Upstream die lip length
L_d	Downstream die lip length
$\dot{m}$	Permeation flux
N_{faces}	Number of enclosed cell faces
P_{cn}	Pressure within two cells
Q	Flow rate
Q_1	Center flow rate
Q_2	Side flow rate
S_m	Mass added to continuous phase

t	Time
tD	Diffusion time cover half the flowing width
th_{min}	Thickness of film
th_{wet}	Anticipated wet thickness
V	Substrate speed
v_{avg}	Average outlet velocity
v_f	Flow velocity
Vol	Volume
w	Width of outlet
w_a	Width of advancing film
w_c	Width of flowing channel
w_a*	Dimensionless advancing width
$w_{II}*$	Dimensionless width at start of pinning
$w_{III}*$	Dimensionless width at full pinned
$\frac{\partial c}{\partial z}$	Concentration gradient over z direction
δ_x	Diffusion distance
ρ	Density
μ	Dynamic viscosity
γ^s	Surface energy at solid phase
γ^{sl}	Surface energy at solid-liquid interface
γ^l	Surface energy at liquid phase
σ	Surface tension
χ	Viscosity ratio between center fluid to side fluid
τ	Stress tensor

Π_a Line-of-fit for dimensionless width calculation

SUMMARY

Polymer thin films with a cross-web gradient structure, is a burgeoning area of research, having received more attention in the last two decades, for improvements in performance and material properties. Such patterned films have been fabricated using several techniques, which in practice, these techniques are not scalable, material dependent, wasteful and not highly efficient. In this thesis, the feasibility of using slot die coating, a well-known scalable manufacturing process, to fabricate gradated polymer thin films will be investigated. The proposed work incorporates slot die with custom roll-to-roll imaging system to successfully fabricate gradated thin film by forcing two fluidic materials into the slot die simultaneously and by manipulating the viscous, diffusion and inertial forces. The materials will be allowed to intermix, with the aim of having approximately a 50% mix along the centerline of any two contiguous stripes. Moreover, several characterizations are performed to assess the quality of the gradated polymer thin films. Here, several well-known functional materials are used as part of the gradient structure to fabricate functional gradient structures, which then are used to prove the practicality of such pattern. Furthermore, mathematical analysis is conducted to understand the mechanisms that drive the mixing or diffusion between the materials to form the gradient structures, the limitations on feature size, and the structure-property relationships relative to system inputs. Computational analysis is used to support the experimental results. These investigations will provide a fundamental understanding of the mechanisms that can be controlled to obtain gradated polymer thin films structures that exhibit the desired geometric structure, mechanical properties, and performance.

CHAPTER 1. INTRODUCTION AND BACKGROUND

1.1 Motivation

Recently, gradient thin films have received more interest due to their versatility in a plethora of research fields such as, but not limited to, packaging of flexible electronics[1, 2, 3], controlled cell growth in lab-on-a-chip (biosensors)[4, 5], thin film electrical devices[6] and production of nanopaper[7]. Gradient structures are advantageous because they have been shown to improve the functionality of materials such as the electrical[8,9], thermal[10], adhesive[11] and mechanical[12] properties as shown in Figure 1.1. The enhancements of these properties can be realized by fabricating the gradient thin film such that the gradient interface is formed through the thickness[13,14,15] or along the sidewalls[1-7] of each coated material. These structures can be composed of two or more different materials[6,8,10,11] or by using different concentrations of the same material[1, 5, 12].

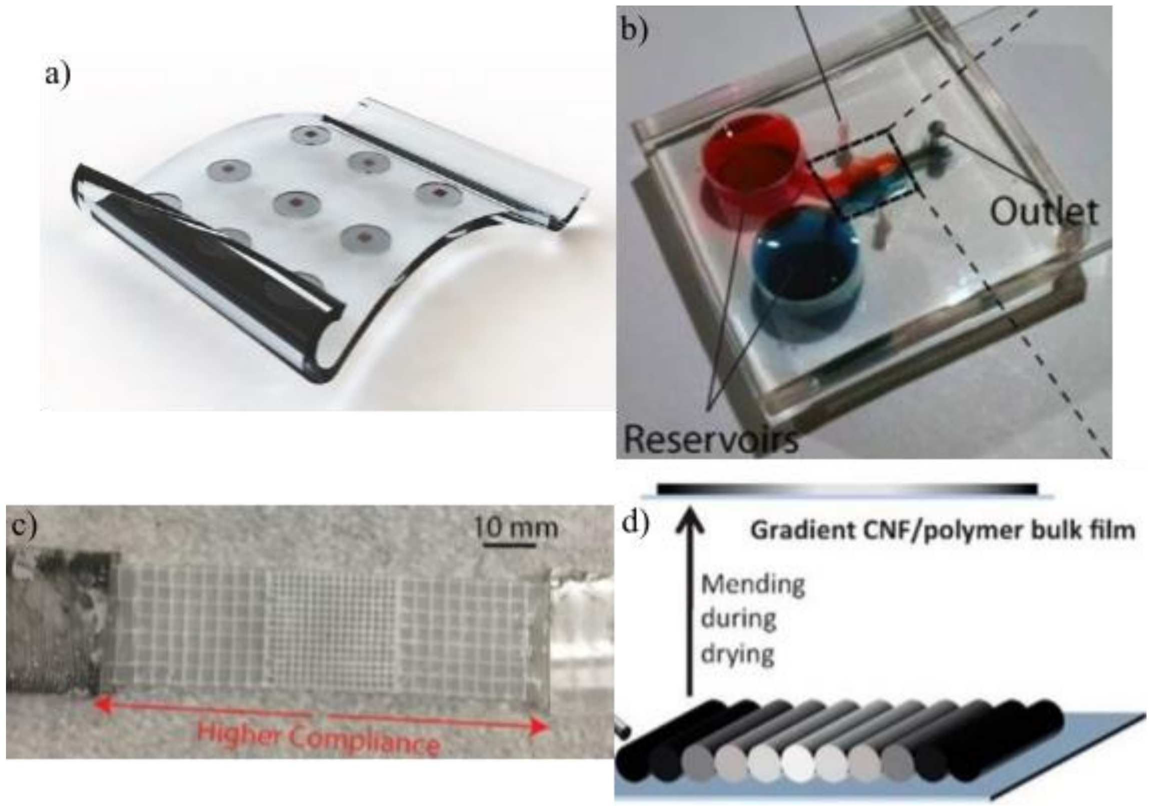

Figure 1.1– Gradient patterned applications including (a) flexible electronics[1], (b) biosensors in form of lab-on-a-chip[4], (c) enhanced thermoplastics scaffolds[5] and (d) strengthened nanopapers[7]

While there exists major benefits for using gradient structures, continuous, cost-efficient scaled fabrication is limited. Coating and printing technologies show promise for scaled fabrication of gradient thin films[1,3,16,17,18]. However, there are limited viable processes for true large-scale manufacturing, hence, more research is required to understand material selection, interfacial mixing and the influence of gradient orientation and production. Elucidating the fundamental science of process-structure-property relationships, of gradient thin films will help establish the knowhow for continuous production of quality gradient thins films.

1.2 State-of-art of Gradient Thin Films and Their Manufacture

1.2.1 Gradient Thin Film Manufacturing

As previously stated, gradient thin films are typically fabricated such that the structure is formed by coating one liquid on top of another (through the thickness) or coating them side-by-side (across web). There are several fabrication methods that have been explored for form these structures, as shown in Figure 1.2. However, each fabrication method and structure have their own set of advantages and disadvantages.

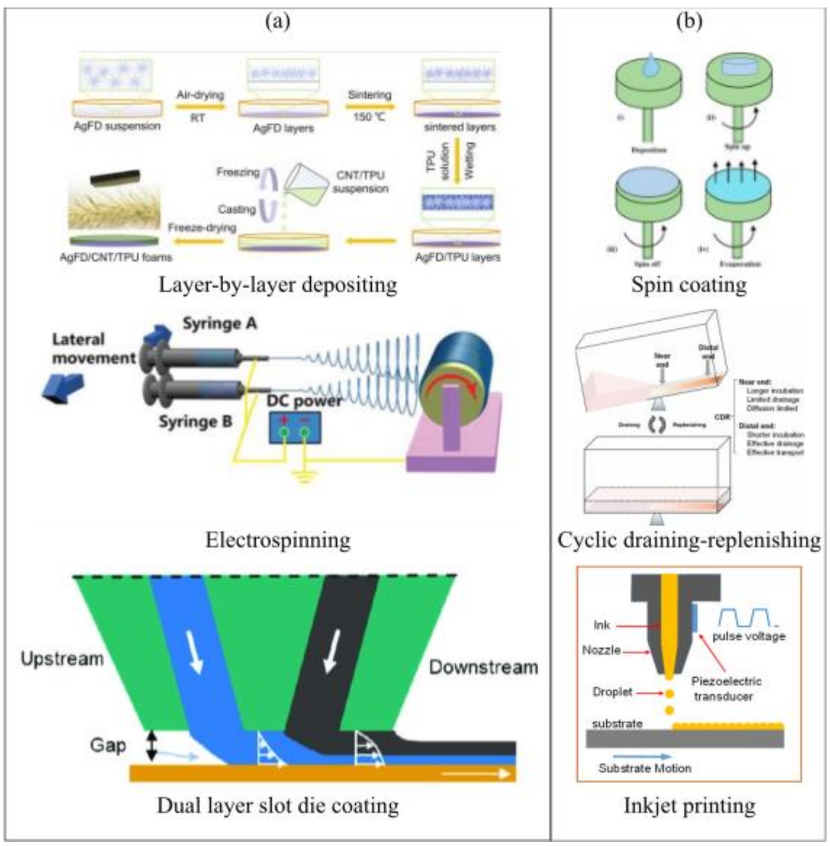

Figure 1.2– Some of known methods for gradient thin film formations (a) through the thickness[8, 14, 19] and (b) side-by-side direction[20,18,21]

Gradient thin films fabricated through the thickness, whereby two or more materials are coated simultaneously through the thickness and allowed to mix along the traverse interface as shown in Figure 1.3. Electrospinning[14,22,23], layer-by-layer depositing[8], spray coating[24] and dual layer slot die coating[9,19], have been used to fabricate traverse gradient thin films. However, these methods have limited scalability and often exhibit gradient non-uniformity through the thickness of the structure, creating more randomness in structure which impact the functionality of the thin film.

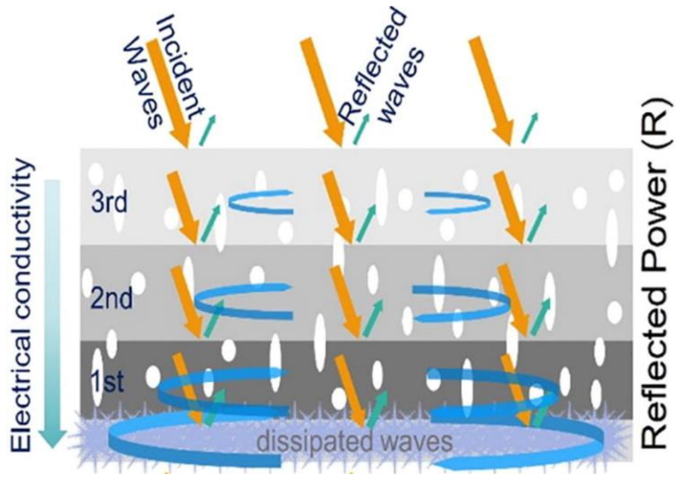

Figure 1.3– Gradient thin films fabricated through the thickness[8]

Electrospinning method in the past has been able to fabricate gradient thin film in two ways: two materials coated simultaneously and coating layer-by-layer. For simultaneous electrospinning method, DC power source was connected to the syringes that move in lateral direction. The power sourced varied the flow rates from 0 mL/h to 1 mL/h to form gradients. The two fluids were directly coated on to the constant velocity substrate for 180 minutes to fully cover the desired coating area as shown in Figure 1.2 (a). Then, the coated film is hot pressed 200°C and quenched to 60°C. From here, it can be noticed that the overall processing time is very inefficient. For electrospinning one material at a time, first material is electrospun on to the substrate using the similar setup to the prior method. However, instead of hot pressing the film, the single material film is plasma treated then the second material is electrospun on to the film fabricated using the first material as shown in Figure 1.4. Then, the overall assembly is baked in the oven 70°C for 2 hours. The coating time is faster than the simultaneous electrospinning method, but there are more processing steps which reduces the scalability and efficiency.

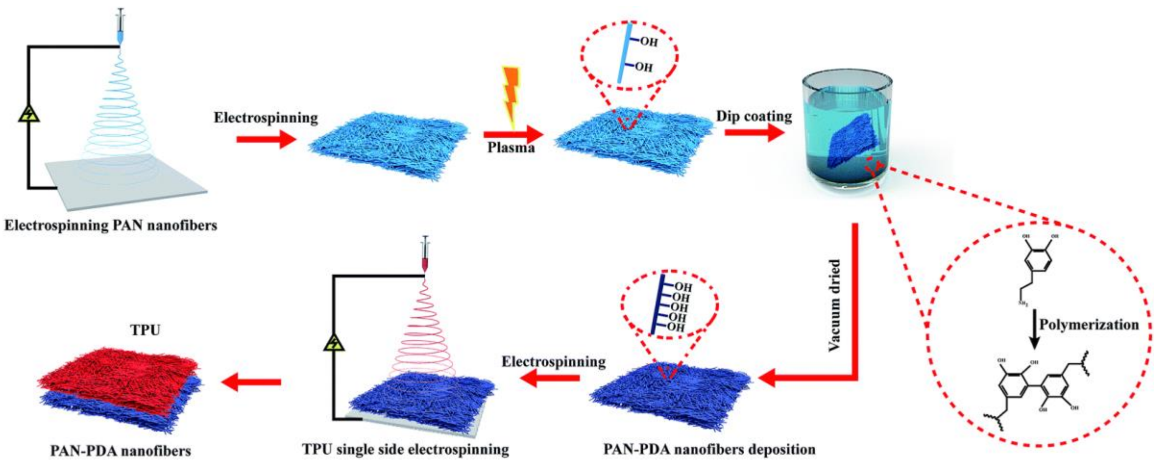

Figure 1.4– Electrospinning two materials in layer-by-layer method to fabricate gradient thin film[23]

Layer-by-layer method in fabricating gradient thin film, as shown in Figure 1.2 (a), follows several complex procedures where the first material is poured onto a mold which is air dried first then sintered in high temperature. After the cooling process, the second material is poured and freeze dried in liquid nitrogen. This step is repeated until the desired thickness. Again, just like the layer-by-layer electrospinning method, this method reduces the overall scalability and efficiency due to complexity in each process.

Spray coating[25] is a well-known coating method that has successfully fabricated gradient thin film through the thickness. Very small volume of fluids is sprayed onto the substrate with random dispersion and the fluids are stacked until the desired thickness. As shown in Figure 1.5, the two materials are simultaneously spray coated on to the substrate on a heating platen for instantaneous drying of the very thinly coated layer[24]. By controlling the material, the gradient pattern can be formed. However, spray coating does not allow for instantaneous coating and due to the randomness in dispersion, the coating is not uniform[26].

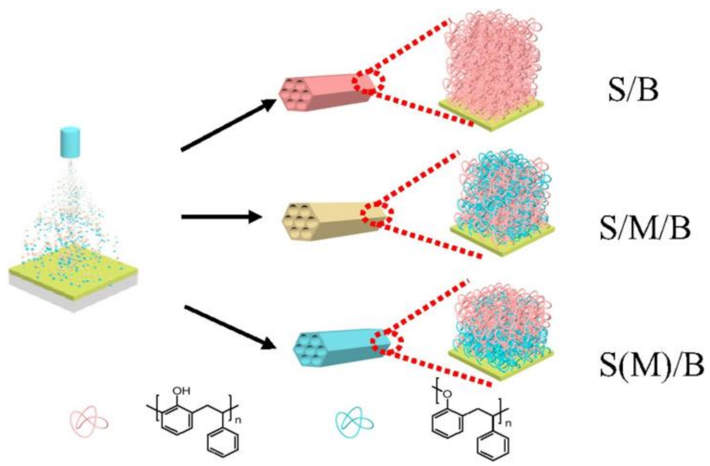

Figure 1.5 – Spray coating method to fabricate gradient structure through the thickness[24]

Dual layer slot die coating is scalable manufacturing method that can stably coat two layered thin film simultaneously. In previous work, such method was used to produce a binder adhesive for multilayer electrodes as shown in Figure 1.2 (a). The two fluids are introduced to the designated thin chamber where the fluids would meet at the deposition. The moving web is the substrate where the fluids are deposited on to. The slot die coating has capability to easily change the coating parameters which include coating gap, substrate speed and flow rate to produce different gradient film dimension and to avoid any coating defects.

Alternatively, there are gradient thin films that are fabricated side-by-side, using methods such as spin coating[1], inkjet printing[16], 3D printing[3], filament writing[7], photolithography[4, 17], cyclic draining-replenishing (CDR) method[18] and slot die coating[27]. Each of these methods, when forming side-by-side gradient structures, has its own pros and cons.

Spin coating[28,29] uses centrifugal forces to evenly distribute the fluidic materials on the desired surface quickly. When fabricating gradient structure, first material is spin coated then the second material is coated with a wafer handle to control the location of the coating[1] as shown in Figure 1.6. However, this method has high material waste[30] with complex processes and it is very hard to form instantaneous gradient pattern[31].

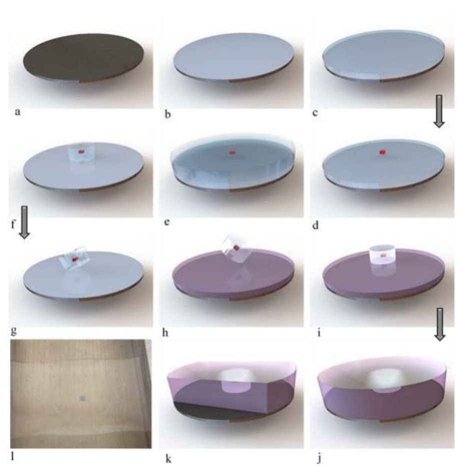

Figure 1.6 – Step-by-step process of gradient thin film fabrication using spin coating[1]

Inkjet printing[32] is digital coating technology that allows for efficiently coating gradient thin film in a specific pattern. To fabricate gradient patterns, droplets are randomly dispersed onto the substrate and the graphics program commends the overall printing process. The two materials are then allowed to intermix on the substrate[16] as shown in Figure 1.7. However, because the wet film is formed by multiple randomly dispersed droplets, the film itself is not perfectly uniform[33,34].

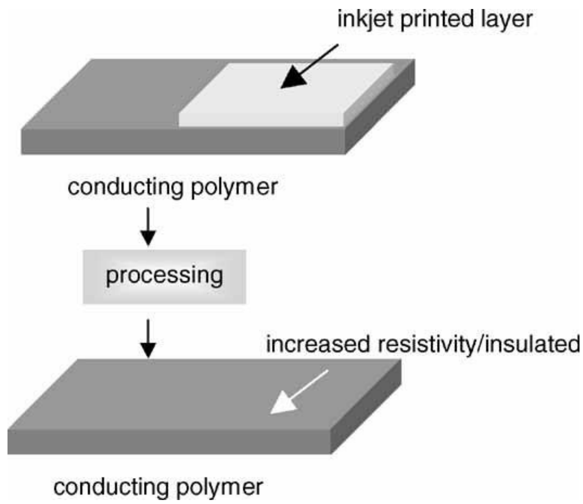

Figure 1.7 – Inkjet printing method to fabricate gradient thin film[16]

3D printing is another computer integrated method which the size and number of nozzles can be customized to fabricate gradient thin films. As it utilizes CAD software, the dimension of resultant film is very precise and using printing software, the flow rate can be easily controlled. Moreover, the materials can be easily interchanged which adds onto its scalability[3]. However, the 3D printing method still has limitation in obtaining uniform film due to the distribution of the materials which results in porous and inhomogeneous film[35].

Photolithography[36] is a method that is mostly used in the biosensors where it utilizes exposes light through photosensitive polymer to selectively dissolve the desired pattern to the substrate. As shown in Figure 1.1 (b), the two photosensitive materials are flowed through into a patterned gasket formed by assembling photomask, photoresist and silicon wafer[4]. This method is instantaneous and easy to use, however, it is expensive, limited to certain materials and enclosed to a rigid geometry[37].

CDR method is not so well known which drops fluid on the substrate as large droplets and rotate the tool to obtain the desired gradient structure. The fluidic material fills the large cavity first which then is tilted to drain the fluids and the remaining fluids are then cured. This step is repeated until the desired pattern in achieved. However, this is very lengthy process and the tool itself is very large which reduced the overall efficiency[18,38]..

Slot die coating is a well-known coating method that has also been utilized to form gradient thin film. Two large blocks encase a very thin shim with a flow pattern then the assembly is mounted on a roll-to-roll system equipped with constant velocity web and controlled flow rate pump. In the previous work, the author attempted to fabricate alternating striped film using two materials. The alternating stripe patterned film is fabricated with special patterned shim with multiple inlets on the downstream die to have two or more fluids entering the cavity in alternating fashion as represented in Figure 2.3. Although very marginal, diffusion was noticed at the interface of the two materials as shown in the call out image from Figure 1.8. The coating production was instantaneous, and the manipulation in flow rates of the two fluids were very easy. Moreover, this method allowed for a mass production of the thin films and very cost effective. Slot die coating, however, has a clear disadvantage in material selection as coating fluids with low wettability on substrate materials are very hard to be processed[27].

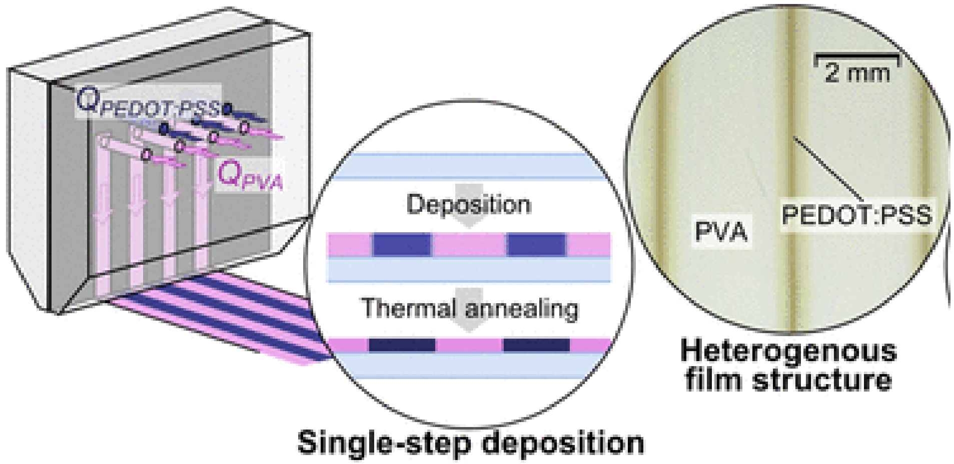

Figure 1.8 – Alternative stripe patterned thin film fabrication using slot die coating[27]

Looking at all the possible methods, there lacks a method that is highly scalable, very cost-efficient and forms uniform instantaneous gradient thin films. Out of the methods mentioned above, slot die coating seemed most promising at it contains all three characteristics in forming gradient formation. However, there is still potential room for improvement as previous study with slot die coating only showed very minimal gradient structure between the two fluidic materials.

1.2.1.1 Slot Die Coating on Roll-to-Roll (R2R) System

Slot die coating[39] is a well-known scalable manufacturing method for fabrication of thin film coating that can reduce the common deficiencies in other coating methods mentioned in section 1.2. The infrastructure and parameters of slot die coater is critical in fabrication of thin film patterns. A slot die coater is a three-piece structured tool, which a thin shim is tightly bounded by two large die blocks which are the downstream and upstream dies. The shim design decides the fluidic behavior as certain designs can alter the overall film pattern formation which is one of the reasons why slot die coating method has large window of scalability. Previous works have successfully designed such internal flow geometry that allowed for uniform coating[40,41], dual layer coating[42] and alternating stripe patterned films[27,43]. For uniform coating, the size of the slot die and shim can be dependent to the user's demand but customization of shim allows for easier scaling as shown in Figure 1.9. For dual layer coating, an additional shim and die block are added to induce cavity for extra layer and an inlet on each die block is attached for each material as shown in Figure 1.10. Moreover, the material of the overall infrastructure can be changed so that it is compatible with the fluidic material.

To have the slot die coating method to continuously produce uniform film, a R2R system equipped with controlled velocity carrier web and constant flow rates is needed. The system has a feed roller and a take-up roller which creates the tensioned carrier web from the roll of substrate material that is equipped at the feed roller. The motor precisely controls the speed of the take-up roller so that the substrate velocity (V) is constant. The flow rate (Q) is constantly controlled using the pump with a fluid filled syringe and the number of pump and syringes can vary with the number of fluids. These tools can control the speed of coating, the volume of the fluid being coated and materials can be changed which further helps the scalability of the method. The R2R system also can have extra infrastructure, such as pre- and post- treatment devices, to further improve the coating quality, as shown in Figure 1.4. For example, heating platens can be added at the post coating stage to instantaneously dry the wet films and surface treatment tools such as corona treatment, plasma treatment and ultraviolet (UV) treatment can be added prior to coating to improve the wetting of a fluid(s) on to the substrate. Moreover, high resolution microscopes can be installed to capture the image at the internal flow and deposition phases.

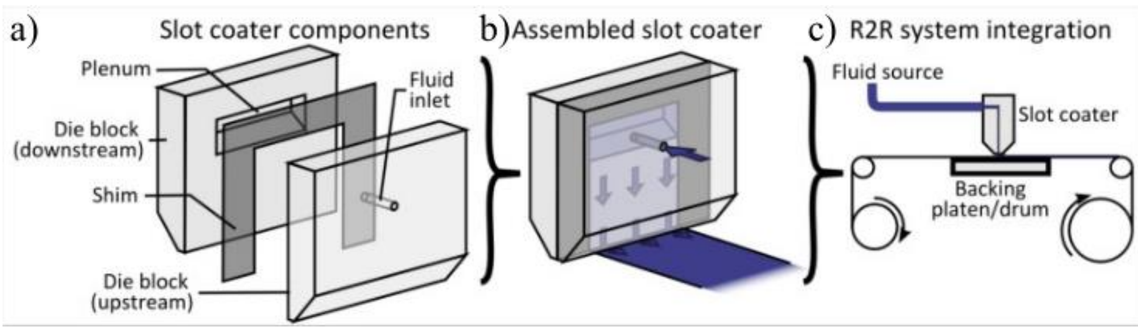

Figure 1.9 – Single layer slot die coating method with (a) exploded view of infrastructure, (b) isometric view and (c) implementation on R2R system[44]

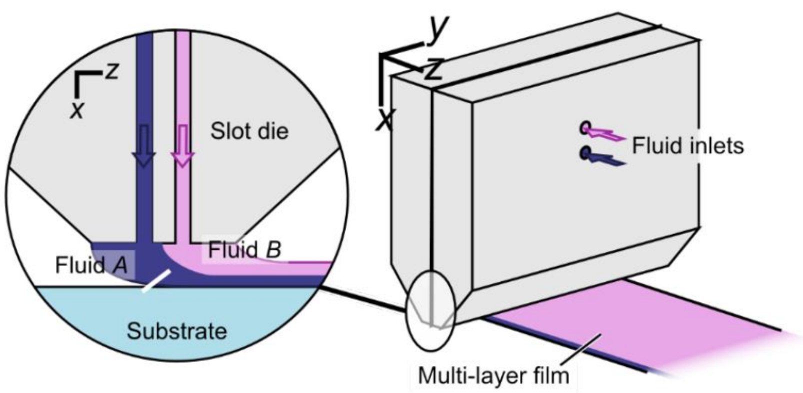

Figure 1.10 – Dual layer slot die coating method[44]

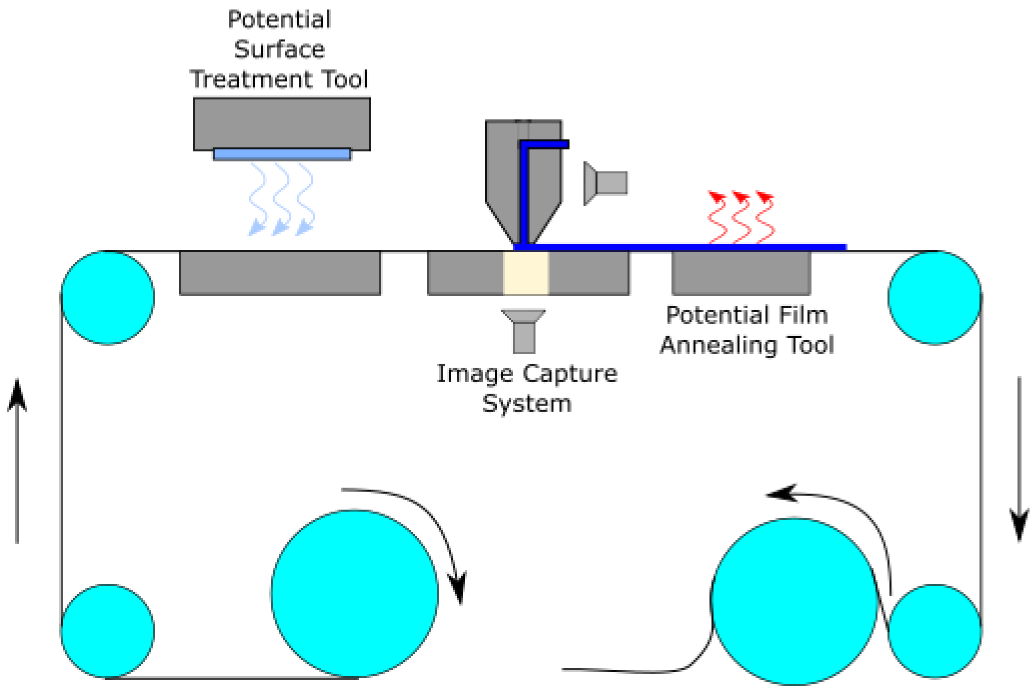

Figure 1.11 – Potential expansion of the slot die coating method mounted on R2R system

1.2.2 Mixing Mechanism in Microfluidics

In the field of microfluidics, mixing can occur largely in two forms: active mixing and passive mixing. Active mixing requires external forces that can agitate the fluids to mix completely. One can think of stirring two materials using a stirring rod as active mixing. However, in microfluidics, sources like acoustic[45], thermal[46, 47] and magnetic actuators[48, 49, 50] are required for mixing materials within the microchannels. Although past efforts have succeeded in gradient formation using active mixing, they require extra apparati, which adds complexity to the overall process.

Conversely, passive mixing does not require extra apparati, as simple flow through patterned channels can induce mixing, with the assistance of microscopic diffusion of two materials. Hence, channel design is very important in passive mixing as it dictates the level of mixing that will occur. Some well-known microfluidic channel geometry includes T-junction[51], Y-junction[52] and flow splitter[53, 54]. However, these geometries have some limitations in terms of flow rate and viscosity[55]. Passive mixing of microfluidics can be depicted in flow through planar geometry, where the thickness and width of the flow channel is on the micron scale. Of note, Cubaud et al.[56, 57] used a fork shaped flow channel constrained, rigid and engraved channel, to investigate instantaneous mixing. Furthermore, they used Peclet Number (Pe) to predict mixing inside a micro channel.

Mixing induced by microfluidic channels has been well demonstrated. However, such phenomenon is yet to be practically applied especially in the field of thin film coating meaning that the microfluidic behavior observation outside the flow channel is unexplored. Also, investigation in the quality and dimension of resultant gradient structure is still needed.

1.2.3 Computational Fluid Dynamics (CFD)

Predicting and verifying experimental results using computational tools is important for improving the cost and time efficiency. Results from computational fluid dynamics (CFD) simulations can be good precursors as they strictly follow the mathematical governing equations. For fluidic behaviors, CFD analysis are used to predict and verify the results. Some notable CFD programs are ANSYS® Fluent[58] and COMSOL®[59] which both have capability of not just looking at single fluidic flow behavior but also the mixing behavior of multiple fluids[60, 61, 62]. However, gradient formation of multiple fluids through a planar geometry was not investigated. The two methods mentioned above have their own pros and cons that allows the user to choose which software to be used. COMSOL® is a very user-friendly tool that can quickly obtain simple fluid behaviors compare to ANSYS® Fluent, but the latter software has ability to obtain more accurate results using its capability to control the mesh elements of the geometry. CFD ACE+® is used to inspect microfluidic mixing of two materials though thin channel[63] and in different work[64], ANSYS® Fluent 6.3 has been used previously to look at fluidic behavior of single fluids at deposition phase of slot die coating. However, to date, there has not been studies that coupled the mixing of two fluids at the internal phase and be carried out to the external deposition phase especially for gradient structures. The result from CFD will be very crucial as it will be a precursor to whether the gradient patterned coating will be formed or not.

1.3 Thesis Scope

1.3.1 Research Objectives and Key Questions

1.3.1.1 Research Objective

The objective of this work is to understand the mechanisms that influence the fabrication of gradient thin film structures that exhibit the desired geometric structure, mechanical properties, and performance using a slot die coating process with integrated passive mixing to explore scaled coating of these materials. Here, experimental and computational analyses are conducted to complete the work following Figure 1.9. The experimental investigation is conducted with an acrylic slot die embedded on a R2R setup that has imaging capabilities to visualize the formation of the gradient in both the internal flow region and the deposition region. The experimental results are validated against CFD results.

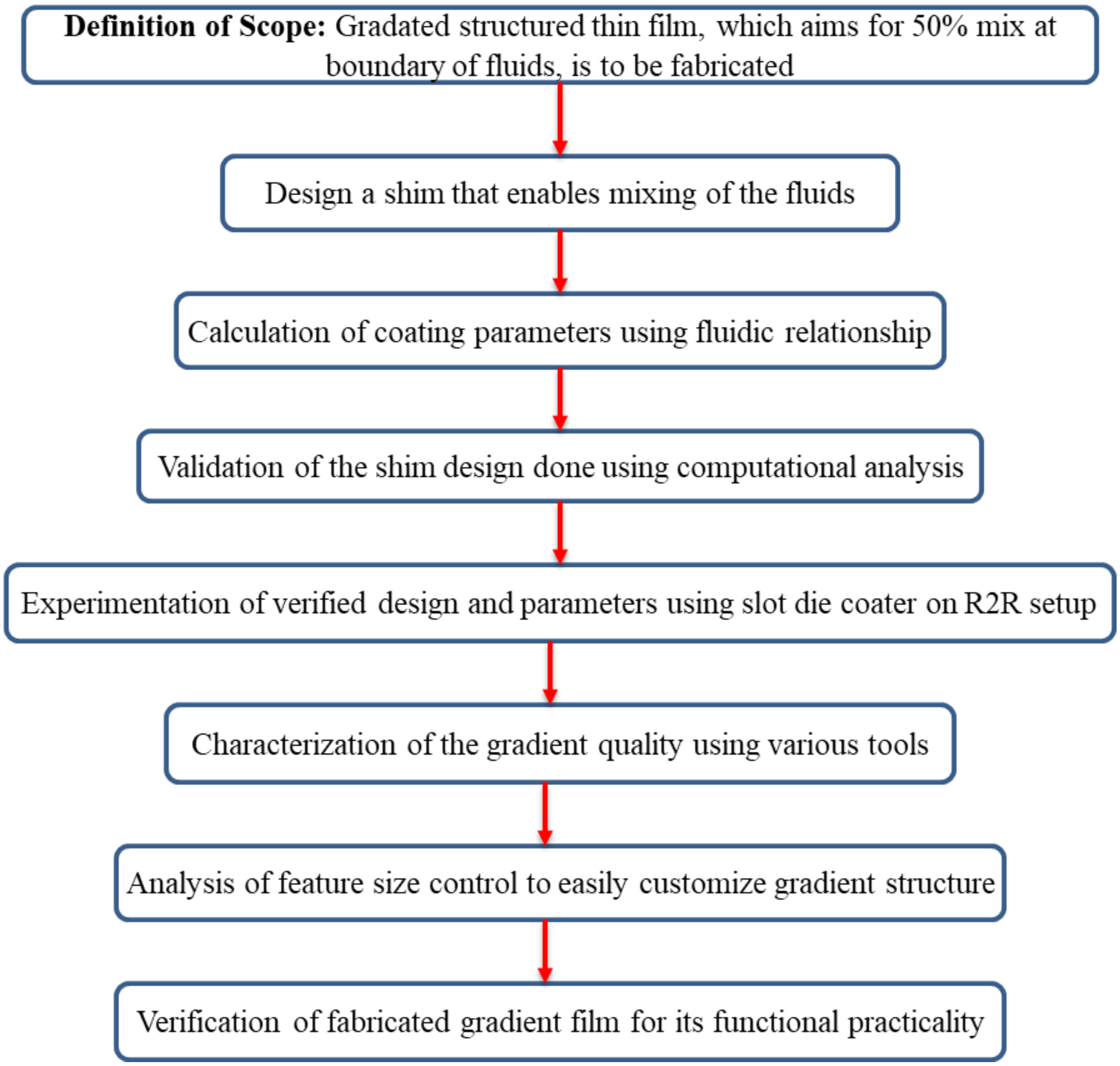

Figure 1.12 – Step-by-step process followed in the dissertation

The influence of the flow channel geometry is analyzed to understand the flow behavior in relationship to the geometry of the channel cavity. This knowledge allows for alteration in feature sizes of the resultant gradient thin film. The aim of the work is to fabricate the gradient thin film using a slot die on a R2R to achieve approximately 50% mix at the centerline as shown in Figure 1.13.

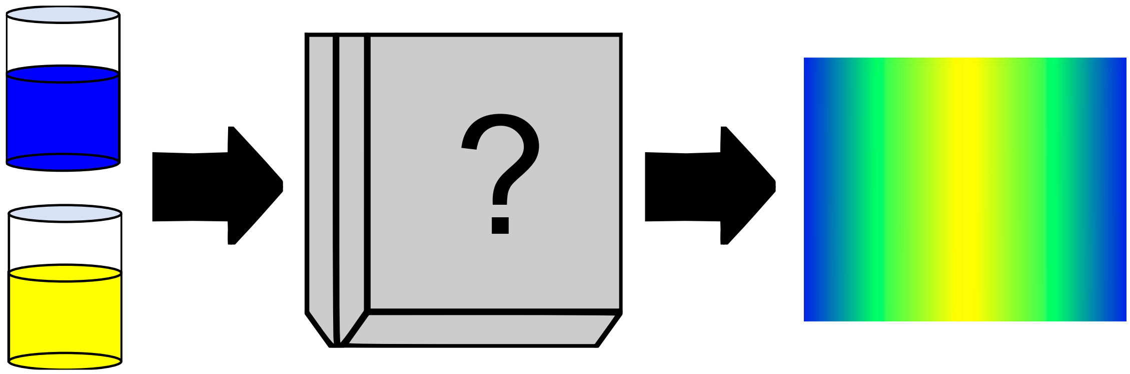

Figure 1.13 – Simple schematic of this dissertation's main objective

2D and 3D CFD analyses, using ANSYS Fluent 17.0 are conducted to understand the mechanisms that lead to mixing internally, limitations on feature size and structure-property relationships relative to system inputs. The mixing observed internally, which mimics passive mixing in microfluidic devices, informs what should be expected as a first approximation in the coating bead or deposition region. This helps control the pattern of the deposited gradient thin film.

1.3.1.2 Key Questions

Key questions that are addressed to fundamentally understanding how gradient structures can be formed using slot die coating with integrated passive mixing on a R2R include:

1) What mechanism(s) drives the formation of a gradient inside the slot die and maintain it at deposition?

2) What mechanism(s) control of the overall dimensionality of the mixed regions exiting the slot die to form a coated thin film?
3) What influences the gradient structure downstream?
4) How does the fluid at the deposition region effect the gradient structure fabrication?

1.3.1.3 Anticipated Contributions

This work is significant because current processing methods to fabricate gradient thin film structures are not highly scalable. Slot die coating on the R2R system is poised to provide an alternative approach to scaling up gradients thin film structures, with precise control over the film structure, thickness, and width. In this work, we introduce a manufacturing process with passive mixing to scale up the fabrication of gradient structures. Here, we investigate the internal mixing phenomena and the flow dynamics within the coating bead to precisely control the geometry and morphology of the deposited thin film, which has led to the following fundamental and applied contributions:

1.3.1.4 Fundamental

1. Provide geometrical relationship of the fluidic passage to control the resultant coating sizes with correlation to rheological properties and processing parameters.
2. Provide an understanding of the fluidic behaviors at thin channels and behaviors at the deposition phase, especially spreading during the formation of gradient structures.

1.3.1.5 Engineering

1. A method for roll-to-roll fabrication of gradient structures to enable scalable processing with control over the resultant geometry.
2. Demonstrate the functionality of gradient films in various fields by verifying its mechanical and electrical properties.
3. Gradient structured film of functional materials can be useful on developing interesting structures, in electrical and biological fields to be used in different applications, that have reduced delamination and longer life.

1.3.2 Organization of Thesis

The thesis follows as mentioned below:

- Chapter 2 provides details on the overall process and materials for initial forming gradient patterns using slot die coating on R2R system
    - The overall infrastructure of the slot die coater as well as the shim design and its fabrication method
    - The details on the materials used for the coating system and fluids for the initial experimental verification
    - Detailed explanation of CFD processes to verify the designed shim
- Chapter 3 investigates complete steps in producing the gradient film via slot die coating with same fluid with different concentrations.
    - Calculations are done to find the exact coating parameters to coat the gradient thin film.

    - Further exploration of the concentration difference between mixed fluids are done to find the limits.
    - Fabricated gradient structure is mechanically and electrically characterized to prove its usefulness.
- Chapter 4 explores the study further to the CFD analysis to verify the experimental results so they can be used as precursors.
    - Detailed description of the method, governing equation and user defined settings provided through the program
    - Thorough comparison of 2D and 3D results to the experimental data for verification of results
- Chapter 5 deepens the research by looking at the gradient structure using functional materials as the fluid but using the same infrastructure.
    - The details on the important material properties of the selected functional fluidic materials. Using those values, coating parameters are calculated based on the equation and results from previous runs.
    - The resultant gradient patterned films are mechanically, electrically and microscopically characterized to verify the molecular existence and usefulness of the gradient structure.
- Chapter 6 proposes a potential characterization method that can visually capture the location of the thin film that is most vulnerable to axial stress
    - The details on the mechanism of the novel characterization and its structure

    - Utilization of the tooling on the uniform single material slot die coated thin films on emulated electronic devices
    - Possible ways to expand the method to be utilized on to the gradient thin films
- Chapter 7 investigates the empirical analysis of the fluidic behavior during the gradient formation
    - The review of previous works on mathematic analysis of microfluidic gradient formation to understand the reason of such phenomena.
    - The difference between mixing and diffusion to verify the status of the formed gradient structure
    - The mathematical understanding of how internal flow behavior is changed or maintained at the deposition phase.
- Chapter 8 concludes the overall work by summarizing the key findings of the dissertation
- Chapter 9 specifies the contribution this work can make and the future work it can expand to.

CHAPTER 2. PROCESS AND METHODS

2.1 Slot Die & R2R System

The slot die coater is structured so that a thin shim is bounded by two cavities (or narrow slots that extend the length of the slot die). The design of the shim controls the internal channel of the fluid flow. Of the two slots, the downstream slot is housed with three luer-lock inlets, which connect to three reusable polytetraflurorethylene (PTFE) syringes that hold 25 mL of solution each, via black rubber tubes. The syringes are connected to electrical syringe pumps that digitally control the flow rate.

The R2R system consists of velocity-controlled PET carrier web, volumetric syringe pumps equipped with syringes, and a vision system. As shown in the callout image of Figure 2.1, important coating parameters such as coating gap (H), fluid flow rate (Q) and velocity of PET substrate (V) can be adjusted for different materials and shim design. To depict the quality of the coating instantaneously, a high-resolution camera and microscope are located in front of the slot die to capture images of the internal flow, as shown in Figure 2.1. A second camera and microscope, also illustrated, is positioned in front of the slot die to image the flow of the fluid internally.

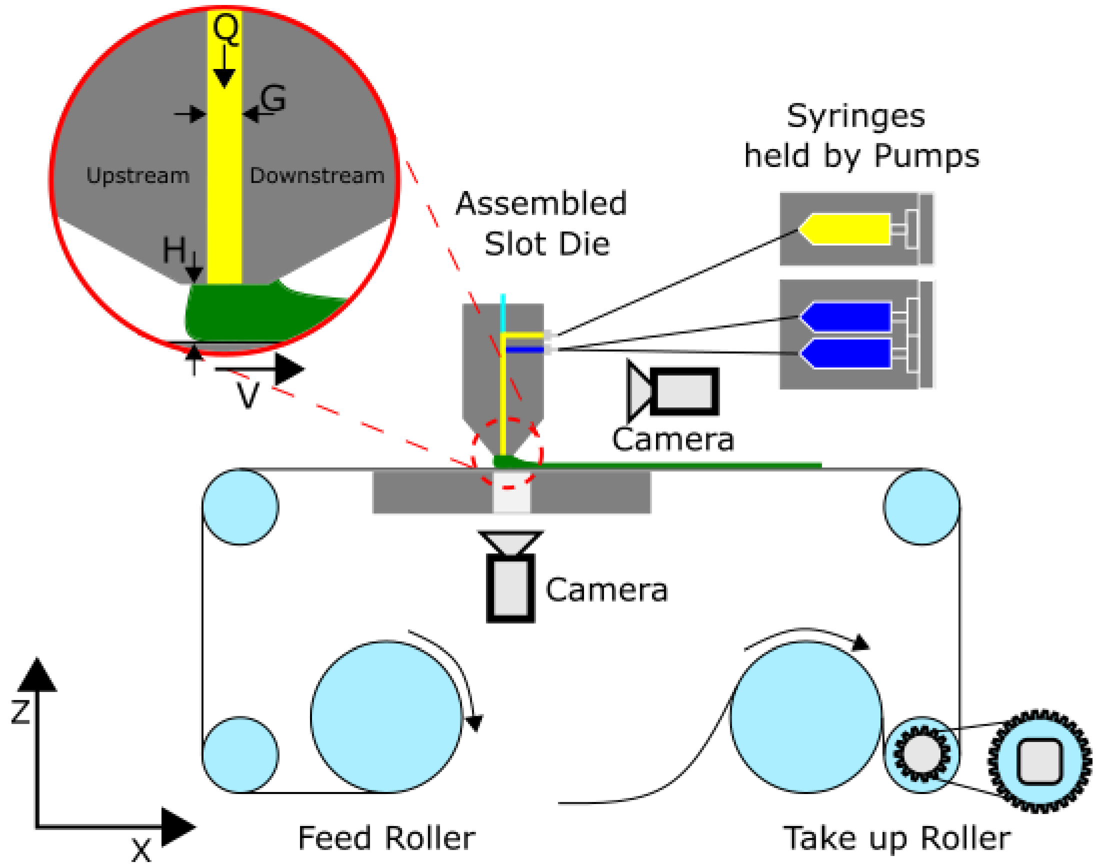

Figure 2.1 – Overall schematic of gradient structured thin film using slot die coating mounted on R2R system.

2.2 Shim Design and Production

The shim is designed based on research regarding gradient formations in microfluidic devices conducted by Cubaud et al.[56]. A vinyl cutter, Cricut Explore Air®, is used to precisely cut the shim after capturing the design in using a user-friendly illustration software called, Inkscape®. As shown in Figure 2.2, the designed flow cavity consists of total of four microchannel with width of 0.2 mm. The multiple microchannel are present to induce more mixing which can be the factor that decide the overall width of gradient region. Such introduction of microchannel aids diffusion to occur as past work has shown that when immiscible fluids pass through sudden constriction of fluids, the flow particles separate themselves to a nanoscale bubble-like form, where multiple fluids can induce the diffusion [65]. For miscible fluids, although the author used active mixing, sudden introduction of microchannel was also utilized for mixing of two fluids. As the fluids pass through the microchannel, the overall flow pattern changes to a semicircular pattern which increases the contact area of the two fluids to allow mixing to occur[66]. Moreover, in theory, when the flow channel expands rapidly after the constriction, flow separation occurs which creates a vortex like recirculation and tendency of turbulence in laminar flow[67]. The overall outlet width is set as 1 cm, which is the desired overall width of the gradient film but is subject to change following the fluidic behavior at the deposition phase.

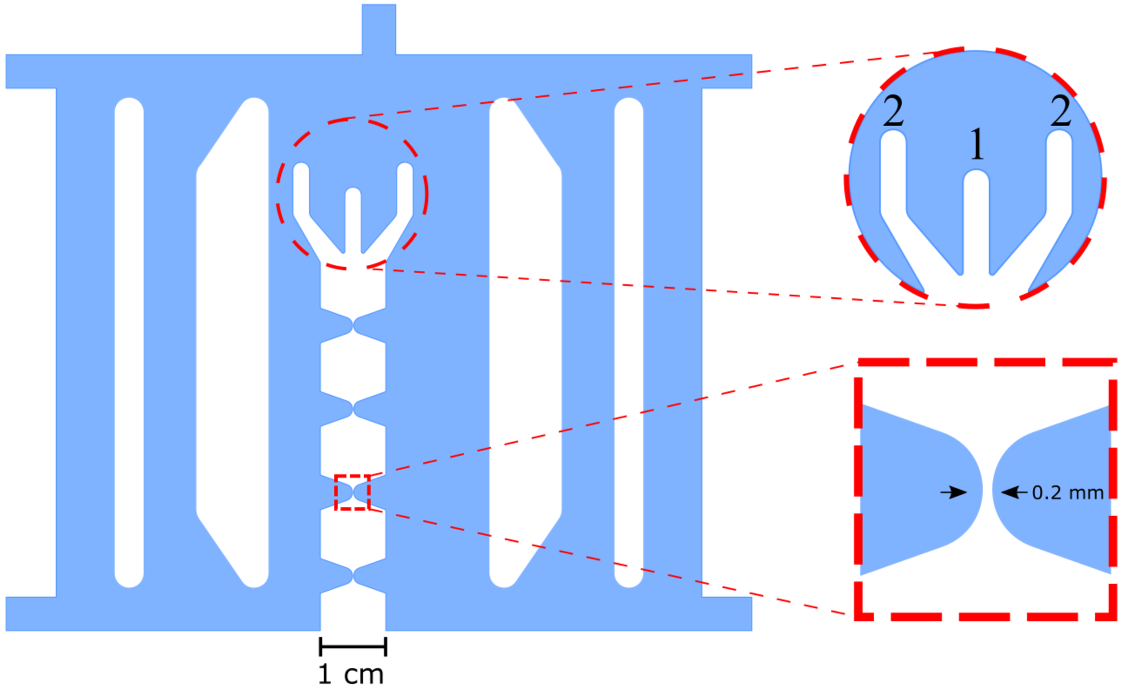

Figure 2.2 – Detailed view of the shim design

As mentioned above, Fluid 1 is introduced in Inlet 1 with flow rate of Q_1 and Fluid 2 is introduced to the two side inlets labeled, Inlet 2, with flow rate of Q_2. On the shim geometry, other empty geometries other than the flow cavity are spaces for dowel pin and screws that that would tightly enclose the two slot die halves with the shim placed between them. The slot die with the cut shim is assembled tightly using twelve (screw size) screws and bolts with two dowel pins in holes near the center to fasten the overall assembly, as illustrated in Figure 2.3. The assembled slot die is then mounted onto the R2R system using two screws, as shown in Figure 2.3 (a), (b) and (c).

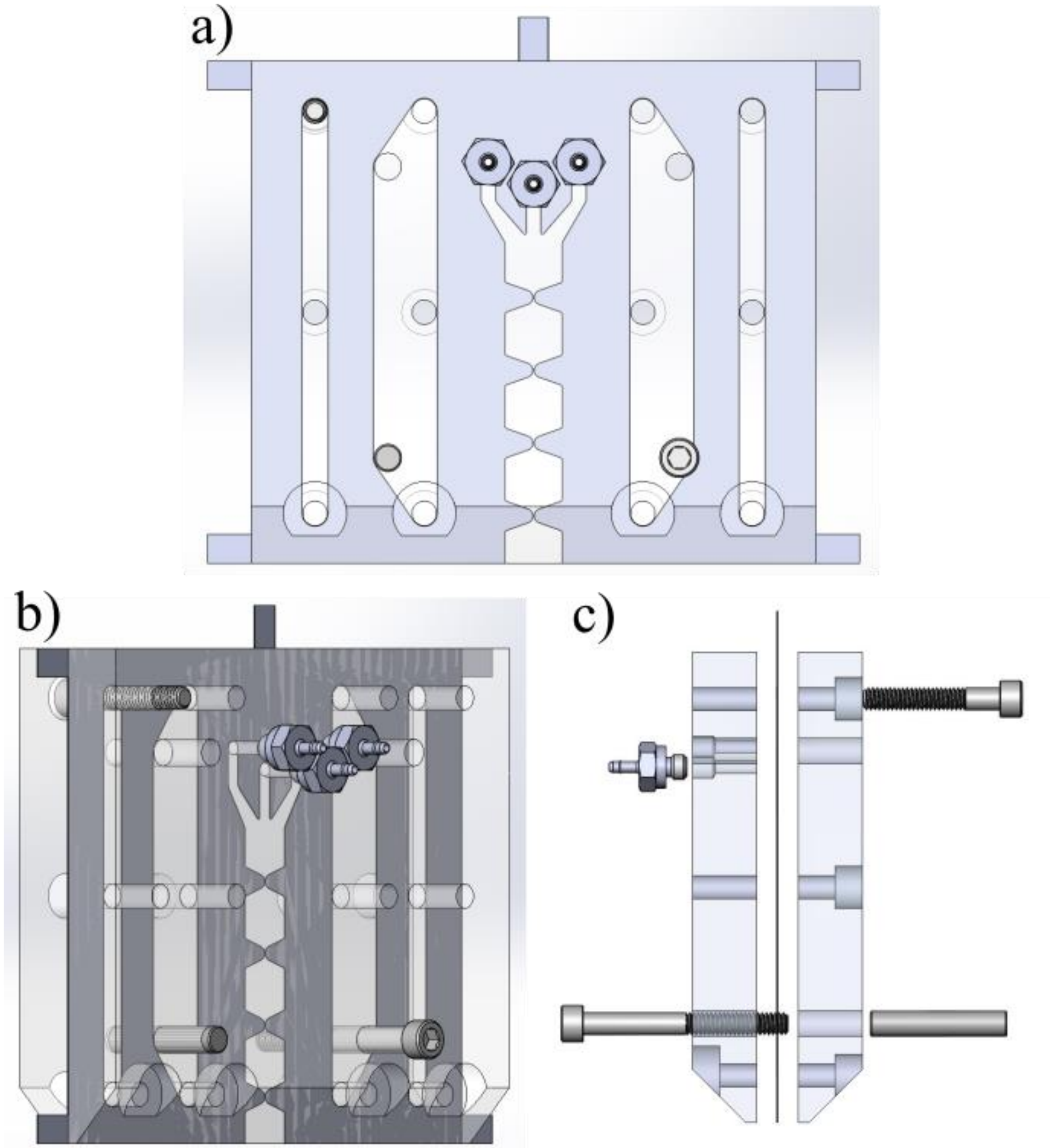

Figure 2.3 – Detailed view of the assembled slot die showing the (a) front view, (b) isometric view and (c) side view.

2.3 Material Selection

2.3.1 For Slot Die, Shim and Substrate

The tooling used for the slot die coating method has to be made of a compatible material that is compatible with the coating fluid(s). Since the solvent is water, a wide range of materials such as stainless steel, aluminum and polymethyl methacrylate (PMMA or acrylic) can be used. Here, PMMA is chosen as the material for the slot die plates, due to its transparency, which is required to visualize of the internal flow phenomena. The shim, thin plate placed between the two slot die halves along the perimeter to create and desired offset distance and the microchannel pattern that will promote mixing, is made of polyethylene terephthalate (PET). The shims are PET sheet, purchased from unknown vendor, which are 127 μm and 76.2 μm in thickness. A roll of 100 μm thick PET film, ES301400, purchased from Goodfellow LTD is used as the main carrier web on the R2R system.

2.3.2 Fluids and Material Properties

Poly vinyl alcohol (PVA), specifically Mowiol 4-88 purchased from Sigma Alderich Corp., is used as the primary polymer for the fluid formulations, because of its versatility in altering the viscosity, high chemical resistivity, and high barrier property. Feasibility of viscosity alteration for PVA is mainly because the material itself is water soluble. Aqueous solutions are prepared by dissolving certain mass of PVA crystals in a larger mass of Deionized (DI) water using hot plate equipped with magnetic stirrer in 60°C until crystals are fully dissolved. The masses of PVA crystals and DI water are decided by the weight concentration. Different weight concentrations are prepared so that gradient thin film is fabricated using different combinations. The maximum concentration is chosen as 20 wt.% PVA as higher concentrated fluid can cause viscous effect and the concentration is decreased by 5 wt.% until 5 wt.% for easy processing and distinct difference in material properties. The property details of PVA used in the experiments are shown in Table 2.1. To pictorially qualify the gradient coating, yellow food coloring (FD&C Yellow 5) is added to the center fluid and blue food coloring (FD&C Blue 1 and Red 40) is added to the side fluids where a drop of food coloring was added for every 2 mL of the PVA. All the food dyes were McCormick® Assorted.

Table 2.1 – Fluidic properties of different fluidic solutions used at standard room temperature (20°C) and pressure (1 atm)[68]

Fluid	Density, ρ, (kg/m^3)	Viscosity, μ, (kg/m-s)
5 wt.% PVA	1010	0.007
10 wt.% PVA	1020	0.040
15 wt.% PVA	1030	0.200
20 wt.% PVA	1045	0.800

Wetting and surface properties of the fluidic materials are crucial to slot die coating as they can predict material-material interactions, be them fluid-fluid or fluid-solid, which is important during a coating process. According to Young's equation, the spreading of a fluid droplet on solid surface can be estimated using the surface tension and the static contact angle as shown[69] in Equation 2.1. Good wetting behavior is noticed when the contact angle between the fluid and the substrate is low and when the fluid surface tension is lower than that of the substrate surface energy. The contact angle of a fluid droplet on the surface material shows the wettability of overall fluidic material to the solid. At angles higher than 90º, it is the surface material is considered hydrophobic and non-wetting. At the contact angle lower than 90 º, the surface material is hydrophilic, however and either exhibit good wetting or non-wetting, especially at values above 60º. Hence, contact angles measurements alone do not dictate wetting, even so, lower angles are always preferred[70,71]. Lower surface tension is preferred as it interferes with wetting and mixing as well[72,73]. Surface tension shows the attractive force of the materials, which determines both the wetting and the mixing of the materials, where lower values are more favorable.[74]

$$\gamma^{s} = \gamma^{sl} + \gamma^{l} cos\theta \qquad (2.1)$$

where, γ is the surface energy at solid surface (*s*), solid-liquid interface (*sl*) and liquid surface (*l*).Contact angle measurements and surface tension measurements are made using a Ramé–Hart Goniometer (Model 500-U1) in ambient conditions. Contact angle measurements are obtained by dispensing 4 µL of solution materials on the surface materials including slot die and substrate, following the ASTM D7334-08 standard. Surface tension measurements are obtained by dispensing 4 µL of the fluid material in pendent droplet form, following the DIN 55660-3 standard. DROPimageAdvanced™ is used as peripheral program to capture and analyze the two properties.

As shown in Table 2.2, the contact angles of both 5% and 10% PVA are higher on the substrate material (PET) than on the slot die material (Acrylic). Although more viscous fluids have lower surface tensions, the viscosity has very minimal effect on surface tension[75]. Previous work also compared the surface tensions of 10% wt. PVA and 24% wt. PVA aqueous solutions,[50] which showed that even with large difference in their viscosities, the surface tension is marginally affected. Based on the wetting properties, slot die coating is feasible.

Table 2.2 – Measured contact angle of different concertation of PVA on different surfaces along with surface tension

Fluid concentration	Contact angle on PET	Contact angle on Acrylic	Surface tension, σ
5 wt.%	59°	53°	0.044 N/m
10 wt.%	56°	51°	0.044 N/m
15 wt.%	52°	54°	0.044 N/m
20 wt.%	52°	53°	0.044 N/m

2.4 Characterization tools

A variety of materials are used to formulate gradient structures to examine the viability of the coating method for different viscosity, diffusion coefficient and inertial force of the flow of two materials, across a variety of applications such as electric devices and ecofriendly barrier layers. Various characterization techniques are used to analyze the properties of the fluids, verify the quality of the resultant gradient films, and to measure the functionality. For measuring the initial thickness, digital caliper from iGAGING® is used but Phenom™ XL G2 scanned electron microscopy (SEM) is used to both measure the exact thickness and visually inspect the cross-section of the fabricated thin film. To investigate the adhesive force of the gradient structured film, cross-cut scratcher and Scotch® tape were used following the ASTM D3359 standard. The gradient color scheme is verified using the Agilent® Cary 60 UV-Vis Sepectrophotometer over the fabricated film. Electrical conductivity is measured using the four-point probe method[76],[77] connected to the source meter. The quality of gradient structures is verified using NicoletTM iSTM 5 Fourier-transform infrared spectroscopy (FTIR).

CHAPTER 3. GRADIENT PATTERNED FILM FABRICATION

3.1 Introduction

In this chapter, gradient patterned thin films are experimentally fabricated using the slot die and R2R system discussed in Chapter 2. The mathematical derivation studies look at the Peclet Number (Pe), which represents the ratio between the advective transport rate and the diffusive transport rate which is shown in Equation 3.1[78].

$$\mathrm{Pe} = \frac{Advective\ Transport\ Rate}{Mass\ Diffusion\ Rate} = \frac{Lv_f}{D} \tag{3.1}$$

where L represents the linear characteristic length dimension of the flow, v_f is the flow velocity and D is the diffusion coefficient. Huysmans et al.[75] showed that if the Pe value is lower than 1, it indicates that diffusion will dominate the flow regime which means that the fluids will instantly diffuse into each other. This is how T-junction micromixer allows mixing to happen in their channel using a very slow flow rate and short distance[79]. High Pe value indicates that the two flows are near immiscible, but even if the Pe value is high, this does not mean there is zero diffusion. This can be more ideal for gradient formulation as complete mixing is not needed to create a gradient, but rather just partial mixing is needed. Moreover, this allows the gradient formulation suitable for slot die coating as slot die is more capable of larger scale flow rates.

The gradient fabrication through slot die system is investigated using aqueous PVA solution. Firstly, same weight concentration of PVA is introduced to the three inlets but with different colors for visual distinction. Secondly, the gradient production is studied with different combinations of PVA concentrations, also with food colorings for qualitative results. The gradient formation at both the internal and external phases are studied and to evaluate the effect of the flow rates on the dimensions of the coated films, experimentations are made by altering the just the center flow rate or just the side flow rates but the other parts stagnant. Finally, the fabricated films are characterized for their functionality especially in the adhesive force. Microscopic imaging is conducted to prove the existence of gradient structure.

3.2 Validation of Theory Using Slot Die Coating

3.2.1 Flow Rate Calculation

Cubaud et al. modified Pe term formed by., the flow rates through each inlet can be calculated using Equation 3.2.

$$\mathrm{Pe} = \frac{\chi Q_1 + Q_2}{2wD} \tag{3.2}$$

where, χ is the viscosity ratio between the center fluid and the side fluid where the center fluid has higher concentration. More viscous flow must be in the center as the less viscous fluid acts as lubricant and reduces the surface area effect of the viscous fluid caused by the wall. Q_1, Q_2, $w_c$is the width at the channel outlet and D.

The range of Pe that induces internal mixing of two miscible at laminar flow within the planar geometry is between 5,000 and 15,000 as experimentally shown by Cubaud et al. Specifically, if the Pe is lower than the set range, the center fluid would be unstable which would cause flow pattern with great randomness. At the higher Pe value, the center flow dominates the overall film instead of mixing where the center flow stream would push the side flow stream. The w_c value is set as 1 cm and the D values is 2.0×10^{-9} m^2/s. Jeck et al.[77] calculates diffusion coefficient by implementing their experimental results into Fick's Law of Diffusion shown in Equation 3.3.

$$\dot{m} = -D \times \frac{\partial c}{\partial z} \tag{3.3}$$

where, $\dot{m}$ is the measured permeation flux which is the quantity of molecules allowed by the membrane and $\frac{\partial c}{\partial z}$ represents the concentration gradient.

3.2.2 Experimental Procedure

Here, we validate the use of a microfluidic channel to fabricate gradient thin films based on Pe, as described in the previous section.

A non-functional fluid, aqueous 10 wt.% PVA solution doped with food coloring is used to fabricate the gradient thin film on PET using a slot die on a R2R, as illustrated in Figure 3.1. The slot die setup is assembled using the 0.0508 mm (0.003 in) thick PET shim. Substrate speed is set to 17 mm/s with coating gap of 0.2 mm which can be used to calculate expected wet thickness later in CHAPTER 7

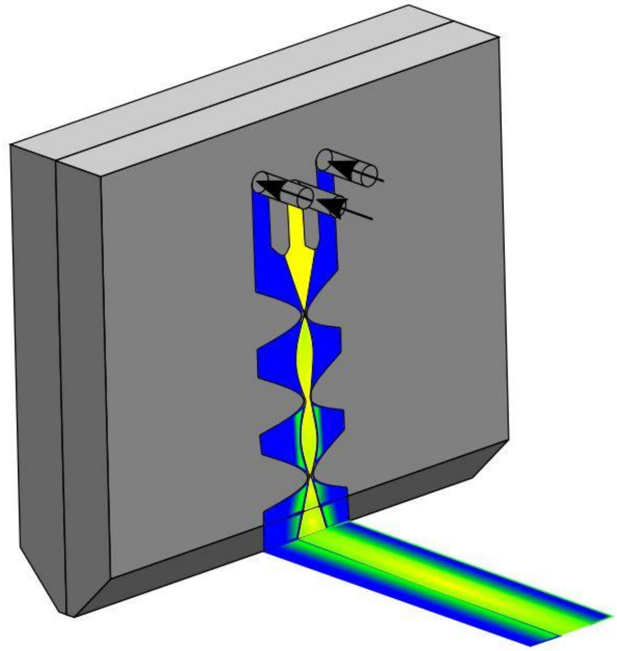

Figure 3.1 – Simple of schematic of the gradient formation of 10 wt.% PVA (Center, yellow) and 10 wt.% PVA (Side, blue) solutions using slot die mounted on R2R system

The center fluid of aqueous 10 wt.% PVA is doped with yellow food coloring and the side fluids of aqueous 10 wt.% PVA is doped with blue food coloring. Aqueous 10 wt.% PVA solution was prepared from 10 g of PVA crystals in 90 g of Deionized (DI) water for 30 minutes at 60°C on a hot plate using a magnetic stirrer. One drop of food dye is added per 2 mL of the fluid and stirred rigorously using stirring rod for at least 10 seconds. About 10 mL of each fluid is poured into the PTFE syringe which are then placed in the digital pump for consistent feed of fluid. To fabricate the gradient thin film, one syringe is filled with the center fluid (10 wt.% PVA, yellow) and is mounted on a pump and two syringes are filled with the side fluid (10 wt.% PVA, blue) and are then mounted on another pump. The flow rate of the center flow stream is set to 1.0 mL/min and the side flow streams are set to 0.5 mL/min. The flow rates of the fluids are set such that they exit the black tubing at the exact same moment, just before being pumped into the slot die.

To ensure the three flow streams reach the inlets simultaneously, the side flow streams are started first to compensate for the longer entrance neck compared to that of the center flow. When the side fluids are visually observed entering the slot die, the center flow is started. This action is mandatory, because if the two pumps are started simultaneously, the center flow would fill the entire slot die cavity and creates reverse flow that resists the incoming side fluid as shown in Figure 3.2.

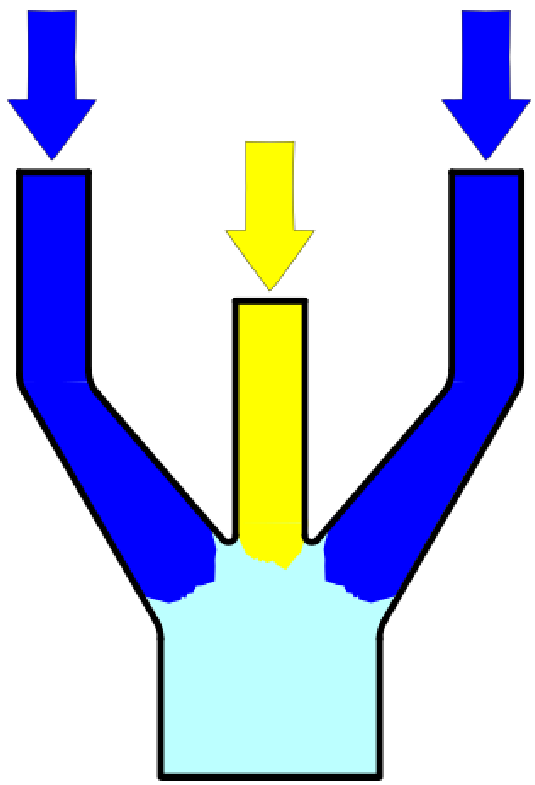

Figure 3.2 - Simple schematic of the flow procedure to induce the fluids to meet at the same point

3.2.3 Experimental Results

The 10 wt.% PVA gradient forms a gradient pattern in the internal slot die cavity and illustrated in Figure 3.3 (a). Furthermore, the gradient pattern is sustained in the coating bead, thereby forming a gradient thin film, which to the author's knowledge, is the first demonstration of a gradient thin film using a slot die on a R2R, as shown in Figure 3.3 (b) and (c), respectively. As shown in Figures 3.3 (a)-(c), a Blue – Green – Yellow – Green – Blue (BGYGB) gradient thin film can be fabricated. However, the distribution of the flow streams is not uniform across the web. Although the width of the outlet channel is 1 cm, the width of coating is measured 1.8 cm. The two sides (blue, 10 wt.% PVA) is 0.3 cm, the center area is 0.8 cm and the gradient area is 0.2 cm each. Hence, the fluid exhibited significant leakage, which theoretically means the coating is not stable. It is believed that pressure gradients forced the fluid out of the flow domain and between one slot die halve and the shim.

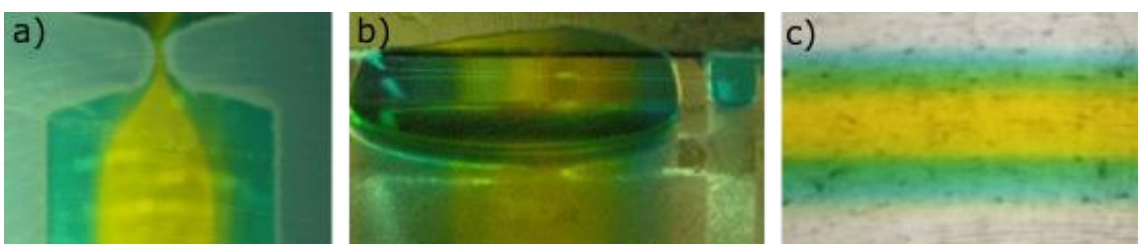

Figure 3.3 - Coated film of 10 wt.% PVA (Center, yellow) and 10 wt.% PVA (Side, blue) in gradated structure using Method 2 showing (a) internal flow, (b) deposition view and (c) wet coating

3.3 Exploration of Different PVA Viscosities

3.3.1 Flow rate calculations of Different PVA viscosities

In this section, different combinations of PVA concentrations are used to explore the influence of viscosity on the fabrication of gradient thin films via slot die coating on a R2R. The combinations are given in Table 3.1. During the experiments, the fluid with the highest viscosity is maintained as the center fluid as less viscous side fluids act as the lubricant for the center fluid which decreases the overall viscous effect. The flow rate of each fluid is calculated based on Equation 3.2, for a Pe value of 5,000 to 15,000. The average of the range is then used as the required flow rate for each fluid. The thickness of the shim is 0.127 mm (0.005 in) to induce better mixing[80] and reduce spreading[81].

Table 3.1 – Flow rate calculations following Equation 3.2 for each combination of PVA concentrations

Center Fluid	Side Fluid	χ	Q_1 (ml/min)	Q_2 (ml/min)
10 wt.% PVA	5 wt.% PVA	5.714	0.95	0.3 ~ 0.5
15 wt.% PVA	5 wt.% PVA	28.57	0.21 ~ 0.45	0.05 ~ 0.2
15 wt.% PVA	10 wt.% PVA	5	1	0.5 ~ 0.7
20 wt.% PVA	5 wt.% PVA	114.3	0.05	0.11
20 wt.% PVA	10 wt.% PVA	20	0.6 ~ 1.5	0.3 ~ 1.0
20 wt.% PVA	15 wt.% PVA	4	1.2	0.6

3.3.2 Defects and Limitations

Certain combinations of PVA concentrations are not suitable for coating due to coating instabilities such as dripping and reversed flow which can cause coating defects such as spreading, gradient non-uniformity, etc.

It has been observed that flow combination with 5 wt.% PVA caused dripping along the dynamic wetting line, at substrate speeds below 21 mm/s. Dripping can be mitigated by increasing the substrate speed, but it was noticed that the speed that compensates the 5 wt.% PVA causes air entrainment on more viscous fluids. For example, an experiment was performed a fluid combination with a high χ, 20 wt.% PVA and 5 wt.% PVA, using the flow rates given in Table 3.1. Under these conditions, internal mixing is observed which verifies the anticipated microfluidic behavior, as shown in Figure 3.4 (a). However, a large volume of fluid dripped behind the upstream die and overflowed on to the downstream which resulted in premature mixing of fluid, as shown in Figure 3.4 (b). Due to such phenomenon, the resultant coating at was very widely spread with altered flow pattern with the center flow unwantedly displaced beyond the side fluids.

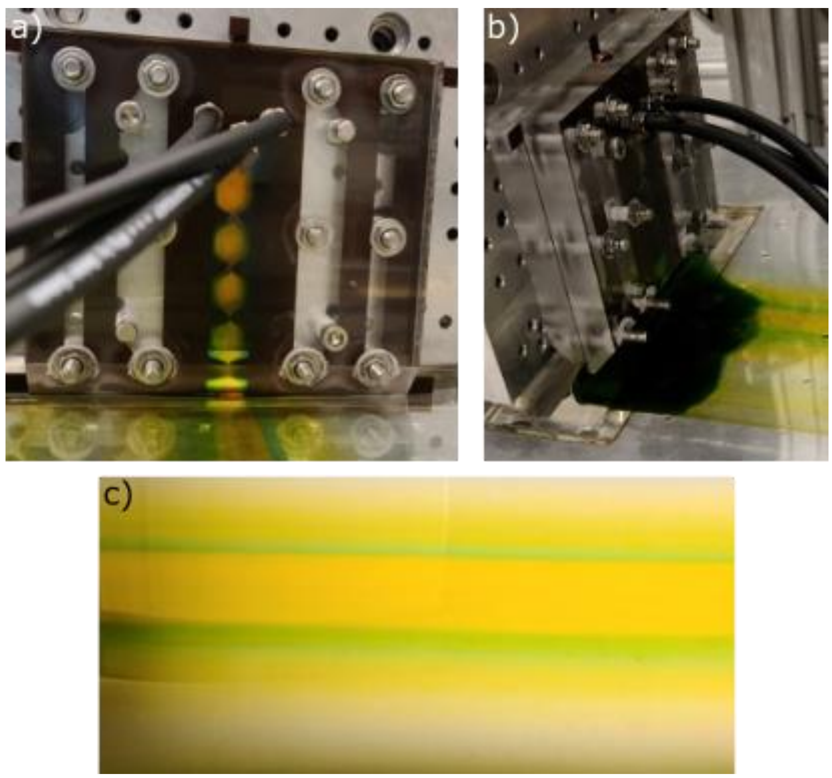

Figure 3.4 - Gradient formation results of 20/ 5 wt.% PVA showing (a) internal flow, (b) dripping at deposition and (c) deposited film

On the other extreme, a low χ is considered, 20 wt.% PVA and 15 wt.% PVA. In this case, reverse flow behavior is observed due to the back pressure formed by viscous effect. Neither image capture of internal flow nor deposition was obtainable as the back flow started as soon as the three flow streams made contact at the die inlet and the side flow streams began invading the center flow stream, intruding into the syringe(s), as shown in Figure 3.5 where the blue side fluid invaded the syringe filled with the yellow center fluid. Therefore, only two fluidic combinations (15 wt.% and 10 wt.% PVA or 20 wt.% and 10 wt.% PVA) are used for the remainder of the work.

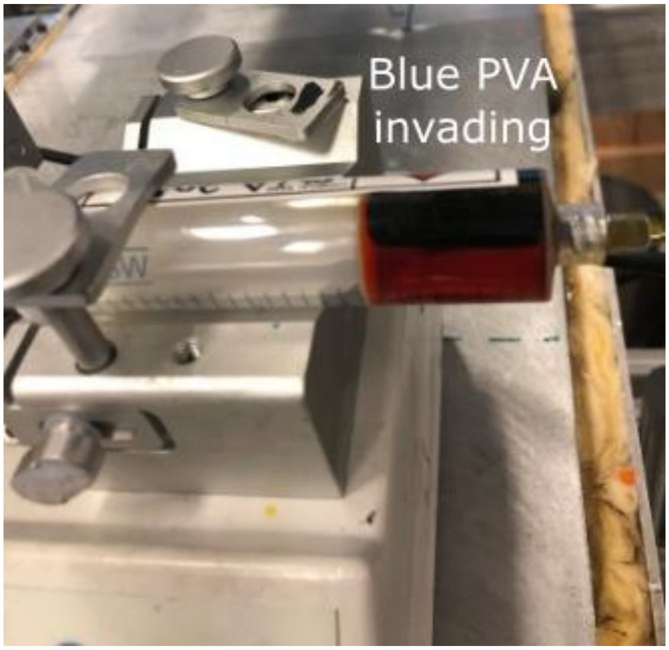

Figure 3.5 - Intruded center fluid syringe at viscous gradient formation using 20 wt.% PVA (Center, yellow) and 15 wt.% PVA (Side, blue)

3.3.3 Comparison of Different Results

Coating with yellow 15 wt.% PVA and blue 10 wt.% PVA for a range of flow rates has resulted in the formation of an internal gradient, which is maintained externally. A typical example of the coating quality for 15 wt.% PVA and blue 10 wt.% PVA is shown in Figure 3.6 (a). A similar trend was shown for 20 wt.% PVA and 10 wt.% PVA as shown in Figure 3.6 (b). The 15%/10% PVA gradient film has total width of 16 mm with the center width being 6 mm, gradient width of 1 mm each and side width measured as 3 mm each. For 20/10 wt.% PVA gradient film, the total width is 15 mm with the center width being 6 mm, gradient width being 1 mm each and the side width being 3.5 mm each. Although the deposition width is set to 10 mm, the resultant films are both wider than set width. As mentioned by Parsekian, the liquid-liquid interaction at their interfaces causes abrupt spreading. Comparing the two results, because the flow rates of 15/10 wt.% PVA gradient coating are higher than the flow rates of 20/10 wt.% PVA gradient coating, the 15/10 wt.% PVA gradient coating is wider.

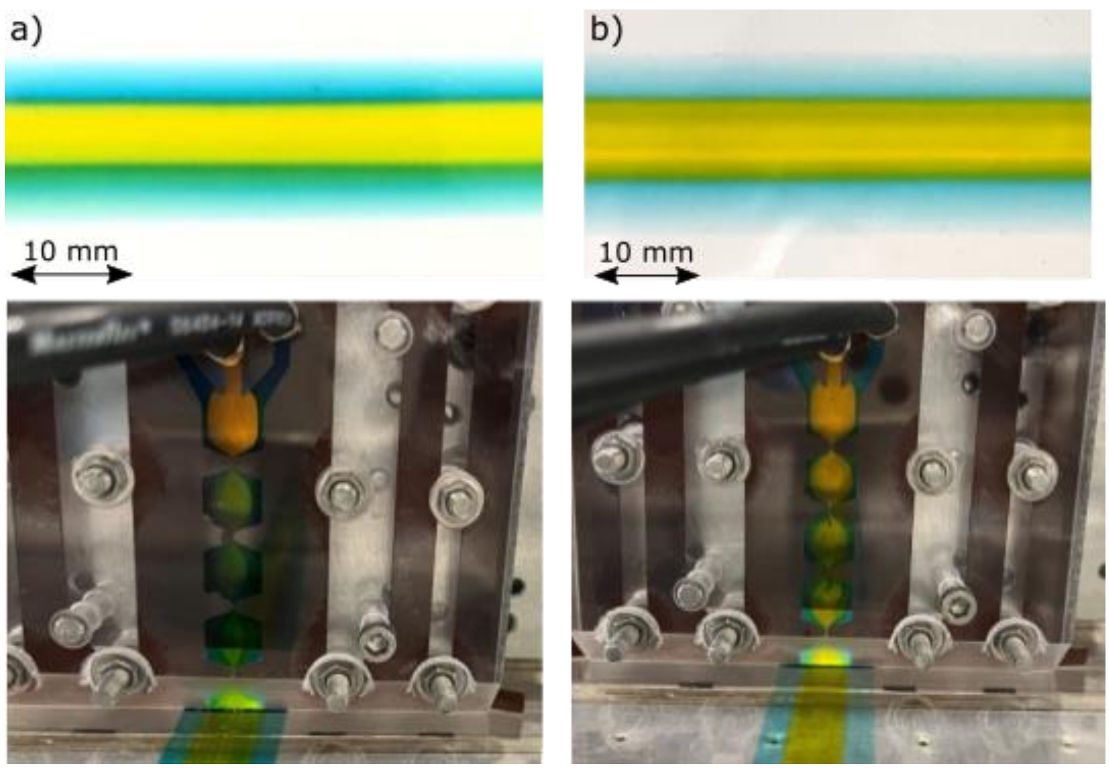

Figure 3.6 - Slot die coated gradient patterned thin film made using (a) 15 wt.% PVA (center, yellow, 1.0 mL/min) and 10 wt.% PVA (sides, blue, 0.5 mL/min) and (b) 20 wt.% PVA (center, yellow, 0.7 mL/min) and 10 wt.% PVA (sides, blue, 0.5 mL/min)

3.4 Effect of Changing Flow Rate

Using the obtained flow rate values in Table 3.1, the effect of changing the center and side flow rates is investigated. To verify the effect of changing the center flow rate, the side flow rate is kept constant. Conversely, to verify the effect of changing the side flow rate, same procedure is performed while keeping the center flow rate constant. The width and thickness of each coated area are compared. For this investigation, 20 wt.% and 10 wt.% PVA are used for the center and side fluids, respectively as out of all the fluid combinations, this has wider ranges of flow rates. Flow rates are increased in increments of 0.1 ml/min within the calculated range shown in Table 3.1.

It has been found that the adjusting the center flow rate has more impact on the Pe. The width of the gradient regions and the center become subsequently larger as illustrated in Figure 3.7 (a) and (c). Changing the side flow rate has a marginal impact on mixing and the overall geometry of the gradient structure, as shown in Figure 3.6 (b) and (d). This phenomenon can be explained using Equation 3.1 calculated earlier as the viscosity only affects the center flow rate. Therefore, it can be explained that the gradient width and thickness are driven by the center flow rates in addition to the wetting properties. All the measurements were made using micrometer with a precision of 0.01 mm.

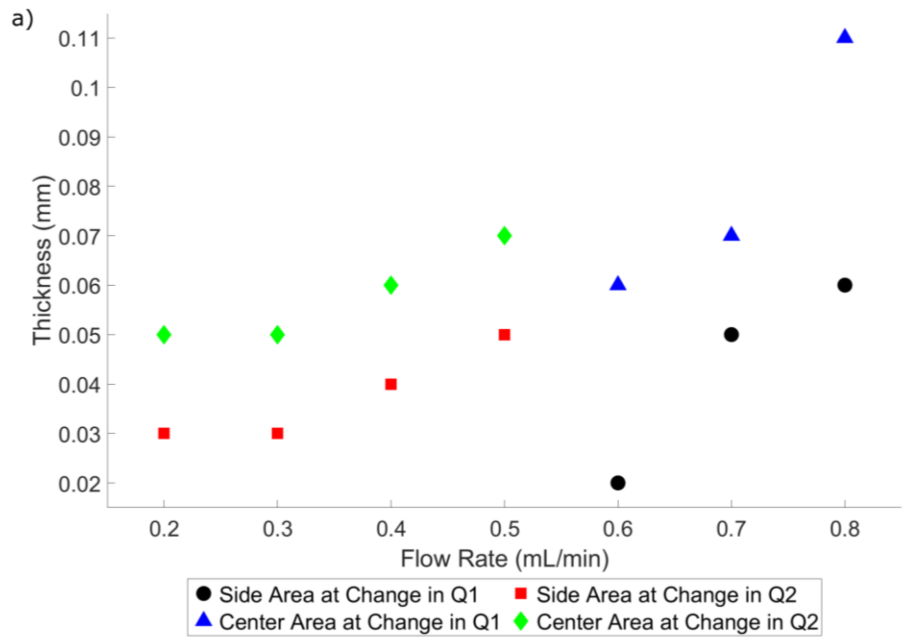

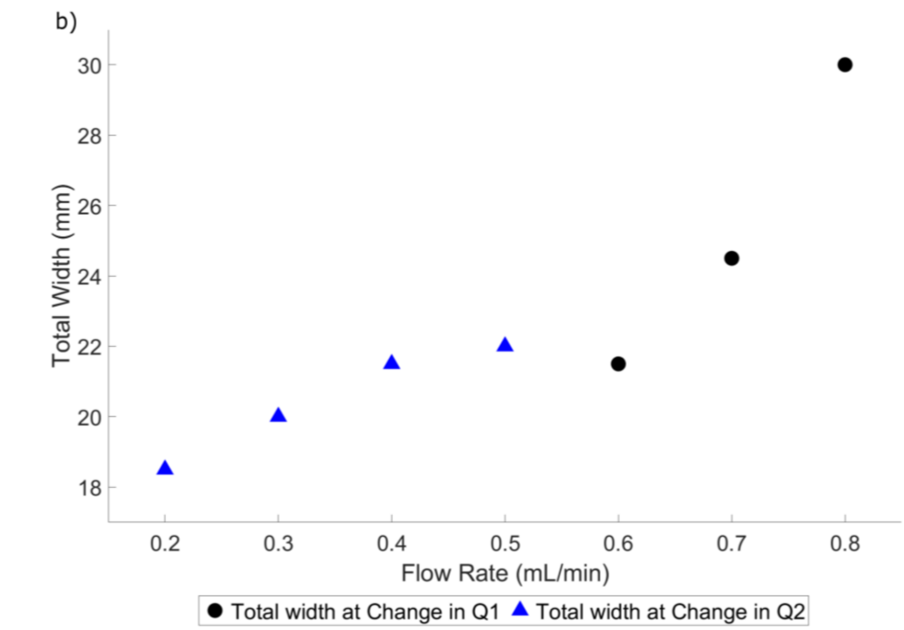

Figure 3.7 - Effect of change in flow rate to the dimension of the gradient film shown in graph form. (a) Change in thickness of both center and side when center flow rate is altered but side flow is stagnant change in thickness of both center and side when side flow rate is altered but center flow is stagnant, (b) change in total width when center flow rate is altered but side flow is stagnant and change in total width when side flow rate is altered but center flow is stagnant

It is known that the if the flow is below the lower Pe limit of 5,000, the center flow becomes very non-uniform with wavy patterns noted in the center flow because during the diffusion process, χ locally decreases and overall stream width narrows which causes distorted wave-like flows[27]. When Pe is over the upper limit of 15,000, the center flow starts to dominate the overall flow since the change in center flow rate has biggest impact on the Pe and this results in two fluids stacking[27].

As shown in Figure 3.8, for 20 wt.% PVA (center, yellow) and 10 wt.% PVA (side, blue), the dashed boxed area flow rate combinations showed the best results. The center flow rate ranges from 0.6 to 0.8 mL/min while the side flow rate range from 0.3 to 0.5 mL/min. It is interesting to note that when the ratio between the side flow rate to center flow rate is 1, the flow is dominated by the side flow. Meaning the edges are pure blue, and the center is mixed with blue as observed in the figure. This happens as there are more side fluids pushing into the center fluid line as the mixing occurs simultaneously. Similarly, when the ratio is below 0.5, the flow is dominated by the center flow and the film becomes more yellow. This occurs as the side fluid is being pushed to the walls of the channel where there is zero velocity. Although the flow rate calculations are within the Pe range, the diffused pattern does not follow through to the deposition phase, due to the spreading behaviors in the deposition zone where wetting and the coating gap must be considered. Moreover, the leakage through the gap between the die blocks and the shim can create different fluidic behaviors that affects the overall mixing behaviors, especially when the ratio is above 1.

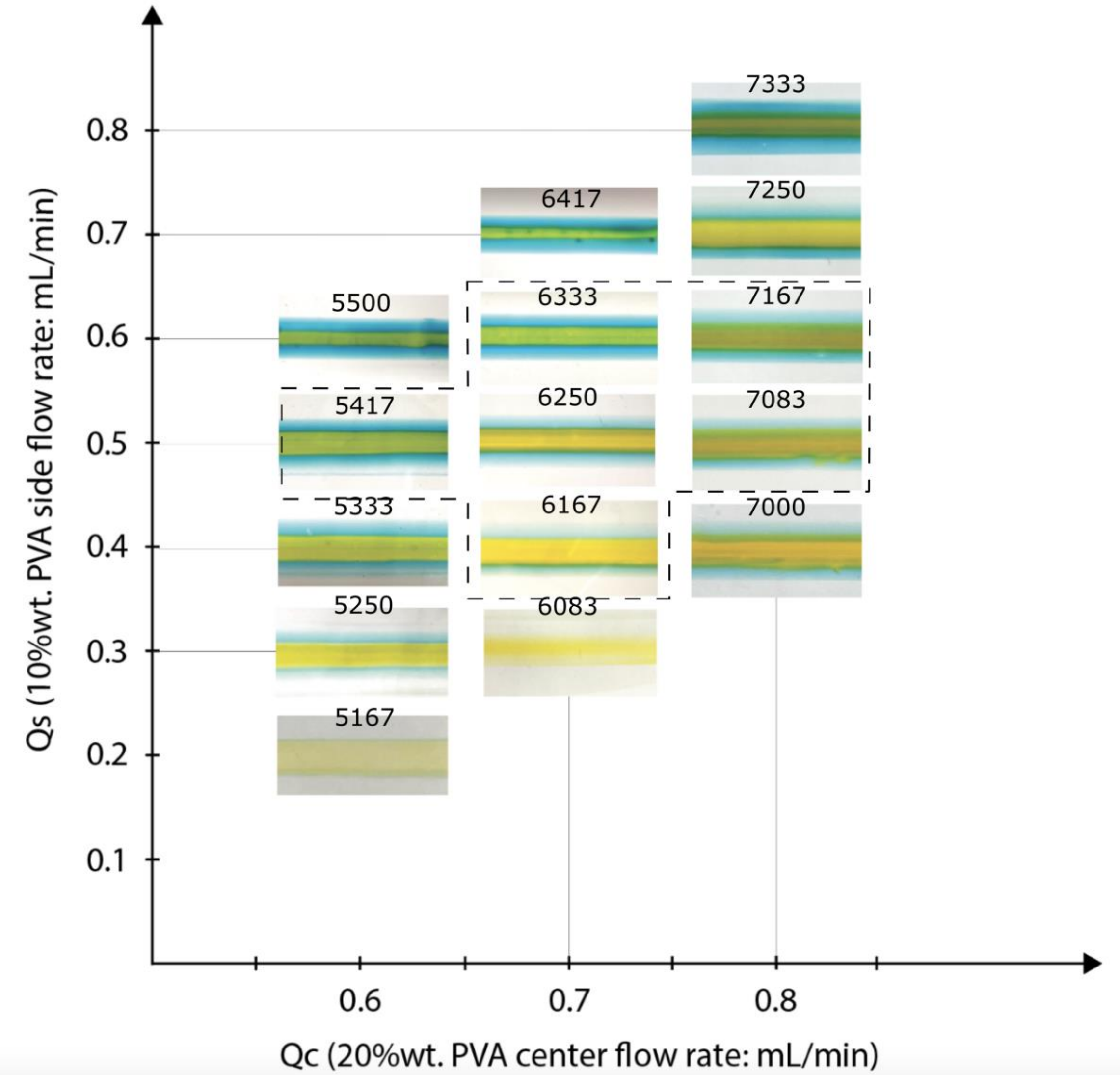

Figure 3.8 - Quality chart showing coating at different ranges of flow rates both at the lower and upper Pe limit

As seen in the results in this chapter, there are clear fluidic and process limitations on the gradient formation through the microchannel. Firstly, there are lower and upper concentration boundaries of the fluid where fluids with low viscosity, forms gradient internally but has defects during the deposition. When both fluids are very viscous, there are limits to fluid flow due to the wall effect and viscous force. Secondly, although the flow rate ranges do fall into the Pe range, at side flow rates below 0.2 mL/min, the center flow starts to dominate the overall internal cavity which impacts the film at deposition, due to low side flows being at the wall. Also, at higher Pe value of at around 7,000, some defects can be noticed. The main reason behind such phenomena is because the previous work that presented the Pe range aimed to have fully mixed fluids instead of creating the gradient.

3.5 Characterization of Gradient Patterned Thin Film

3.5.1 Microscopic Characterization

The dimensions of the gradient thin film are analyzed using multiple characterization tools including a scanning electron microscope (SEM). A Phenom^{TM} XL G2 SEM is used to visually inspect the cross-section of the fabricated thin film. To make a clear comparison, different types of coatings are tested which include plain 10 wt.% PVA coating, 20/10 wt.% PVA gradient coating. The cross-sectional images shown in Figures 3.9 (a)-(c) shows the thickness difference of the gradient structure. The SEM images were taken along the center, gradient, and side area with the thickness measured using software named ImageJ®. For 20/10 wt.% PVA gradient film, the thickness of center, side and gradient area are 68.70 μm, 51.32 μm and 55.72 μm respectively as shown in Figure 3.8 (a). The comparison of the theoretical and experimental thickness will be mentioned in CHAPTER 7 of this dissertation.

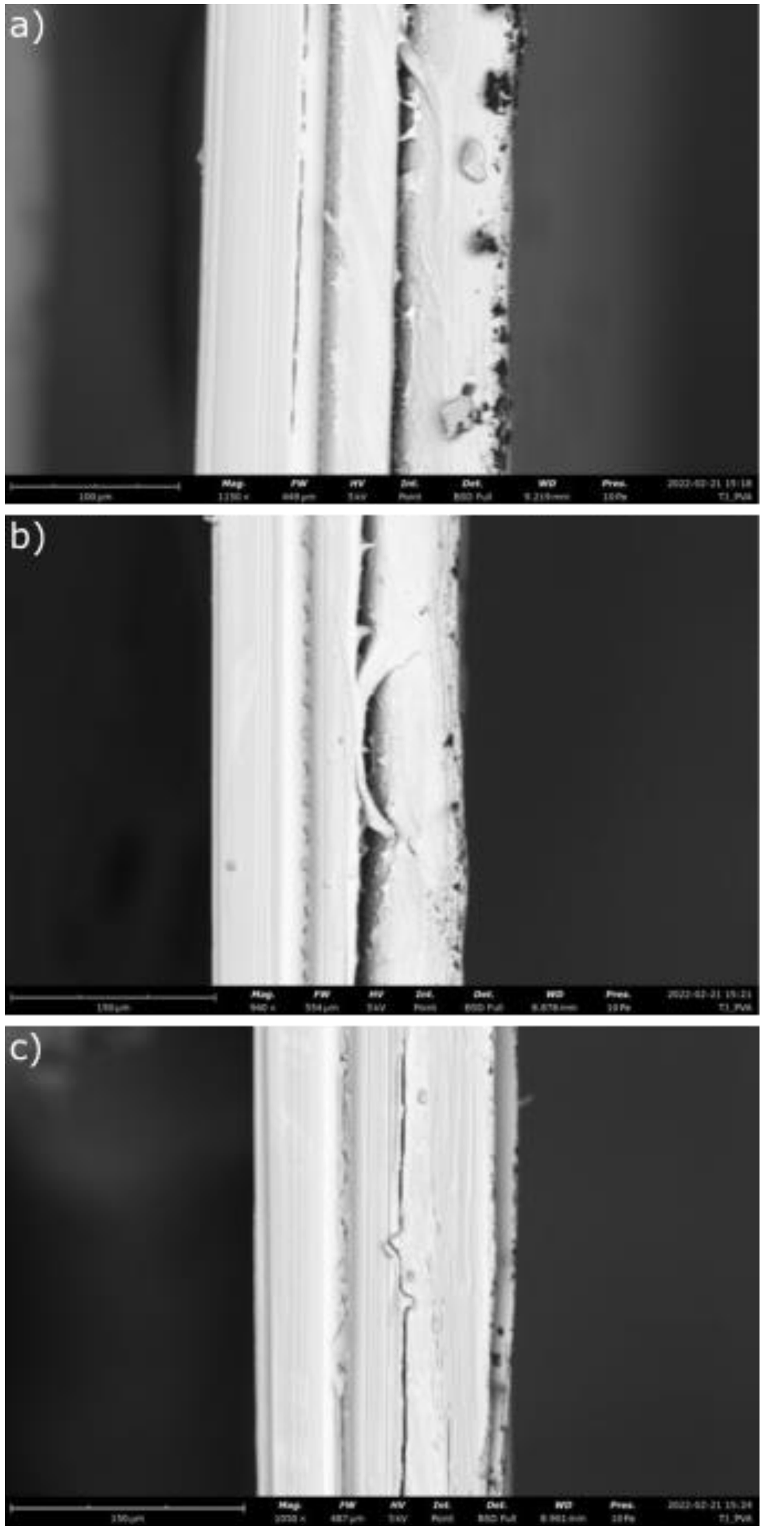

Figure 3.9 - Cross sectional image of PVA/PVA gradient film with (a) center area, (b) side area and (c) gradient area

3.5.2 Adhesion Test

It has been shown from adhesion tests that PVA has very poor adhesion on PET. Regardless of PVA concentration it has been found that it has poor adhesive on PET, exhibiting category 0B delamination, per the chart shown in Figure 3.11. As shown in Figure 3.10 (a), the PVA coated on PET completely delaminates from the PET surface. Changing the concentration of PVA does not improve the adhesive of the gradient thin film to PET as shown in Figure 3.10 (b). Unfortunately, due to the poor adhesive nature between the coating material and the substrate material, gradient structure could not aid with the improvement of adhesion. This is understandable as PET is negatively charged and PVA is non-ionic. The usefulness of gradient structure can be verified if a positively charged material is coated on the PET.

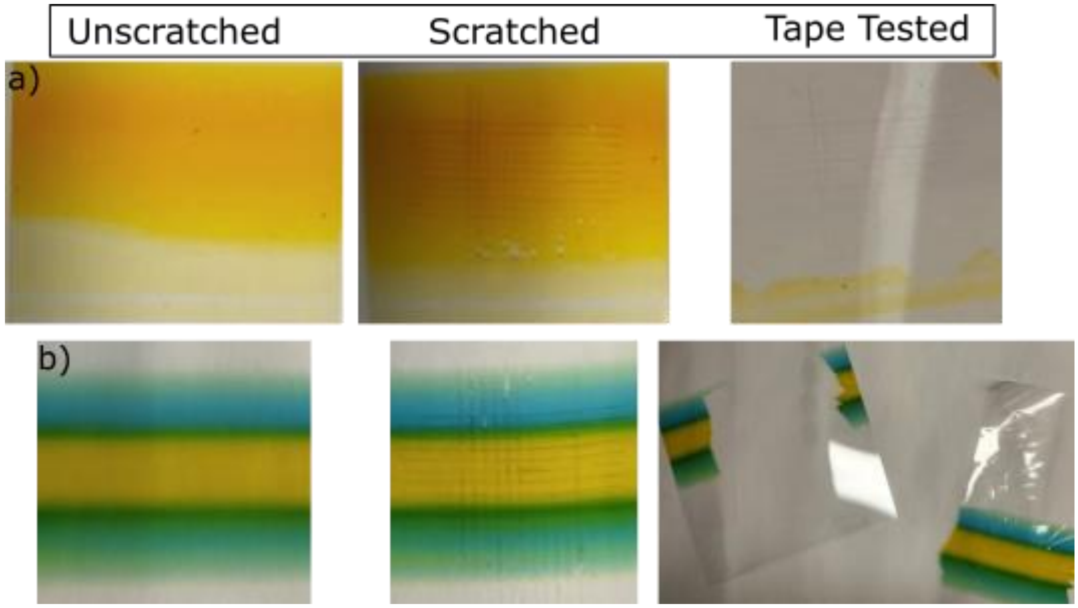

Figure 3.10 - Adhesion test result of (a) 15 wt. PVA (1 mL/min) and (b) 20 wt.% PVA (center, 0.7 mL/min) and 10 wt.% PVA (sides, 0.5mL/min) at unscratched state, scratched state and Tape tested state.

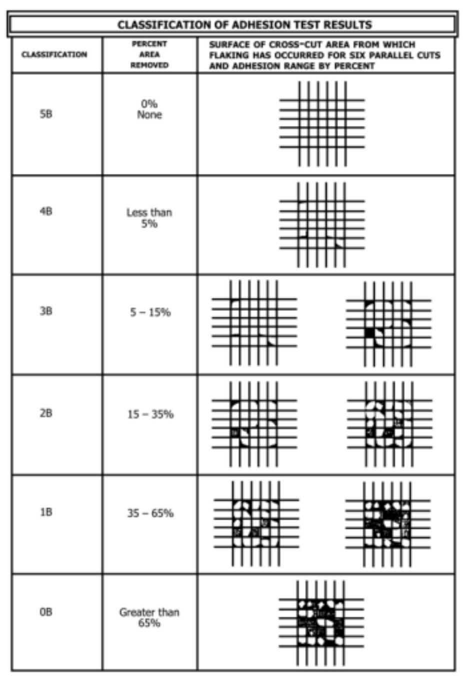

CLASSIFICATION OF ADHESION TEST RESULTS		
CLASSIFICATION	PERCENT AREA REMOVED	SURFACE OF CROSS-CUT AREA FROM WHICH FLAKING HAS OCCURRED FOR SIX PARALLEL CUTS AND ADHESION RANGE BY PERCENT
5B	0% None	
4B	Less than 5%	
3B	5 – 15%	
2B	15 – 35%	
1B	35 – 65%	
0B	Greater than 65%	

Figure 3.11 - Classification of adhesion test results given by ASTM standard

3.5.3 UV-vis Spectrometry

The UV-vis spectrometer is used to verify the gradient more quantitatively. The 20/10 wt.% PVA gradient thin film with Q_1 = 0.7 mL/min, Q_2 = 0.5 mL/min and constant coating parameters is used for this verification which is shown in the call out image of Figure 3.12. It is known that the blue pigment shows peak absorbance at wavelength of around 630 nm[82] and the yellow pigment shows peak absorbance at wavelength of around 405 nm[83]. As shown in Figure 3.12, the blue and yellow absorbance results follow the known wavelength values but for the gradient area, the peaks are apparent at both yellow and blue meaning both colors exist. The yellow absorbance data shows that there are some blue pigments, which is believed to be indicative of mixing in that region. The scattering at the peak is due to experimental errors.

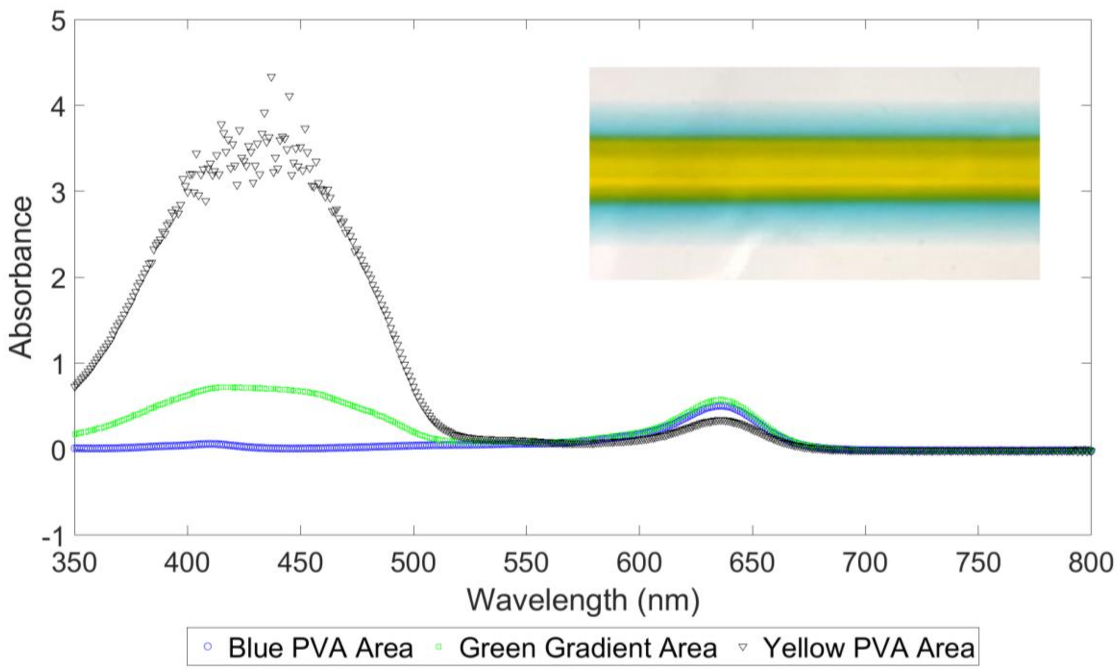

Figure 3.12 – Absorbance to wavelength data obtained from the UV-vis Spectrometer for 20/10 wt.% PVA gradient film at side (blue), center (yellow) and gradient (green) areas

3.6 Summary

In this chapter, it is shown that the gradient thin film using scalable slot die coating on R2R system can be fabricated using this continuous technique. It has been found that the internal mixing based on microfluidic flow in a planar device is the most important factor for the internal gradient formation. However, the stability of the coating bead is important as well. For visual effects, food coloring was used to observe the formation of the gradient during the fabrication process.

Specifically, the influence of flow rate as a function of Pe and viscosity has been investigated experimentally for PVA solutions of the same and different concentrations.

The effect of flow rates has demonstrated that feature size control is dominated by the flow rate of the center flow stream which is more viscous. The width of the gradient and overall film can be determined based on the flow rate of the center fluid as a function of the side fluids. It has been found also that the gradient is maintained in the coating bead, due to the wetting and spreading behavior of the fluidic materials. However, there are limitations related to the viscosity ratio, which is necessary to avoid coating defects in the coating bead, such as recirculation and dripping.

Unsurprisingly, the overall functionality of the gradient thin film was assessed using adhesion test. It has been observed that different concentrations PVA does not enhance adhesion, whereas in other work discussed in CHAPTER 5, we have observed improvements, when well-known functional materials are used.

CHAPTER 4. CFD ANALYSIS OF THE GRADIENT FILM PRODUCTION

4.1 Introduction

The usefulness of CFD has been proved multiple times to analyze the internal flow behaviors in slot die coating[84,85,86]. The works looked at single fluid 2D analysis without any mixing behaviors. Therefore, work in 2D and 3D CFD analysis of multiple fluids are required to verify the experimental results. In this chapter, ANSYS® 21.0 Fluent is used along with Volume of Fluid (VOF) modeling to analyze mixing of two fluid phases flowing inside the designed flow cavity.

4.2 Assumptions

To simplify and accelerate the overall computational process, there are several assumptions that the CFD analysis is based on. The assumptions are listed below:

1. Overall process is laminar
2. No temperature effects to reduce any outside effects
3. Transient analysis to investigate the change over time
4. Pressure based solver as it uses the fluid properties to solve the momentum equation to update the pressure. Moreover, to use VOF analysis, pressure-based solver is mandatory
5. The flow cavity geometry was initially filled with one fluidic material then the second flow is introduced

6. The geometry is truncated to consist just one microchannel with symmetry down the center to reduce run time.

4.3 Boundary Conditions

The boundary conditions are shown in Figure 4.1 (a), where (1) shows the side fluid inlet with velocity of the fluid back calculated using flowrate and the cross-sectional area, (2) shows the center inlet of the fluid also with velocity back calculated using the same method as (1), (3) is the symmetry surface, (4) is the pressure outlet with pressure gauge of 0 psi to represent outflow into air and otherwise are set as fluidic body. As shown in Figure 2.4 (b), the 3D boundary conditions are kept the same as the 2D geometry but (5) wall is added to set the solid boundary material.

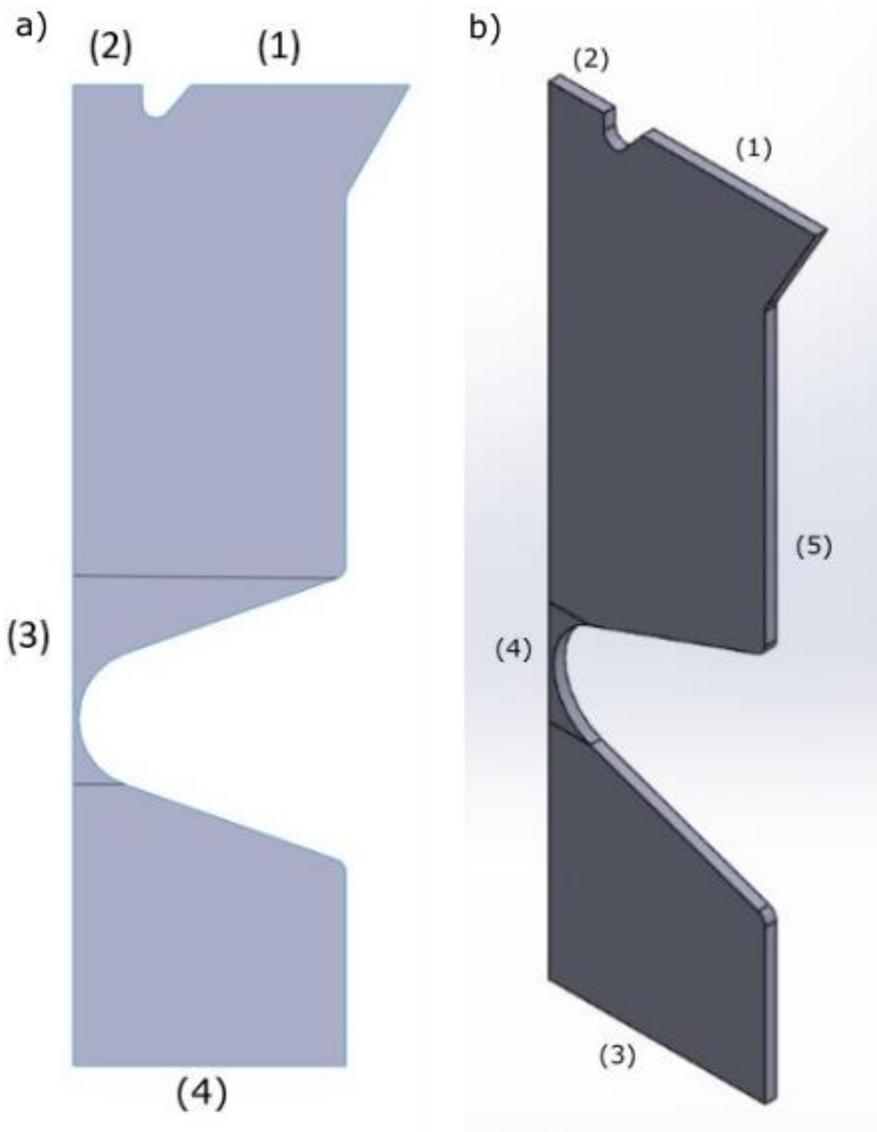

Figure 4.1 - Geometry used for (a) 2D and (b) 3D ANSYS CFD with boundary conditions

4.4 Methods and Governing Equation

ANSYS® 21.0 Fluent can capture very fine meshes across length scales and solve 2D and 3D domains for multiple fluid phases. The internal cavity of the slot die is composed of regions on the macro and micro scales and two fluid phases are considered, Fluid 1 and Fluid 2. To induce mixing, Multiphase modeling with Volume of Fluid (VOF) is utilized for the three phases. The analysis is done using a pressure-velocity algorithm named Semi Implicit Method for Pressure Linked Equation (SIMPLE)[87], which is embedded in Ansys. This algorithm utilizes mass conservation to obtain a pressure field based on the relationship between a corrected velocity and pressure values, given as:

$$\frac{\partial\rho}{\partial t} + \nabla\left(\rho\vec{v}_f\right) = S_m \tag{4.1}$$

where ρ represents the density of the fluid, *t* represents time, v_f represents velocity and S_m represents mass added to the continuous phase from the dispersed second phase. The conservation of momentum in a non-accelerating reference is shown in below:

$$\frac{\partial}{\partial t}\left(p\vec{v}_f\right) + \nabla\left(p\vec{v}_f\vec{v}_f\right) = -\nabla p + \nabla(\vec{\tau}) + \rho\vec{g} + \vec{F} \tag{4.2}$$

where g represents gravitational acceleration, *F* represents the external body forces and τ represents the stress tensor, given by:

$$\bar{\bar{\tau}} = \mu\left[\left(\overrightarrow{\nabla\vec{v}_f} + \overrightarrow{\nabla\vec{v}_f}^T\right) - \frac{2}{3}\nabla\vec{v}_f I\right] \tag{4.3}$$

where μ is dynamic viscosity and *I* is the unit tensor. From the pressure-based solver, the momentum and continuity equation at steady state can be given by:

$$\oint \rho\vec{v}\cdot\vec{dA} = 0 \tag{4.4}$$

where, A is the cross-sectional area. By integrating the Equation 4.4 over each control volume by the triangular mesh, a discrete equation shown below can be obtained

$$\frac{\partial \rho \varphi}{\partial t} V + \sum_{f}^{N_{faces}} J_f \cdot A_f = \sum_{f}^{N_{faces}} D_\varphi \nabla_\varphi \cdot A + S_\varphi Vol \tag{4.5}$$

where N_{faces} is the number of enclosed cell faces, J_f is the mass flux going through the face and Vol is the overall control volume. The equation can be further explained in Figure 4.2

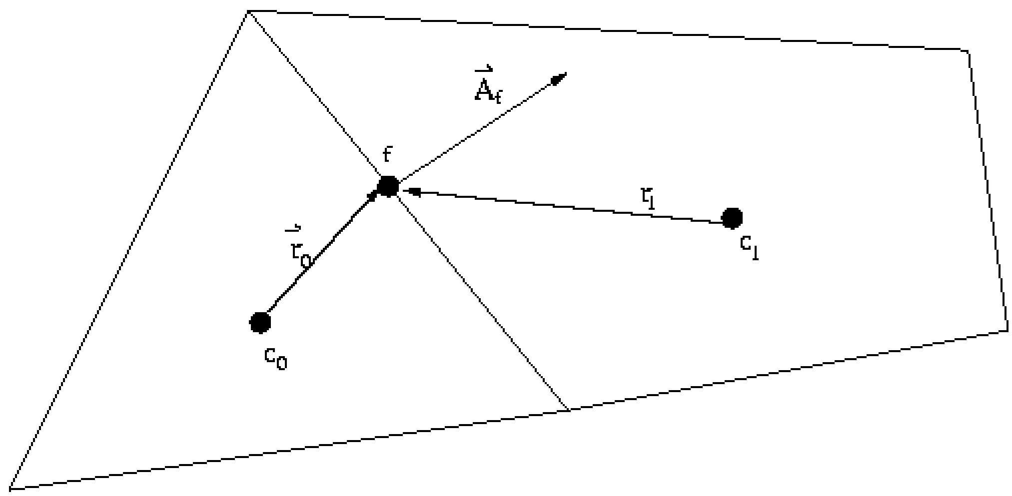

Figure 4.2 - Schematic of scalar transportation in control volume mesh

Following the SIMPLE algorithm, which uses the velocity and pressure corrections to enforce mass conservation, the equation below can be obtained to guess the pressure field and face flux.

$$J_f^* = \widehat{J_f^*} + d_f(p_{c0}^* - p_{c1}^*) \tag{4.6}$$

where J_f^* is the resulting face flux, $\widehat{J_f^*}$ is the influence of velocities in the cells, d_f shows the average momentum and p_{cn}^* values represent the pressure within two cells on either side of the face. These equations can be implemented with continuity equation for the VOF in multiphase, given by:

$$\frac{1}{\rho_2}\left[\frac{\partial}{\partial t}(\alpha_2\rho_2) + \nabla(\alpha_2\rho_2\vec{v}_2) = S_{\alpha_2} + \sum_{p=1}^{n}(Q_{12} - \dot{Q}_{21})\right] \tag{4.7}$$

where 1 and 2 represent the two different phases and α represents the face value of the volume fraction. Parameters including viscosity, velocity, density of the fluid and gravitational acceleration are all user defined depending on the input fluid as previously mentioned in the materials section in Section 2.3, and the boundary conditions in Section 4.3. When computational analysis of outflow to the ambient conditions is investigated, the density and viscosity of air are needed, which are defined as 1.225 kg/m^3 and 1.79$\times 10^{-5}$ kg/m^3, respectively.

4.5 User Defined Settings

For internal flow, three methods (Method 1, Method 2, and Method 3) are used to fill the cavity, following the boundary condition mentioned in Chapter 2. For the fluidic materials, 15 wt.% PVA is set as the center fluid and 10 wt.% PVA is set as the side fluids, with flow rates of 1.0 mL/min and 0.5 mL/min as the center and side flow rates, respectively, to correlate with the experimental results in Chapter 3. Material properties are added based on their measured values.

Method 1: The entire cavity is filled with the center channel solution first using the *Primary Flow* setting, at a continuously flow with an inlet velocity of 0.05 m/s. The inlet velocity is calculated using the flow rate and the cross-sectional area of the inlet. Then, the second solution is introduced into the side at a velocity of 0.025 m/s as a *Secondary Flow*. The *adaptive time step* is set to range from 0.00001 s to 10 s depending on the mesh size to avoid diverging flow and with a total step of 100,000 for sufficient run time.

Method 2: The side fluid is set as the *Primary Flow* and the center flow is then introduced into the flow domain as *Secondary Flow*, using the same velocities and time steps as those used in Method 1.

For both Method 1 and 2, the study has been performed in both 2D and 3D domains. For CFD analysis, a systematic approach is taken since the internal fluid flow region and the deposition region are of interest. Figure 4.3 shows the mesh prepared by separating the flow geometry into three components to set different mesh sizes. The top and bottom geometries, which represent the wider channel which has a width of 10 mm, has an element size of 0.05 mm. The middle area, which contains the 0.2 mm wide microchannel, has a finer mesh of 0.0075 mm per element, to allow for extensive and accurate analysis of the mixing. As shown in Figure 4.4, the mesh sizes at the wider channel and microchannel of 3D geometry are equal to that of the 2D geometry but the thickness was meshed finely to 0.005 mm per elements, to induce more accurate calculations through the whole geometry. For all the meshing elements, tetrahedral shaped elements are to garner better convergence. These mesh settings are selected based on a mesh study, for both 2D and 3D. For 2D analysis, the element size for both microchannel and the wide channel are studied. The number of elements must be as small as possible for faster computational time and more accurate solutions, especially in the microchannel. A larger element size at the microchannel causes divergence in the calculation. Based on the mesh study, it was found that 0.0075 mm per element is needed for convergence. For 3D analysis, the same element size as that used for 2D analysis was found to converge, however, the shape of each element became more important. Rectangular elements are more computationally expensive as the mesh had to be finer. However, tetrahedral elements converged faster and were thus used for the 3D study.

To emulate experimental analysis, the cavity must be initially filled with air. In Method 3, air is set as the *Primary Flow* and the center and side fluids are set as *Secondary Flow*. For Method 3, the overall geometry is truncated with finer mesh in the microchannel of 0.005 mm and other settings are set the same as Methods 1 and 2.

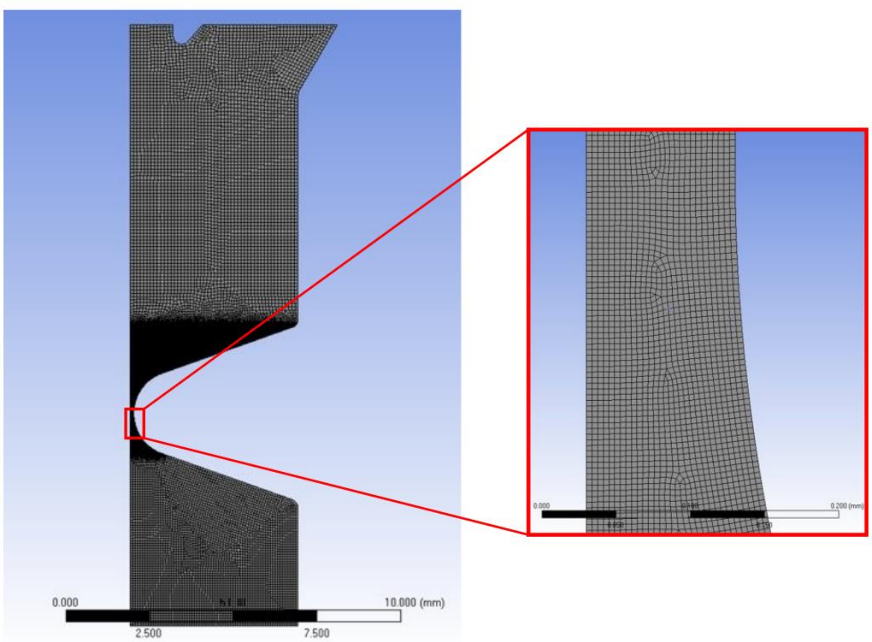

Figure 4.3 - Meshed geometry of the 2D domain with call out image in the microchannel

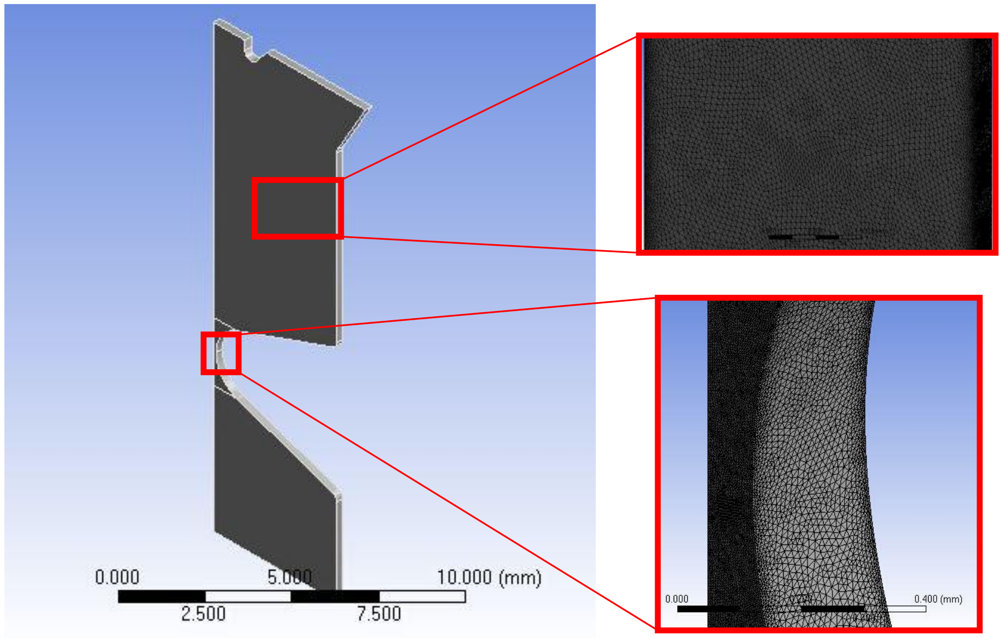

Figure 4.4 - Meshed geometry of 3D domain in isometric view with call out image of the microchannel and through the thickness

4.6 Results

4.6.1 2D Analysis

The contour images of the volume fraction for both Method 1 and Method 2 are shown in Figure 4.5. From the color scheme, the blue shows the *Primary Fluid* and the red shows the *Secondary Fluid*. Hence, the color schemes in Figure 4.3 (a) and (b) are directly opposite. Even so, the mixed regions show up as green in for both Methods. Interestingly, the results of Method 1 and 2 are significantly different.

For Method 1, the side fluid does not reach the wall area, where the velocity = 0 m/s and forms dead zone on the sides. Hence the *Primary Fluid* is not totally displaced by the *Secondary Fluid.* Then, after the fluids pass through the microchannel, the geometry of the *Secondary Fluid* drastically decreases at the deposition region. While mixing is observed, in the interfacial region of the two fluids in the microchannel, it appears that there would be to be streaks in gradient thin film and that the *Primary Fluid* would dominate the film structure as previously illustrated in Figure 3.3 (c). While this is not validated via CFD since the coating bead is not analyzed, there is strong evidence that the final film structure would be similar to that obtained experimentally.

In Method 2, the center fluid adheres to the wall and even after passing the through the microchannel, the flow pattern is very stable without any dead zones. The mixing region is apparent in the chamber after the fluids travel through the microchannel, giving good confidence in the approach and validation of the gradient thin films obtained experimentally in Figure 3.5 (a) and (b).

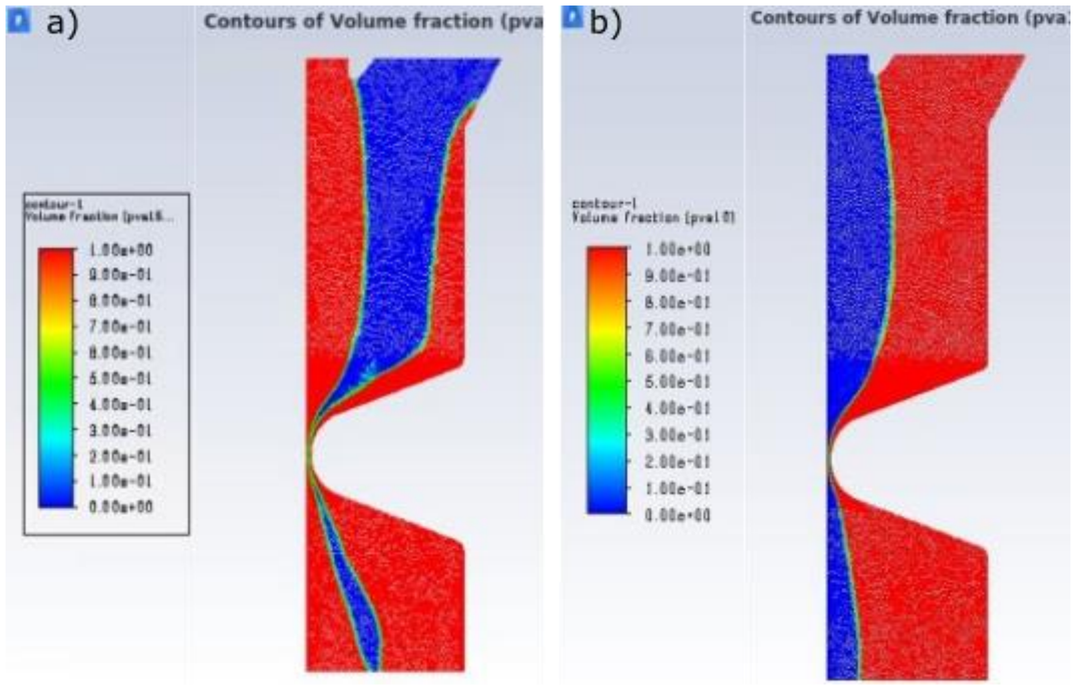

Figure 4.5 - Contour color schemed image showing the VOF results of (a) Method 1 and (b) Method 2

2D analysis for Method 3 is shown in Figure 4.6. Due to the computational expense of simulating the full geometry, the velocity results from the inlet area are derived first, then the values are directly applied to the inlet surfaces of the middle section. The blue colored section represents air (*Primary Flow*), and the green and red colored section represent the 15 wt.% PVA along the center and 10 wt.% PVA along the sides (both are *Secondary Flow*). Mixing of the Secondary fluids is observed, in this case as the yellow line. Also, it is noticed that dead zones are created at close to the walls, in the form of an air pocket. While not clear in the figure, blockage and recirculation from the center fluid seemed to prevent the side fluid from enter the microchannel, which lead to divergence in the computational analysis. While Method 3 is technically to most realistic setup, it is important to note that due to the complexity of simulating and the computational expense, which took more than 2 weeks to reach the result in Figure 4.6, this method was not further pursued.

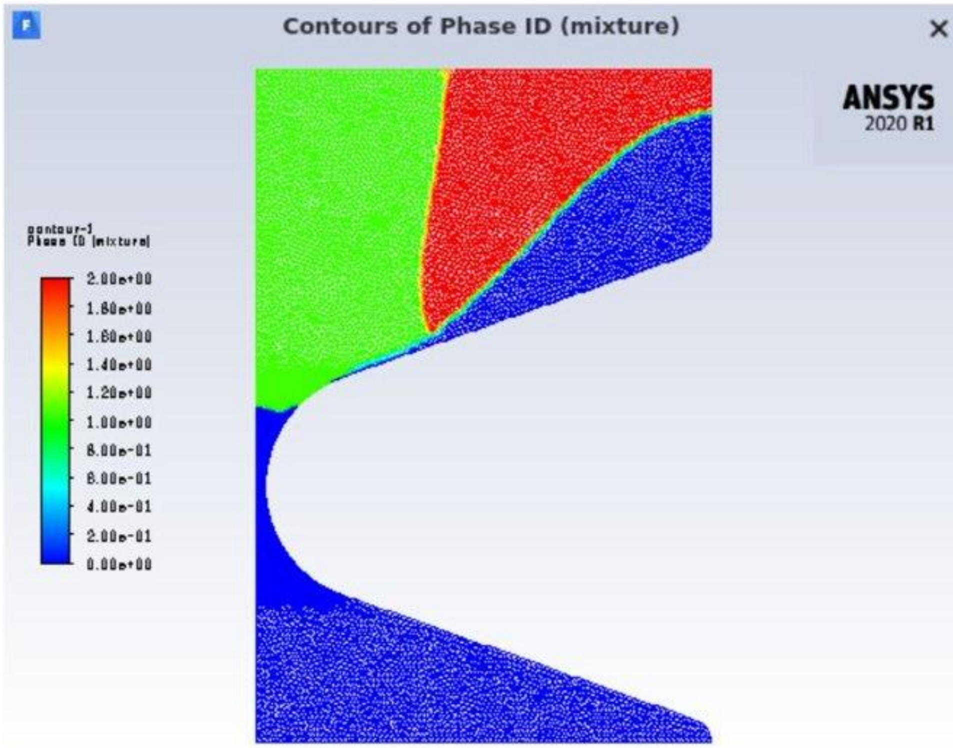

Figure 4.6 - 2D CFD analysis of 3 phase VOF contour image that diverged

4.6.2 3D Analysis

Methods 1 and 2 are analyzed further using 3D analysis. As shown in Figure 4.7, Method 1 resulted in a similar flow pattern as that observed in the 2D analysis where the side flow (*Secondary Flow*) could not fill the whole geometry, creating dead zones at the corner of the large chamber. Moreover, the flow is not seen through the microchannel, but it is shown after the flows pass through the microchannel. Compared to the 2D analysis, the flow pattern in the second analysis is wider but still does not reach the full width of the chamber. As shown in Figure 4.8, due to reduction of viscous effect on the wall, the there are no deadzones. The phase diagrams showed the mixing of the two fluids after it passes through the microchannel. Unlike Method 1, which mixing starts to occur even before entering the microchannel, Method 2 does not mix before entering the microchannel. The deadzones formed in Method 1 can be the factor on why such premature mixing is occurring. The call out image in Figure 4.8 shows that inside the geometry, the flow is continuous and mixing is occurring in the microchannel.

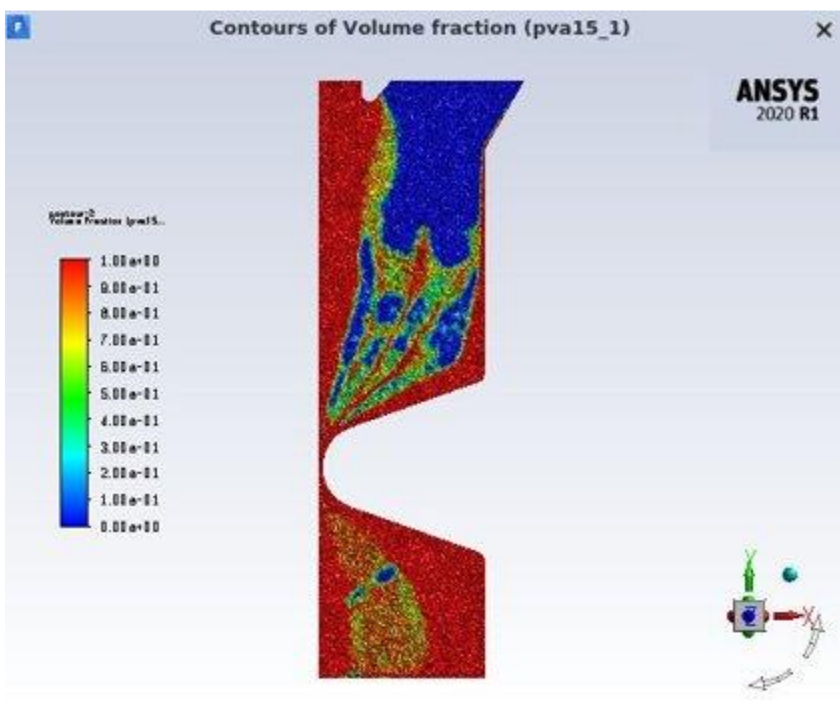

Figure 4.7 - Contour image of VOF result of 3D geometry using Method 1

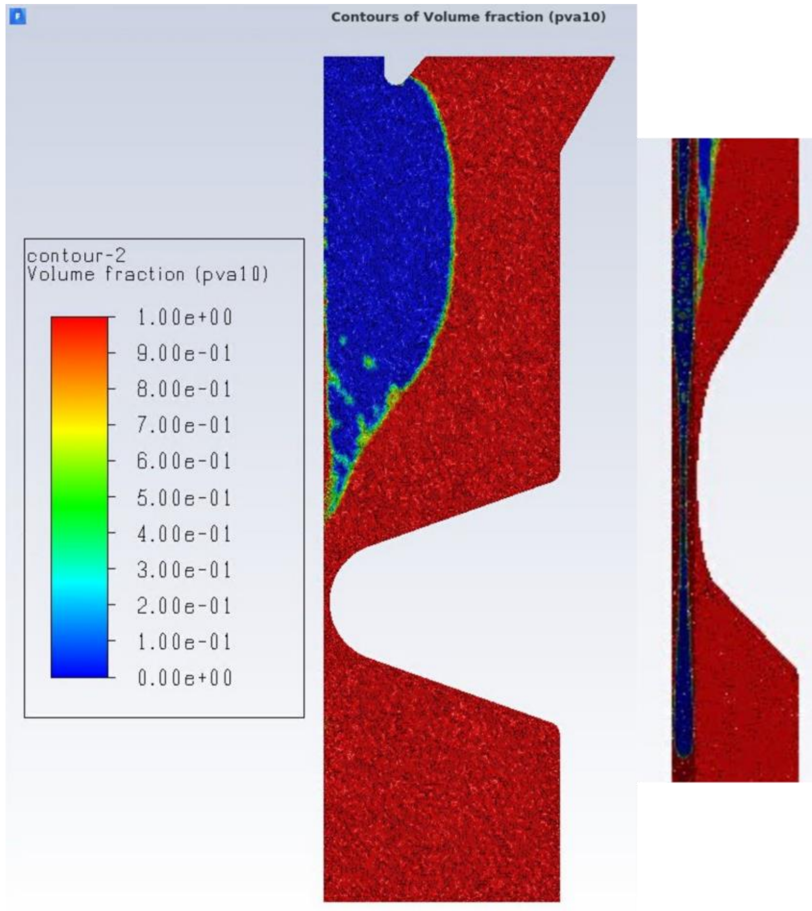

Figure 4.8 – 3D contour image of Method 2 with call out image of the 'Symmetry' wall at the microchannel

4.7 Comparison of Experimental and CFD Results

The complexity of the calculation that occurred in 3D simulation in both Method 1 and 2 which created different patterns than expected. However, looking at the 2D analysis, the experimental data shown in CHAPTER 3 concur with the results of Method 2. As shown in Figure 4.9, the mixing is evident based on gradient of color scheme shown. The mixed width is measured using the measuring tool embedded in the ANSYS which is around 0.019 mm. An experimental test is conducted to verify mixing in the microchannel for 20 wt.% PVA and 10 wt.% PVA gradient film. An Olympus® Zoom Stereo Microscope-model SZ61TR equipped with Olympus® SIS-UC30 digital camera is used to capture the front view of the overall coating process, then Image J® is used to analyze then mixing width in the microchannel. The microscopic image of the fluid flowing in the microchannel is shown in Figure 4.10. The measurement is taken at the narrowest flow width at the microchannel using ImageJ and it is found that the mixing width is around 0.019 mm. The two results are the same which indicated that the CFD results are good precursor to the experimental results. Such investigation is very different from the 2D analysis as in 2D, zero velocity caused by the wall effect is not considered. Therefore, the 2D results show instantaneous mixing when the two fluids meet, whereas the 3D analysis shows that the mixing happens at the microchannel, which is more accurate.

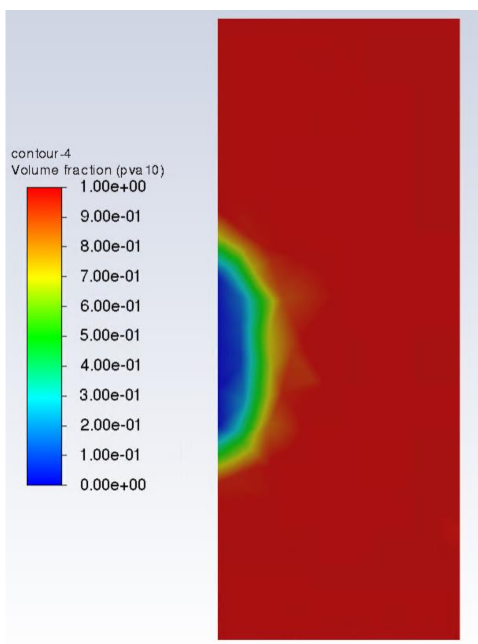

Figure 4.9 – Cross seciton view of flow through microchannel for 3D analysis for Method 2

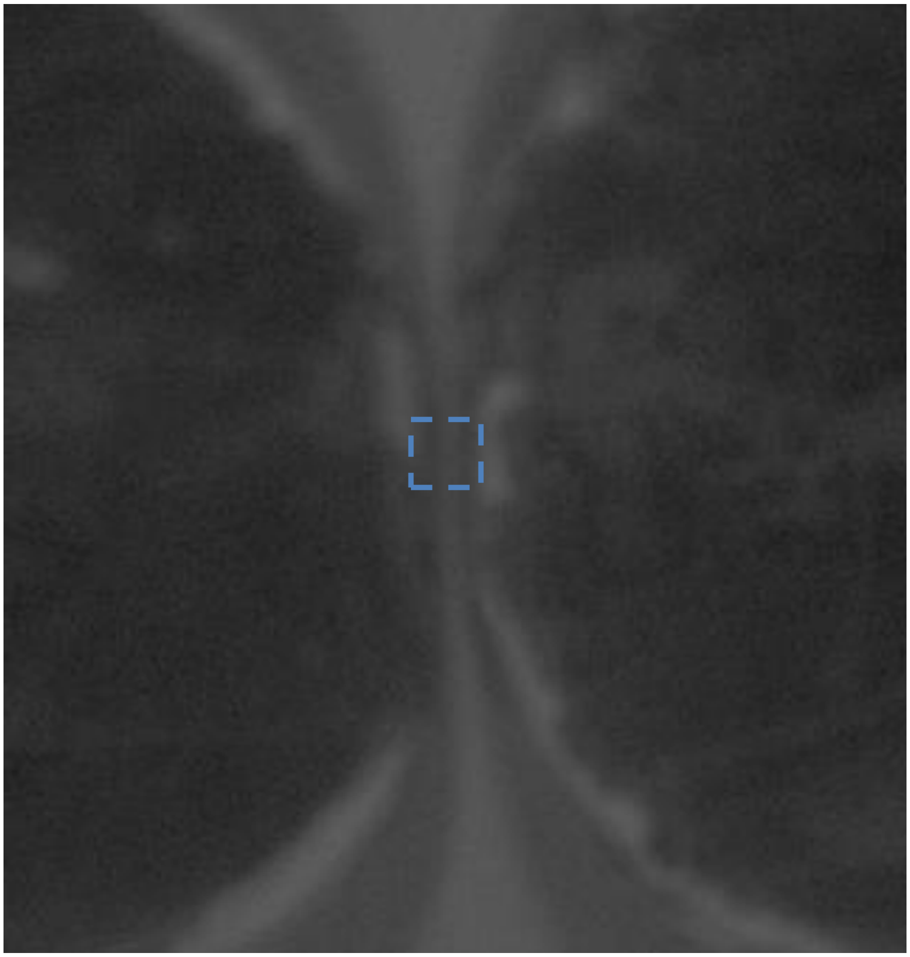

Figure 4.10 - Microscopic image of 20 wt.% PVA and 10 wt.% PVA gradient film at the 0.2 mm width microchannel. Boxed area shows the area of measurement

CHAPTER 5. FABRICATION OF FUNCTIONAL GRADIENT PATTERNED FILM

5.1 Introduction

In the chapters above, the gradient formulations using slot die coating are well proven. However, the gradient structures with just the PVA had limitation in its functionality as PVA was merely used for its convenience and accessibility. Gradient structures have been shown, in previous literature, to improve material properties as the functional material molecules are less dispersed compared to fully blended films, which allow for better intermolecular connection of the materials as the molecules fill up the spaces created by the non-functional materials[7,88,89,90,91]. Therefore, gradient thin film production of functionally graded materials on a R2R with slot die coating on a R2R opens the pathway for large scale production of relevant materials.

Moreover, in recent years, ecofriendly materials are becoming more preferred as thin films used in a variety of fields to reduce negative environmental impacts[92,93,94]. In this chapter, functional materials are investigated. Using a similar approach as that used in Chapter 3 where the flow rate is calculated based on flow in a microfluidic channel, several functionally graded thin film structures are fabricated and analyzed. Change in methods, if any, are listed and the film characterization is performed to show the improvement brought by fabricating the gradient thin film structures.

5.2 Functional Materials

5.2.1 Material Selection and Properties

Some of the mandatory traits for the selected fluidic materials include: 1) water soluble, for easy processability, 2) non-toxic, for user safety, 3) has known functionality and 4) cost effective. To this end, two functional materials have been selected, Poly(3,4-ethylenedioxythiophene) polystyrene sulfonate (PEDOT: PSS) and Polyethylenimine (PEI).

5.2.1.1 Poly(3,4-ethylenedioxythiophene) polystyrene sulfonate (PEDOT: PSS)

Poly(3,4-ethylenedioxythiophene) polystyrene sulfonate (PEDOT: PSS), specifically Clevios™ PH 1000 purchased from Heraeus® is used because it is a well-known conductive polymer, having been used as an organic thermoelectric material applied in fields such as flexible and biodegradable generators[95]. For processability, it is easily dispersed in water or organic solvents. As an aqueous solution, it does not contain any hazardous materials that limits the exposure and while it cost $2.45/gram according to the vendor, compared to $0.194/gram for Mowiol 4-88 PVA, it is significantly less expensive than other materials such as polyaniline which is at least $16/gram.

The material properties of PEDOT:PSS on PET and PMMA are given in Table 5.1. Based solely on the contact angle, PEDOT:PSS would be expected to be non-wetting on PET substrate, similar to what's observed with water, which has , which has a contact angle of 74° on PET. .

Table 5.1 – Important material properties of PEDOT:PSS

Viscosity (kg/m-s)	Contact Angle on PET	Contact Angle on PMMA	Surface Tension (N/m)[96]
0.035	74º	76°	0.070

Generally, a non-wetting fluid would pose significant challenges. However, it has been demonstrated by Parsekian, in the Harris Group, that co-depositing a wetting and non-wetting fluid simultaneously can stabilize the wetting of the non-wetting fluid. Following this interesting discovery, in this work, the PEDOT:PSS must serve as the center fluid, during the experiments. Here, PVA is used for the second fluid phase to fabricate a functionally graded thin film. As discussed in Chapter 3, successful fabrication of gradient structure requires that the center fluid have a higher viscosity. However, 10 wt.% PVA has viscosity of 0.04 kg/m-s, which is higher than that of PEDOT:PSS, and 5 wt.% PVA is not stable for the coating conditions explored. To mitigate these problems, 7.5 wt.% PVA is prepared as Fluid 2, which has the material properties as given in Table 5.2.

Table 5.2 – Material Properties of 7.5 wt.% PVA

Viscosity (kg/m-s)	Contact Angle on PET	Contact Angle on PMMA	Surface Tension (N/m)
0.015	68 º	55°	0.044

5.2.1.2 Polyethylenimine (PEI)

The other functional material, Polyethylenimine (PEI), is a water soluble, non-toxic polymer that has been highlighted for its cationic nature,[97] which allows it to be used in DNA delivery[98,99], organic solar cells[100], functional binder for batteries[101] and CO_2 capture[102]. Generally, PEI has been mixed with other substances[103] and have been spray coated[104] and electrospun[68,105]. Although these are excellent coating procedures, there exist some drawbacks such as material compatibility, resource inefficiency, lack of scalability and low scalability, which are significantly resolved by slot die coating the fluid.

PEI is purchased from Fisher Scientific® (~M.N 60,000, 50 wt.% aqueous solution, branched). The viscosity of PEI was not provided by the vendor, however, it is approximated based on EPOMIN®'s database[106]. The secondary fluid used to form the functionally graded thin film with PEI is 10 wt.% PVA is used due to its versatility and easy processibility. As shown in Table 5.3, the contact angles of 10 wt.% and 20 wt.%. PEI on PET are higher than those on PMMA. Therefore, 25 wt.% PEI is used as the center fluid since 30 wt.% PEI, although has good wetting property, is too viscous to process and create a mixture along the interface. The range of flow rates is greater as the ratio of center to side fluid viscosity are greater.

Table 5.3 – Important material properties used for slot die coating for PEI

Concentration	Viscosity (kg/m-s)	Contact Angle on PET	Contact Angle on PMMA	Surface Tension (N/m)
10 wt.%	0.045	80º	62º	0.067
20 wt.%	0.170	79º	65º	0.064
25 wt.%	0.400	69º	68º	0.064
30 wt.%	0.900	61º	80º	0.064

5.2.2 Flow Rate Calculations

Following the Equation 3.2 from Chapter 3, and using material properties from Table 5.1, 5.2 and 5.3, flow rate ranges for PEDOT:PSS and 7.5 wt.% PVA and 25 wt.% PEI and 10 wt.% PVA are calculated. The flow rate values are shown in Table 5.4.

Table 5.4 - Range of flow rates calculated using Equation 3.2 for PEDOT:PSS/PVA and PEI/PVA gradient structure

Center Fluid	Side Fluid	χ	Q_1 (ml/min)	Q_2 (ml/min)
PEDOT:PSS	7.5 wt.% PVA	2.33	0.9~1.1	1.1 ~ 1.3
25 wt.% PEI	10 wt.% PVA	10	0.8 ~ 1.0	0.6 ~ 1.0

5.3 Methods

For fabrication of the PEDOT:PSS and 7.5 wt.% PVA gradient thin film, same infrastructure (slot die, shim design and R2R system) previously described is used. However, for the 7.5 wt.% PVA, to reduce the possibility of dripping, the substrate speed is increased to 21 mm/s. For 25 wt.% PEI and 10 wt.% PVA, the previously described infrastructure and coating parameters are maintained. (H = 0.2 mm and V = 17 mm/s) and tooling are consistent with previous chapters.

To qualitatively investigate the existence of the gradient, different food colorings including, Red (FD&C 40 and 3), Yellow (FD&C Yellow 5) and Blue (FD&C Blue 1 and Red 40) had to be used. For every 2 mL of fluid, 1 drop of food coloring is added to the base fluid to minimize the effect of the food coloring on the fluid properties of the bulk fluid, while still providing a rich color. For PEDOT:PSS, no food coloring is used since it is black. 7.5 wt.% PVA is dyed yellow. For PEI, red food coloring is used, due to some interesting interactions when mixed with certain food colorings, which will be discussed later in this chapter.

Completely mixed PEDOT:PSS and PVA is formulated in different concentrations to act as a control for the experiments. The PEDOT:PSS/PVA solutions are prepared by altering the weight of each sample, i.e., the content ratio of PEDOT:PSS to PVA is increased from 0% to 100% by creating 1 g of each sample. To be clear, to make 10 wt.% PEDOT:PSS/PVA sample, 0.1 gram of PEDOT:PSS and 0.9 gram of 7.5 wt.% PVA are mixed thoroughly with stirring rod. Then, three drops of each mixed solutions are drop casted onto a PET surface, which had been cleaned with DI water and isopropanol alcohol. To quickly fabricate a uniform surface for the various PEDOT:PSS and PVA concentrations, a blade coater with coating gap of 0.2 mm is used to spread the solutions evenly, then the samples are put into a 60ºC oven for 1 hour to dry. A grid of the various concentrations is shown in Figure 5.1.

Figure 5.1 - Blade coated PEDOT:PSS/PVA solution drops in different solution percentage

The 1:1 weight ratio mixture of PEI to PVA with and without food colorings were also prepared, to act as controls for this fluid mixtures. The fully mixed PEI/PVA solution is slot die coated with the following coating parameters: coating gap of 0.2 mm, substrate speed of 17 mm/s and flow rate of 1.6 mL/min.

5.4 Results and Key Observations

5.4.1 PEDOT:PSS/PVA Gradient Coating

Here, PEDOT:PSS is coated with PVA as the side fluid in order to produce functional gradient structure. An example of the internal gradient formation and the final gradient film are show in Figures 5.2 (a) and (b), respectively.

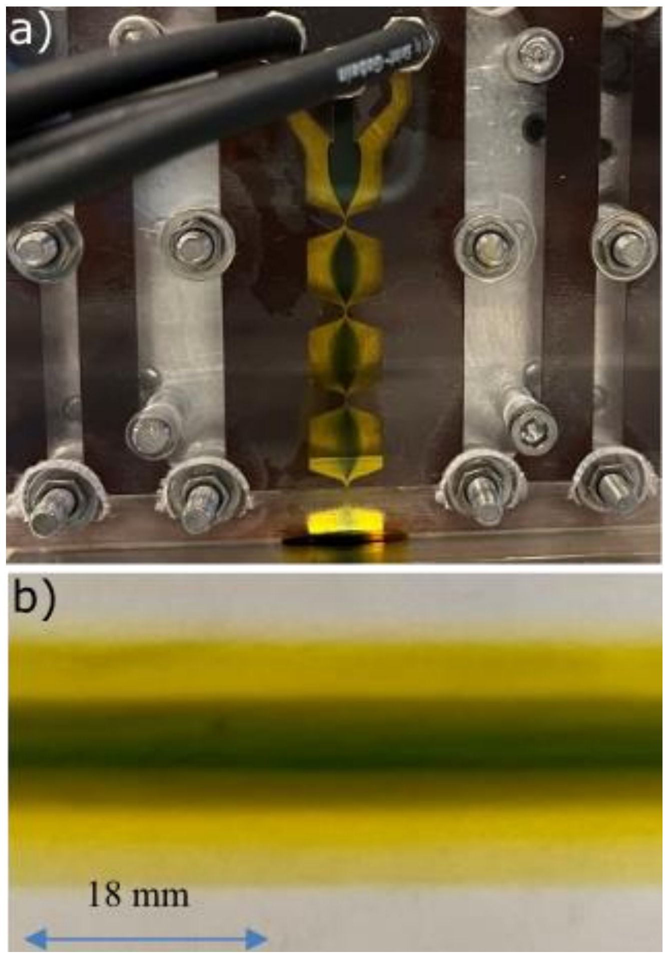

Figure 5.2 - Gradient patterned film coating showing a) the internal cavity and b) the dried gradient thin film where PEDOT:PSS is center, black fluid coated at 1.1 mL/min and 7.5 wt.% PVA is the side fluids, yellow coated at 1.4 mL/min.

A parametric study is performed, such that the flow rates exceed both the lower and upper limits of the Pe values where mixing is induced. This study allows for comparing the theoretical and experimental values. Although the flow rate ranges are deduced to have nine different possible working conditions, as shown in the solid line box area of Figure 5.3 (d), only four combinations had quality gradient formation where clear color scheme is noticeable, as shown in the dashed box of Figure 5.3 (d). Conversely, at flow rate combinations below the lower Pe limit, the center flow shows eroded wavy patterns and it is known that at beyond the upper Pe limit, the center flow dominates the film structure. The eroded pattern can be seen in Figure 5.3 (a) where after the flow passes through the microchannel, the flow starts to form separated pattern. As result, unstable wavy patterned film is deposited. Interestingly, in the upper right corner section of Figure 5.3 (d), although the flow rate conditions are within the given Pe range, the deposited film does not hold the anticipated pattern. However, looking at the internal flows, the diffusion is visible meaning that there are discrepancies at the deposition phases. Such discrepancies include the leakage at the gap between the die blocks and the shim and spreading effects at the deposition that could change the overall film formation as the effect of substrate speed and coating gaps are not studied.

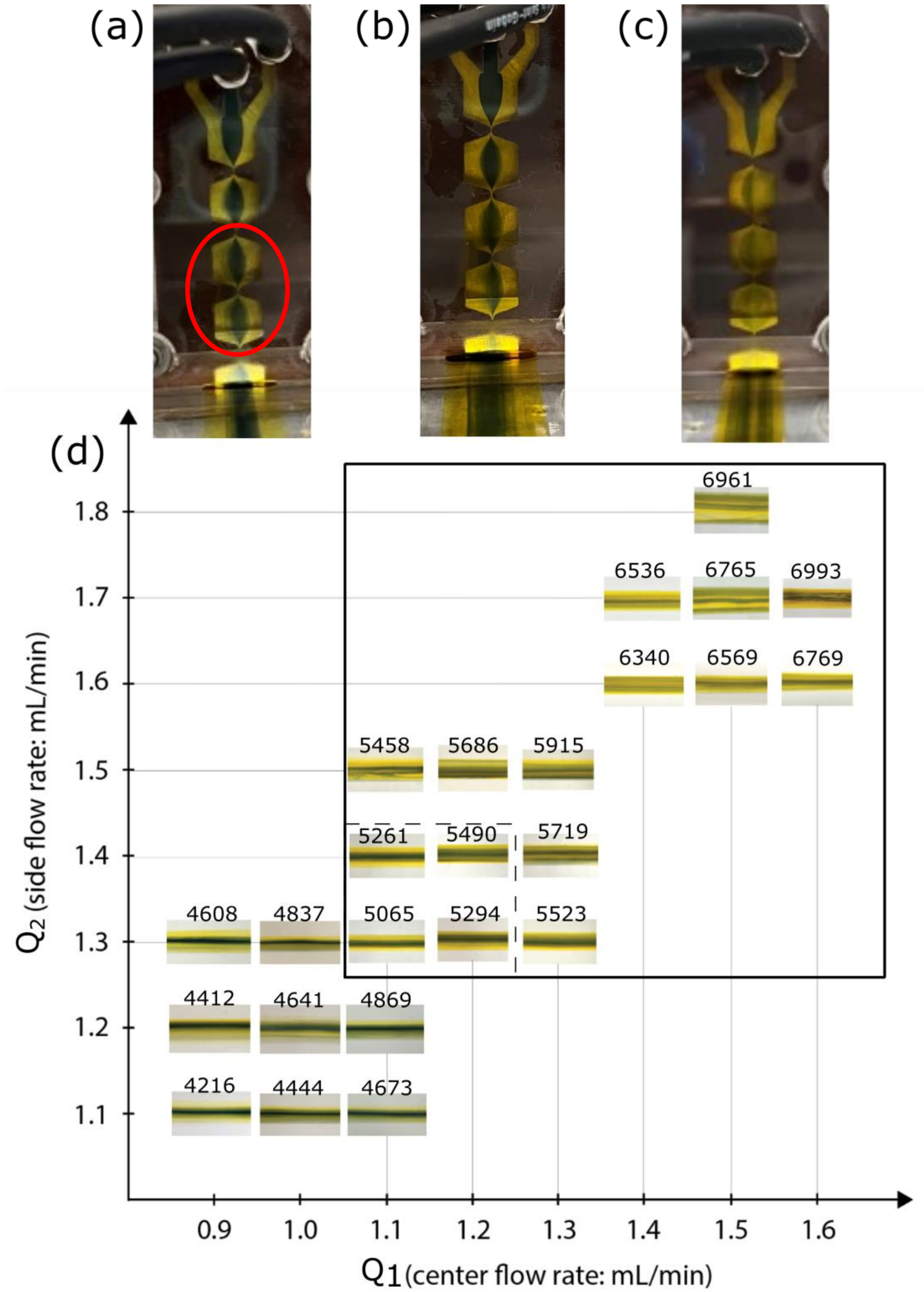

Figure 5.3 – PEDOT:PSS/PVA gradient film fabrication showing internal flow at (a) Pe < 5,000, (b) within Pe range with qualitfy film, (c) within Pe range but defective and (d) quality chart showing coating at different ranges of flow rates

As for the diffusion to occur, the center flow needs to have higher viscosity compared to the side viscosity. Unfortunately, PVA solutions with higher than 7.5 wt.% had higher viscosity than PEDOT:PSS and less viscous PVA resulted in coating defect, i.e. dripping. Therefore, the change in χ is not so feasible as PEDOT:PSS was used as is where it is difficult to increase the viscosity. Although, some combinations of Pe are still within the calculated range, the gradient does not seem to be formed as center flow domination is noticed. Moreover, the area that PEDOT:PSS covers are very narrow compared to that of PVA/PVA gradient films. Such phenomenon occurs due to the significantly low D value of PEDOT:PSS. Therefore, it is likely that the PVA – PVA concentrations are inter-diffusing into each other as the diffusion coefficient of PVA is high compare to that of PEDOT:PSS. Whereas, for the PEDOT:PSS/PVA gradient thin film, the PVA diffusing into PEDOT:PSS.

5.4.2 PEI/PVA Gradient Coating

25 wt.% PEI is slot die coated as a single fluid to verify its wetting stability on PET in Section 5.2.. Yellow food coloring is added for better visualization of the coating. The flow rate is set as 1 mL/min with coating gap of 0.2 mm and substrate speed of 11 mm/s. As shown in Figure 5.4, although the wetting properties show that the fluid should wet well on the PET surface, the 25 wt.% PEI exhibited non-wetting behavior on the PET substrate.

Figure 5.4 - Single fluid slot die coating of 25 wt.% PEI with yellow food coloring

Given the successful results of the PEDOT:PSS, 25 wt.% PEI is maintained as the center flow stream with 10 wt.% PVA as the side flow streams, since it has good wetting. The coating parameters are given in Table 5.2.

Yellow food coloring was added to PEI and blue food coloring was added to PVA for easier depiction of gradient structure, as done previously. As shown in Figures 5.5 (a) and (b), the gradient formed inside the die as expected and was maintained upon deposition, respectively. However, after drying, the green and blue regions, seemed to largely disappear as illustrated in Figure 5.5 (c).

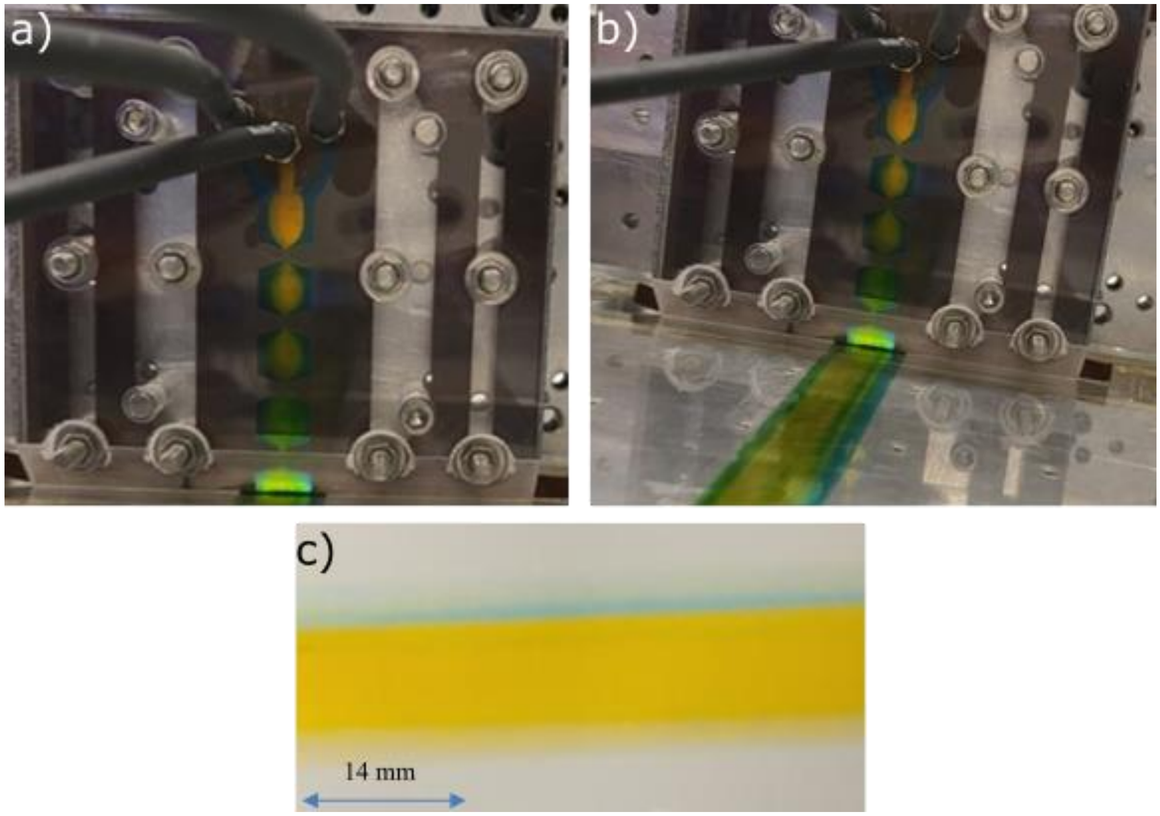

Figure 5.5 - Slot die coating of 25 wt.% PEI (center, yellow) and 10 wt.% PVA (side, blue) at (a) internal flow, (b) deposition and (c) after drying.

As such, PEI had to be evaluated with different food colorings. as a reaction between the two fluids could be the cause of such phenomenon. This is likely due to the high photodegradation nature of the PEI itself[107]. For this study, PEI dyed with blue, yellow, red and green (FD&C Yellow 5 and Blue 1) food coloring is drop casted onto PET, to minimize concerns of dewetting. All the drop casted samples are dried in 60ºC oven for 60 min and checked at 30 mins, to ensure no intermittent reaction occurred. As shown in Figure 5.6 (a), the blue color completely disappeared upon drying, and as shown in Figure 5.6 (d) the green color loses all traces of blue food coloring, leaving only yellow as visible.

As shown in Figures 5.6 (b) and (c), yellow and red remain visible in PEI, thus, red food coloring is used for visualization of PVA and PEI gradient thin films.

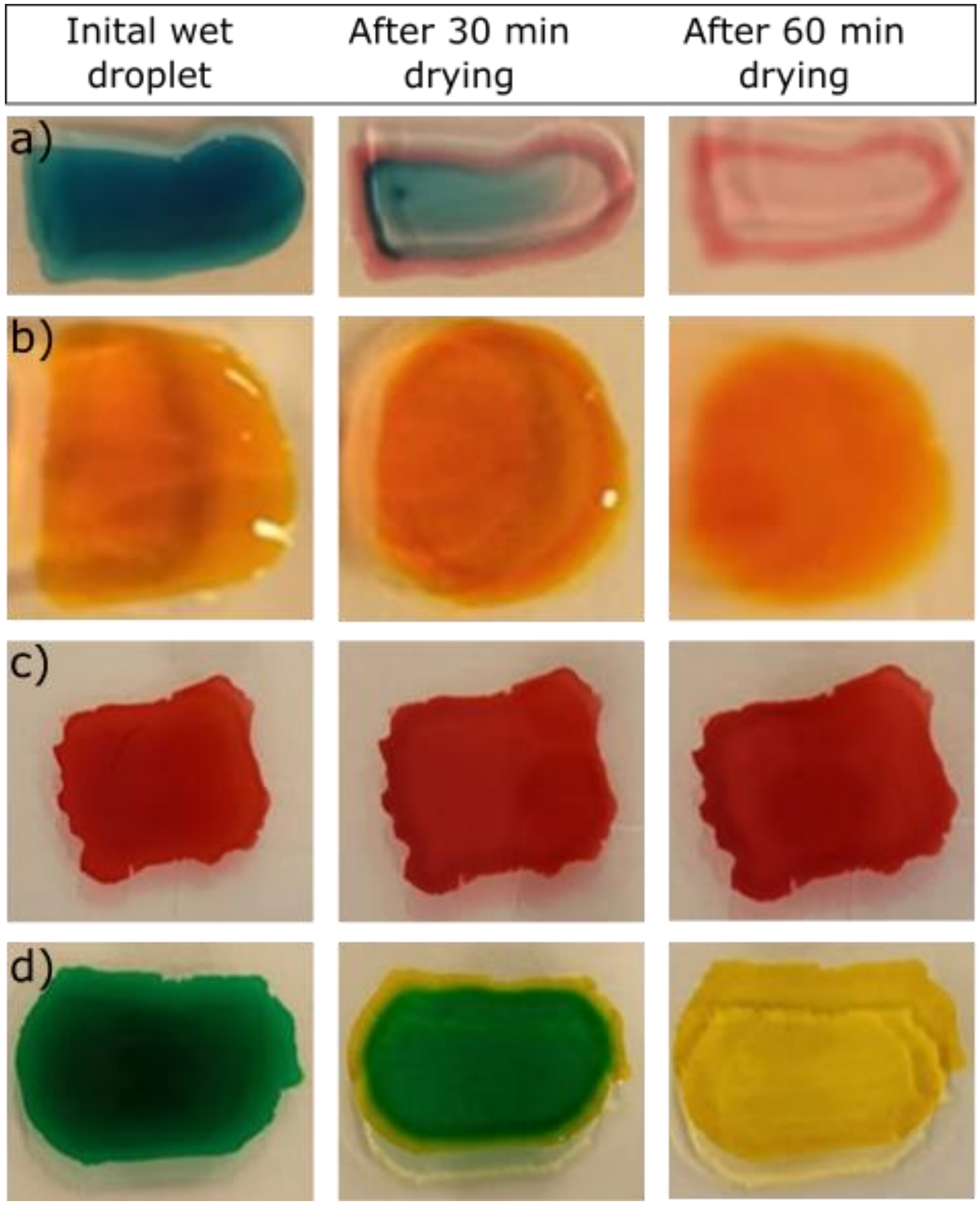

Figure 5.6 - Drop casted 25 wt.% PEI on PET with food coloring added with (a) blue, (b) yellow, (c) red and (d) green. Each image was taken at the initial wet droplet phase, 30 minutes drying and 60 minutes drying

As shown in Figure 5.7, using the same coating parameters Table 5.2, clear 25 wt.% PEI and 10 wt.% red PVA successfully formed a gradient and subsequently functionally graded thin films, at both the internal and external phases, respectively. The red color did not disappear after drying. However, after 1 week, the red color that diffused into the clear PEI disappeared as shown in Figure 5.8, due to the photodegradation of the material. However, this does not necessarily mean that the gradient does not exists. Characterization of the thin film must be performed to assess this.

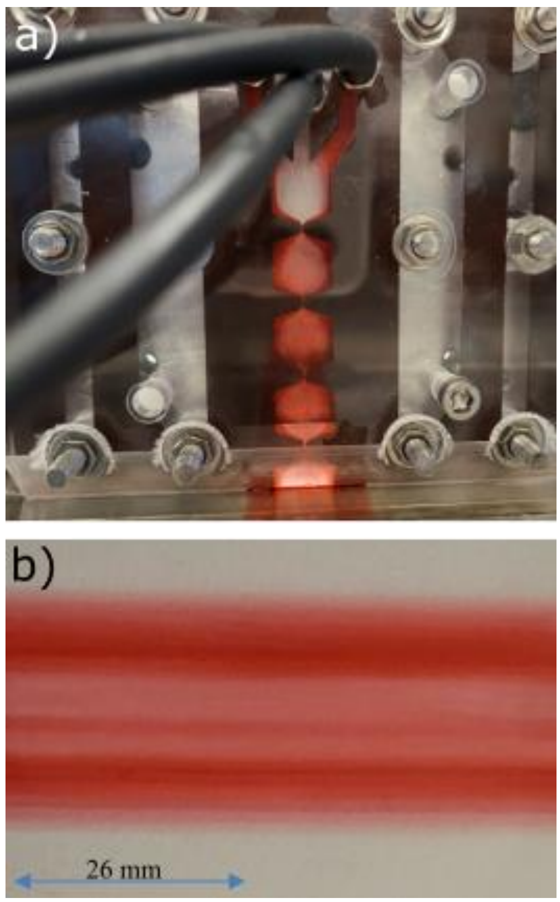

Figure 5.7 - Gradient patterned film coated using 25 wt.% PEI (center, clear, 1.0 mL/min) and 10 wt.% PVA (sides, red, 0.8 mL/min)

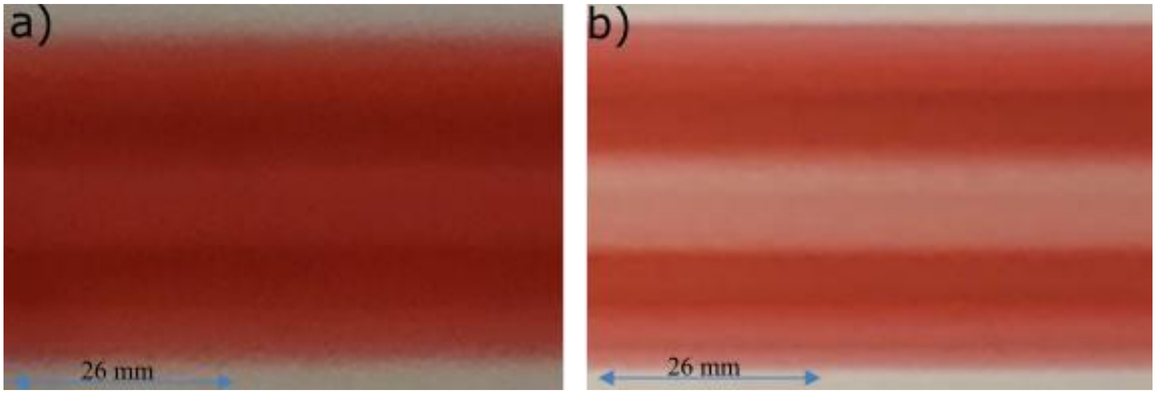

Figure 5.8 - Color difference of PEI/PVA gradient film with red food coloring at (a) right after drying and (b) 1 week after

5.5 Characterization of Functional Gradient Patterned Thin Films

5.5.1 Adhesion Test

It is well understood that PEDOT:PSS dewets PET, thus adhesion tests are not viable. However, due to the scaffolding effects of the co-deposition slot die coating process and formation of the PEDOT:PSS and PVA gradient thin film, it is important to assess the adhesion of the material. The tested PEDOT:PSS/PVA gradient film is shown in Figure 5.9. It is observed that the PEDOT:PSS started delaminating at the scratching stage, Figure 5.9 (b). However, the overall assessment is an evaluation of 0B, complete delamination, for the gradient structure, as would be expected given that PVA delaminates from the surface as well, as discussed in Section 3.5 as shown in Figure 5.9. One of the main reasons PVA and PEDOT:PSS delaminates off the PET film is because PVA is non-ionic and PEDOT:PSS is negatively charged when PET is negatively charged.

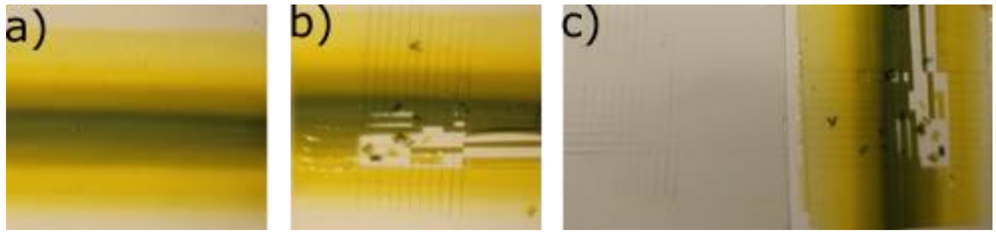

Figure 5.9 - Adhesion test result of PEDOT:PSS (center, 1.1mL/min) and 7.5 wt.% PVA (sides, 1.4 mL/min), where (a) represents Unscratched state, (b) represents Scratched state and (c) represents the tested state

As previously shown, PEI does not wet PET well. Even so, the gradient thin film of PEI and PVA is tested, as shown in Figure 5.10. Interestingly, the PEI is category 5B (0% delamination) and only the PVA delaminated, receiving a category 0B (100% delamination) assessment. Furthermore, the gradient regions exhibited very high adhesion to the PET surface also obtaining a category 5B assessment. The sample was allowed to photodegrade for a week, to assess whether this degradation would lead to poor adhesion later. As shown in Figure 5.11, the adhesion test results are maintained.

Fully blended 25 wt.% PEI and 10 wt.% PVA solution with 1:1 weight ratio is also tested to prove the efficiency of the gradient structure, as shown in Figure 5.12. It is observed that approximately 50% of the blend film delaminated, thus receiving category 1B (35% ~ 65% delamination). The high adhesion force of the PEI is anticipated, since it is positively charged, and PET film is negatively charged. It is well known that positively charged beads have higher adhesive forces on negatively charged surfaces[108].

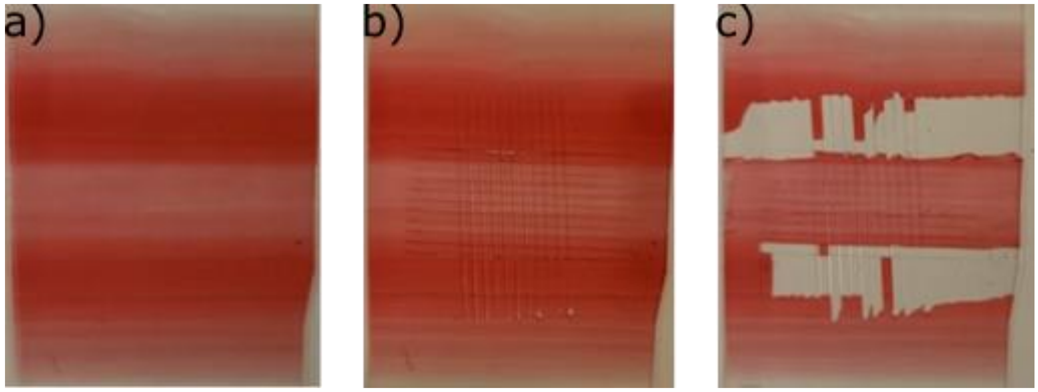

Figure 5.10 - Adhesion test result of 25 wt.% PEI (center, 1.0 mL/min) and red 10 wt.% PVA (sides, 0.8 mL/min). For each figure, (a) represents Unscratched state, (b) represents Scratched state and (c) represents post tape test state

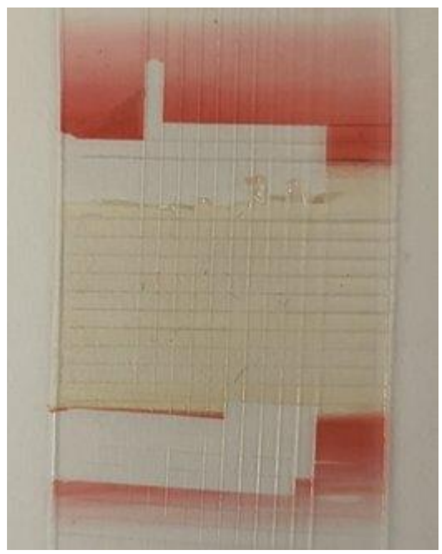

Figure 5.11 - Adhesion test result of 25 wt.% PEI (center, 1.0 mL/min) and red 10 wt.% PVA (sides, 0.8 mL/min) after one week

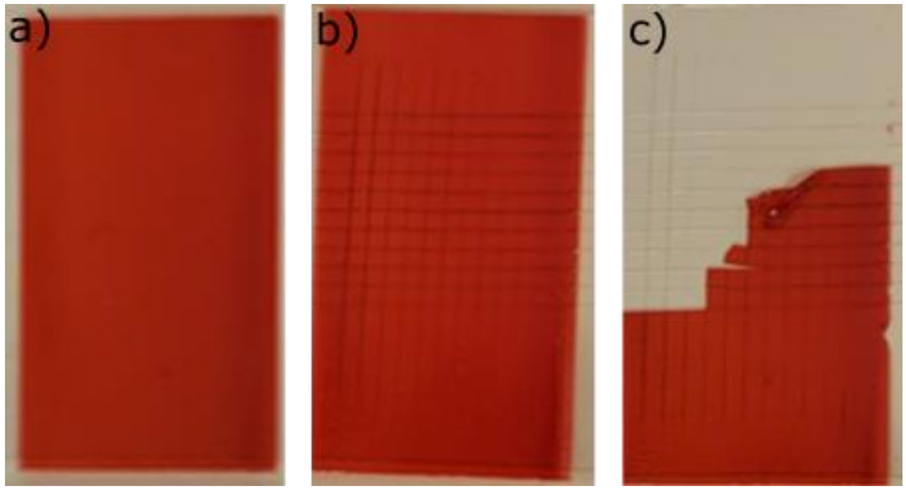

Figure 5.12 - Adhesion test result of 25 wt.% PEI and red 10 wt.% PVA fully blended at (a) unscratched state, (b) scratched state and (c) post tape test state

5.5.2 Electrical Characterization

Electrical conductivity is measured using the four-point probe method[109],[110] which is common technique for measuring the electrical conductivity of thin films. The probe contacts are lines of polished copper with widths of 25.5 μm each. The fabricated films are cut to the overall width of the probe, 4.6 mm width. The measurements are at three points on the samples, the center, gradient area, and one side material, as illustrated in Figure 5.13. In the previous work, although composites were used, showed that composite foam with gradient structure had 7 orders of magnitude larger conductivity than that of homogenous blending.

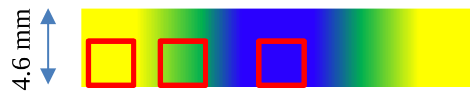

Figure 5.13 - Orientation of thin film used for electrical conductivity test with red box showing the actual measured areas

Electrical conductivity of blade coated PEDOT:PSS/PVA mixtures at different concentrations, provided in Figure 5.1 are measured. The thickness of each drop was measured using a micrometer. The coatings have uniform thickness of roughly 0.03 mm regardless the weight ratio, however, the width is not uniform. Based on literature, the conductivity of PEDOT:PSS ranges from 20 to 100 S/m[111] and PVA film has conductivity of 0.248 S/m[112]. . As shown in Figure 5.14, the conductivity of the raw materials and the blends with PEDOT:PSS ranged from 0.22 S/m to 83.3 S/m. This data can be used to verify the existence of a gradient film as well as aid with quantitative assessment the overall material concentrations within the measured regions. Such increase in electrical conductivity is also observed in previous works where the PVA/PEDOT:PSS blended film started to increase exponentially, similar to Figure 5.14, as the concentration of PEDOT:PSS started to increase[113].

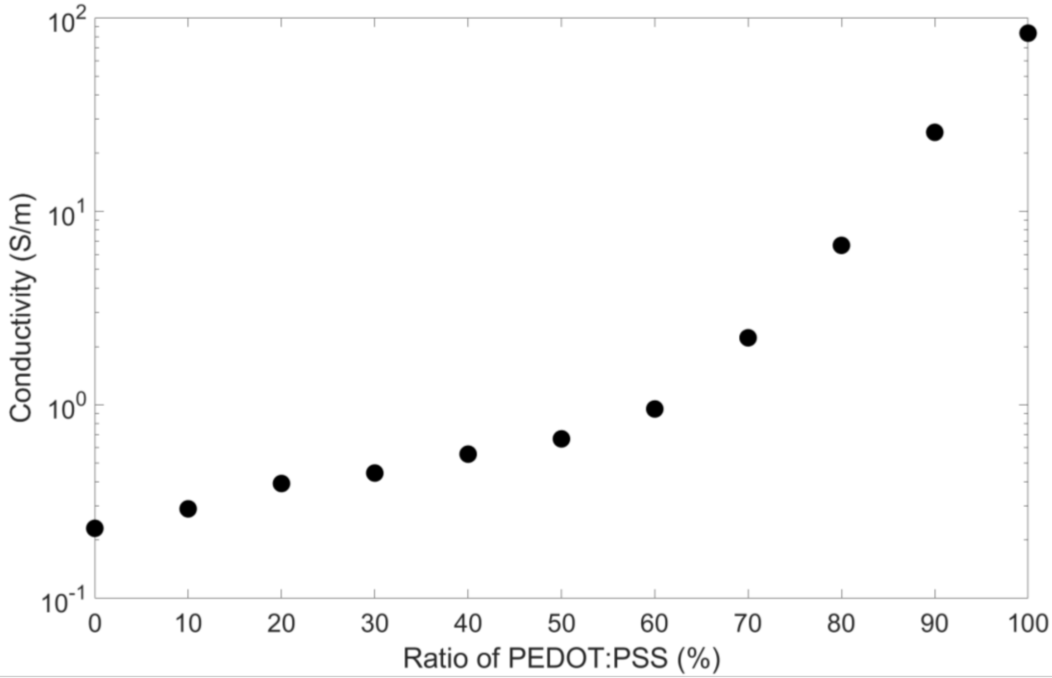

Figure 5.14 - Electrical conductivity at different PEDOT:PSS/PVA ratios, using the grid from Figure 5.1

The functionally graded thin film of PEDOT:PSS and 7.5 wt.% PVA are measured using four point probe. The thickness of the film are 0.03 mm. The PEDOT:PSS area had conductivity of 50 S/m, 7.5 wt.% PVA had conductivity of 0.36 S/m and the gradient area had conductivity of 6.7 S/m. the conductivity at the gradient structure are is same as the 80% PEDOT:PSS/PVA solution with 6.67 S/m, These results are a significant improvement on those reported by Liu et al.[114], for electrospun fully blended mixture of PEDOT:PSS and PVA solutions, which exhibited very poor conductivity, ranging from 0.00048 to 0.0017 S/m. However, these values are associated with much thinner film with thickness of 250 nm. Even so, the gradient structure produces higher electrical conductivity compared to that of the fully blended materials.

5.5.3 Microscopic Characterization

Since there are notable differences in the chemical make-up of each coating fluid, the quality of gradient structures is analyzed using Fourier-transform infrared spectroscopy (FTIR). NicoletTM iSTM 5 FTIR is used to analyze the actual chemical structure of the film, which can be aid verification for the gradient structure. To make a clear comparison, different types of thin film is tested, including plain PVA thin film, gradient thin film and completely mixed thin film. The library of materials embedded in the FTIR tool does not include PEDOT:PSS. Therefore, the measurement for PEDOT:PSS is compared to data in the literature[115]. For film containing PEI, gradient coating with and without food coloring were investigated to ensure the colors in PEI, as listed above, photodegraded instead of not mixing.

As shown in Figure 5.15, the PEDOT:PSS/PVA blends from the control grid, follow the FTIR curves of PVA, when the concentration of PEDOT:PSS is at or above 90% ratio. This is also comparable to the FTIR results from the gradient structure, where even at the PEDOT:PSS area, some of the peaks shown in PVA results are shown. It can be seen that the 80% PEDOT:PSS/PVA has similar FTIR graph as the gradient area closer to PEDOT:PSS boundary, as shown in Figure 5.16.

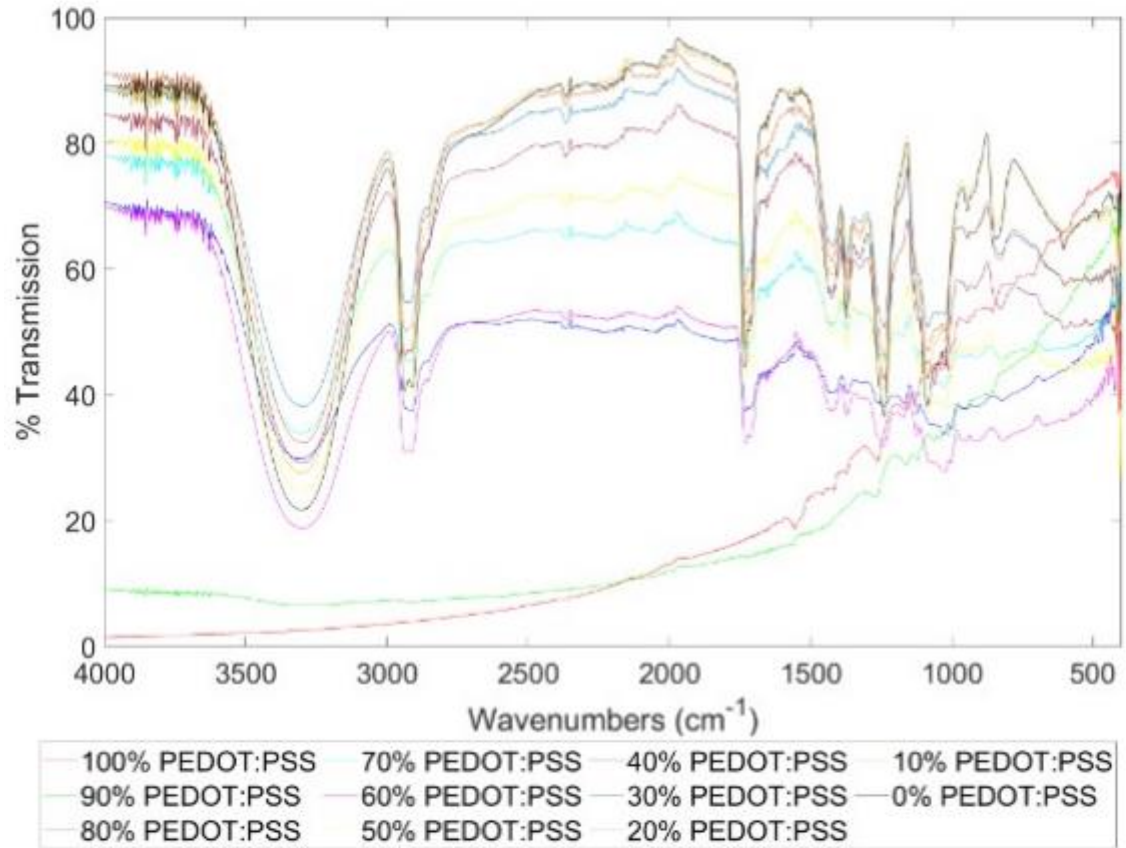

Figure 5.15 - FTIR results of different ratio of PEDOT:PSS/PVA

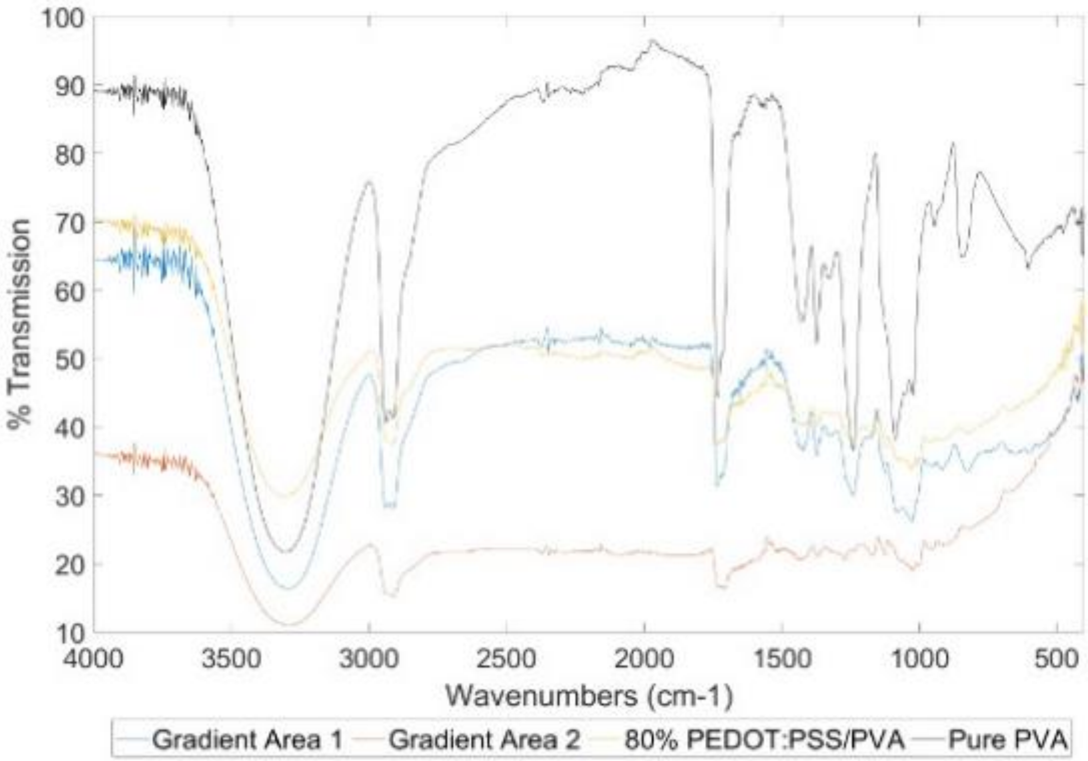

Figure 5.16 - FTIR results to compare 80% PEDOT:PSS/PVA mixture, pure PVA and the two gradient areas (closer to PEDOT:PSS & closer to PVA)

The FTIR results for slot die coated PEDOT:PSS/PVA gradient thin film is shown in Figure 5.17. PVA data had just over an 80% correlation with the FTIR database. The addition of food coloring is believed to reduce this value from 100%, even so, there are clear peaks that confirm the presence of PVA. Furthermore, the data from Figure 5.16 clearly shows the existence of a gradient as the percentage correlation to PVA decreased to 63%, 44% and then to 34% as the area of measurement moved into the PEDOT:PSS area.

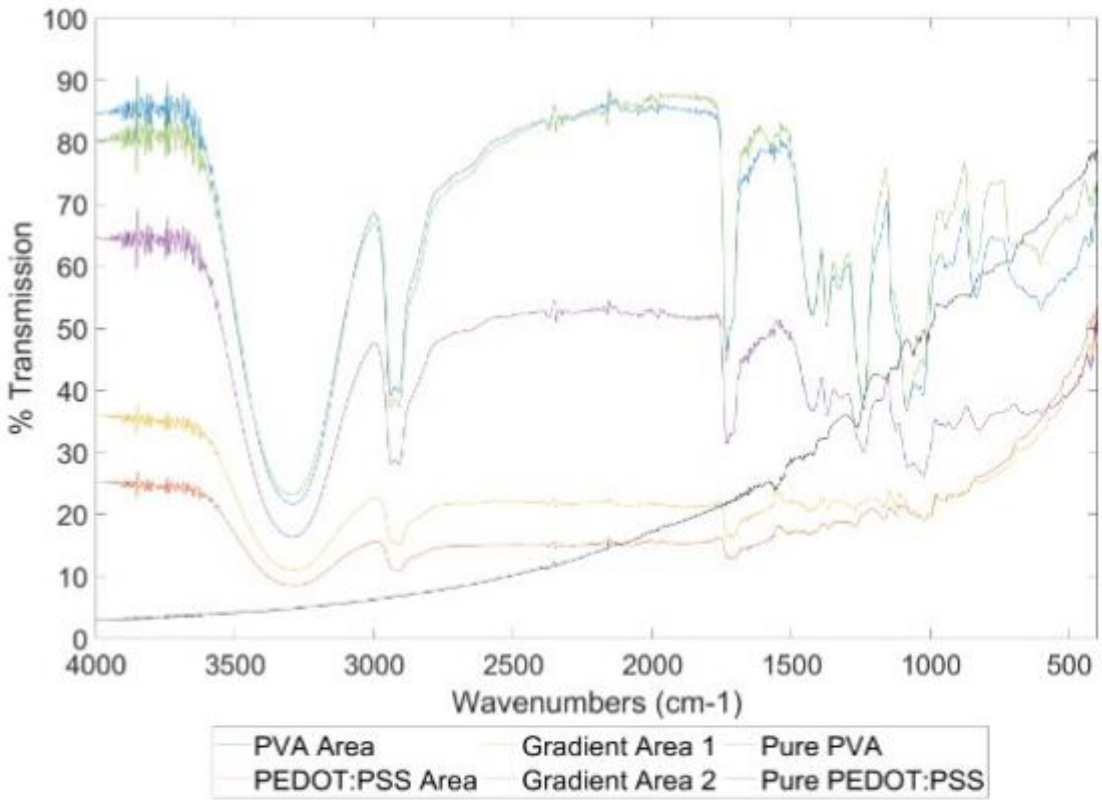

Figure 5.17 - FTIR % transmission results at different coating area

The FTIR result of PEI/PVA gradient thin film is as shown in Figure 5.18. It is observed that the % transmission peaks of the gradient structures lay between the PVA and PEI peaks. Also, the material library embedded in the FTIR tool compares the peaks with the database where the red PVA area had 74.64% correlation with the library data, the gradient area had 59% correlation and PEI, like PEDOT:PSS, has no correlations in the FTIR library. Comparing the data with the literature, the peaks looked very identical with very minor differences[116].

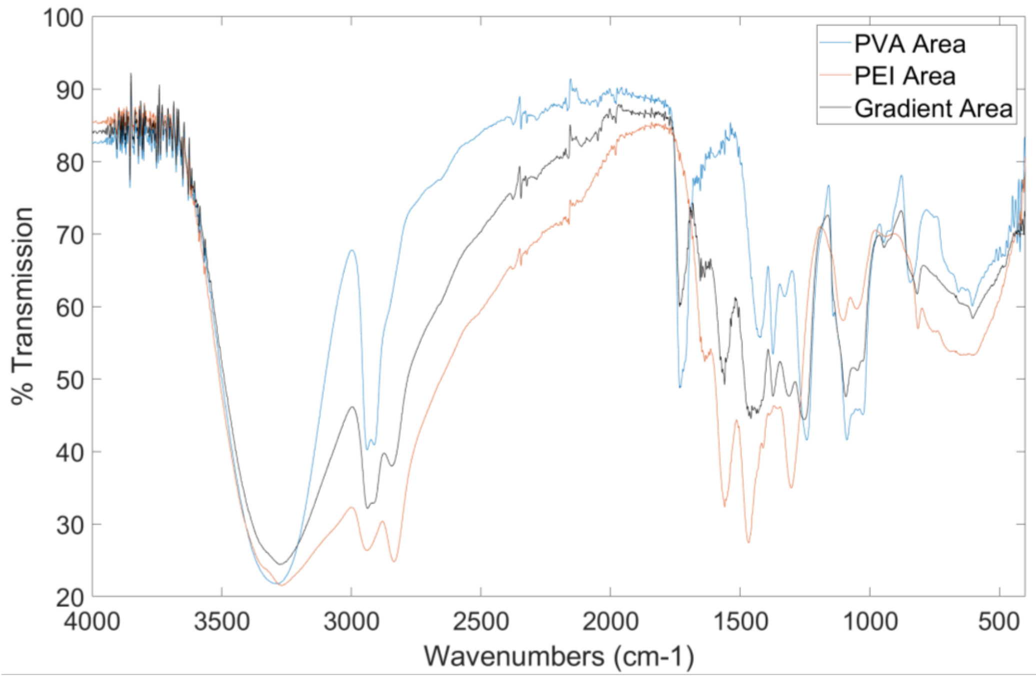

Figure 5.18 - FTIR result of 25 wt.% PEI and 10 wt.% PVA gradient coating with red food coloring added

To investigate the existence of photodegradation in PEI, PEI/PVA gradient with exact same coating parameters but without food coloring is fabricated and the FTIR result is shown in Figure 5.19. The PVA correlation data with the library is very similar with 78.07% in PVA area and 57.48% in the gradient area. Additional FTIR results for comparison are shown in Figure 5.20 (a) – (c), which illustrates that the red food dye has minimal impact and that the disappearance of red color after a week is indeed photodegradation.

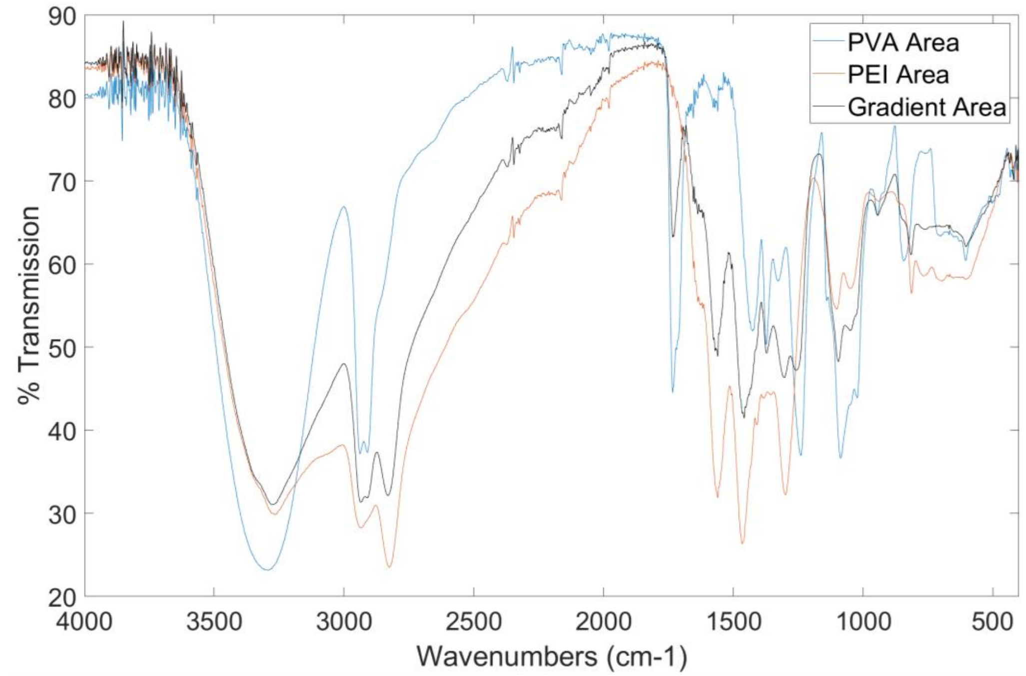

Figure 5.19 - FTIR result of 25 wt.% PEI and 10 wt.% PVA gradient coating without any food coloring added

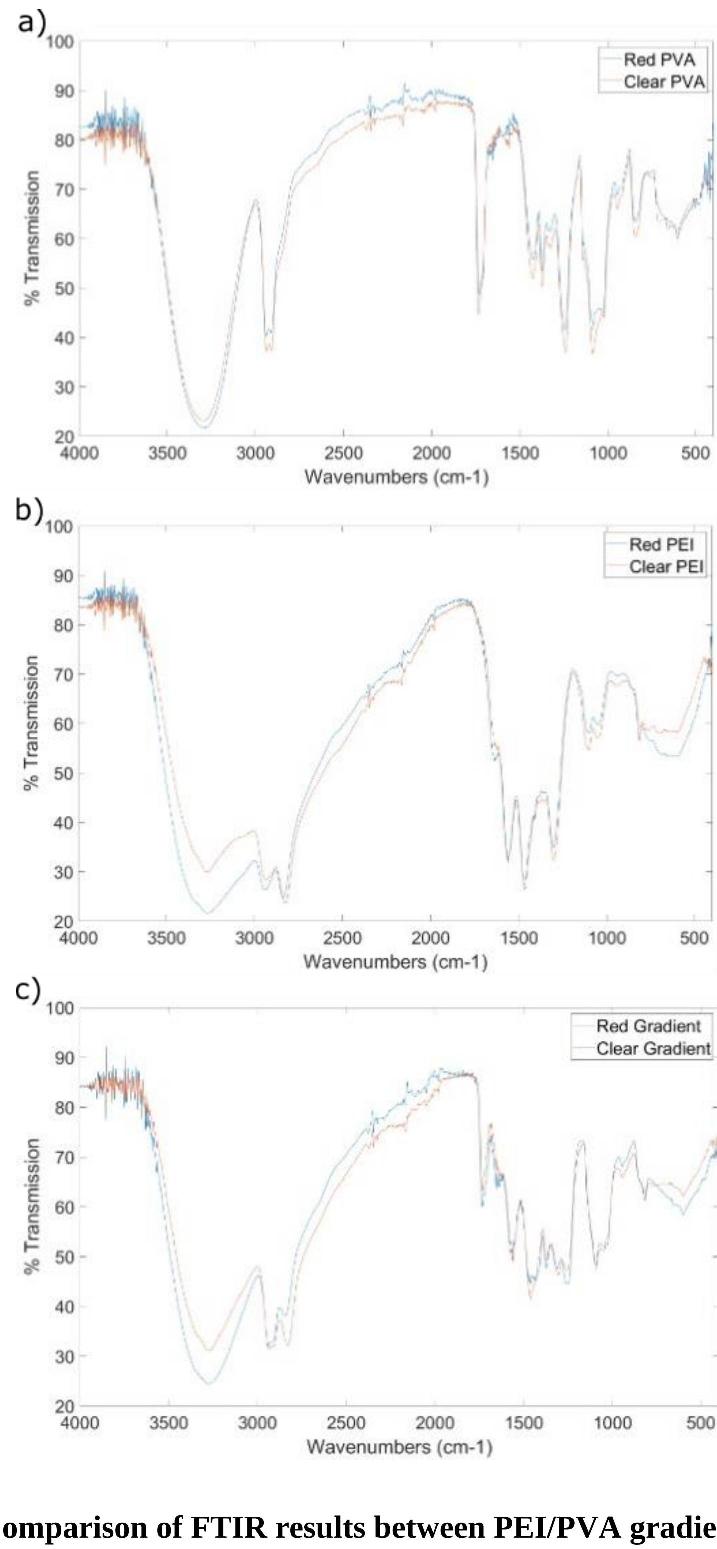

Figure 5.20 - Comparison of FTIR results between PEI/PVA gradient films with and without red food coloring at (a) PVA area, (b) PEI area and (c) gradient area

5.6 Conclusions

In this chapter, functional materials have been used to form functionally graded thin films, in an effort to exploit the enhanced material properties afforded by gradient thin film. PEDOT:PSS and PEI were chosen as the functional materials, due to their well-known properties, processability, and cost. The secondary fluid was PVA.

While these aqueous solutions generally have very poor wetting properties on the PET, stable coating were obtained by scaffolding the non-wetting fluids, PEDOT:PSS and PEI, with a wetting fluid, PVA. Functionally graded thin films of PEDOT:PSS/PVA and PEI/PVA were formed by calculating the flow rates based on the Pe.

Upon characterization, it has been found that the electrical conductivity of PEDOT:PSS/PVA gradient film was measured to be 50 S/m, 6.7 S/m and 0.36 S/m in the PEDOT:PSS, gradient and PVA areas, respectively. This result was compared to completely mixed PEDOT:PSS/PVA solution and it was noted that the conductivity of the 80% mixture has a similar value to that at gradient region. However, the results from FTIR showed that the gradient area had peaks closer to the PVA (more PVA content) than to the 80% PEDOT:PSS/PVA. This could indicate that even with lower PEDOT:PSS content, the gradient structure can create higher efficiency. Unfortunately, PEDOT:PSS/PVA gradient films have very poor adhesion. Conversely, the adhesion of PEI/PVA gradient film was tested and it was noted that presence of PEI improved the adhesive properties in the gradient area of the sample, where no delamination was observed. Although the PVA regions still delaminated, regions with PEI and PEI/PVA gradient showed highest adhesive force, even when compared to the adhesion of fully mixed PEI/PVA coatings. It was interesting to note that the photostability of PEI did not negatively impact the results.

CHAPTER 6. POSSIBLE METHOD FOR STRAIN STRESS TEST AND DELAMINATION: DIGITAL PHOTOELASTICITY

6.1 Introduction

Conventional approaches for determining the delamination of flexible electronics include buckling-driven delamination[117] and laser sheet blister profiling[118]. These methods are costly, time consuming, and not ideal for films without crystalline[119]. Hence, a new approach is needed. A potential method for analyzing delamination is a new approach called digital photoelasticity (DP)[120]. DP is an optical approach that utilizes digital algorithms to determine the principal stress difference and directions of planer stress. The stress changes detected may be due to applied loading, residual stresses, cracks, or coating thickness variation. Initial photoelasticity concepts conducted by previous authors[121,122,123] are based on single layer pure crystalline materials, because they have inherently two different light reflections. When light passes through a stressed semi-crystalline sample, like polymers polyimide, liquid crystal polymers (LCP) and polyethylene terephthalate (PET), a birefringence is also created. The paths correspond to the primary and secondary in plane stress. Due to automatized phase-shifting, photoelastic measurements are accurate and simplified to obtain the principal information while still having the advantage of being noncontact, whole-field, and low cost.

In this chapter, the utility of the DP method for analyzing delamination of thin slot die coated Ethylene Vinyl Acetate (EVA)[124] films that are used to encapsulate flexible substrates will be investigated to reveal the effective shear stress of the coating. EVA is introduced as a new material for this chapter as results in previous Chapters in this dissertation showed that PVA and PEDOT:PSS have poor adhesion on the PET and PEI, although had good adhesion on PET, was not used as it had poor wetting. Different concentrations of EVA are used to encapsulate plain polyethylene terephthalate (PET).The coatings are applied across a range of concentration. The exact locations of initial and propagating delamination are elucidated and the effect of film concentration is analyzed. This work provides a framework for identifying the regions most susceptible to delamination in flexible electronic devices, in a quick and cost effective way.

6.2 Materials

DuPont® EVA 250 resin is used as purchased. The EVA resin is dissolved in cyclohexane, purchased from VWR® to make two concentrations of EVA solutions 3.3 wt.% and 6.6 wt.%. The 3.3 wt.% EVA solution is made by dissolving 2 g of EVA 250 resin in 58 g of cyclohexane at 45°C for 20 min. The 6.6 wt.% EVA solution is made by dissolving 4 g of EVA 250 resin in 54 g of cyclohexane at 45°C for 30 min.

A stainless steel slot die is used to coat the EVA solutions onto various substrates. 100 µm thick polyethylene terephthalate (PET) film purchased from Goodfellow® is used not only as a substrate but also as a carrier web during the slot die coating process.Each substrate is cut to 18 cm by 2 cm, using a rotary trimmer, to meet the dimensional requirement of the Digital Photoelasticity. After the cut, each substrate was cleaned with Deionized water (DI water) and Isopropyl Alcohol (ACS standard), purchased from VWR®, using Kimtech® Kimwipes.

6.3 Methods

The slot die is mounted on a Roll-to-Roll (R2R) imaging system that consists of a carrier web with controlled velocity and a volumetric flow pump equipped with a syringe, to fabricate uniform coatings of EVA solutions. The distance between the slot die and the substrate, coating gap, is set to 150 µm. The flow rate of the EVA solutions and velocity of the carrier web are set to 1 $\frac{\mathrm{mL}}{\mathrm{min}}$ and 3 $\frac{\mathrm{mm}}{\mathrm{s}}$, respectively. A camera with microscope function located beneath the deposition regions, helps to instantaneous ensure the quality of the coating. After coating a layer of EVA 250 solution onto a substrate, it is solidified in air for 15 min and then placed into a 120°C oven for 3 h to cure. The final film thickness for a single layer is 15 µm.

Contact angle measurements are made using a Rame-hart® Goniometer to ensure good wetting between the slot die and EVA solutions as well as the EVA solutions and the substrates. ASTM 7334-08 standard is followed. Adhesion test are conducted following the ASTM D3359 standard using cross cut scratcher and Scotch® tape, to verify the results of the DP.

The DP is used to optically inspect the stress-strain of the EVA samples. The DP set-up is positioned so that each sample is placed on a Test Resource's universal test machine (UTM) between motorized wave plates. A UTM is used to apply tensile loading on to the sample while monitoring the displacement and force. An even load is placed across each sample by clamping the samples across the width (i.e., 2 cm). The clamps are spaced 10 cm apart, exposing the actively strained area, hence the other 8 cm along the length are used for clamping. The clamped locations are marked to ensure that the exact same locations are being measured. Figure 6.1 shows better representation of the overall DP setup, but not into scale. The data collected by the camera is then analyzed by Polaritek® software which is novel program that is specifically designed for the DP setup. Currently, the developed software is compatible with Windows® 7 system and efforts are still being made to form a compatible software for new Windows® systems.

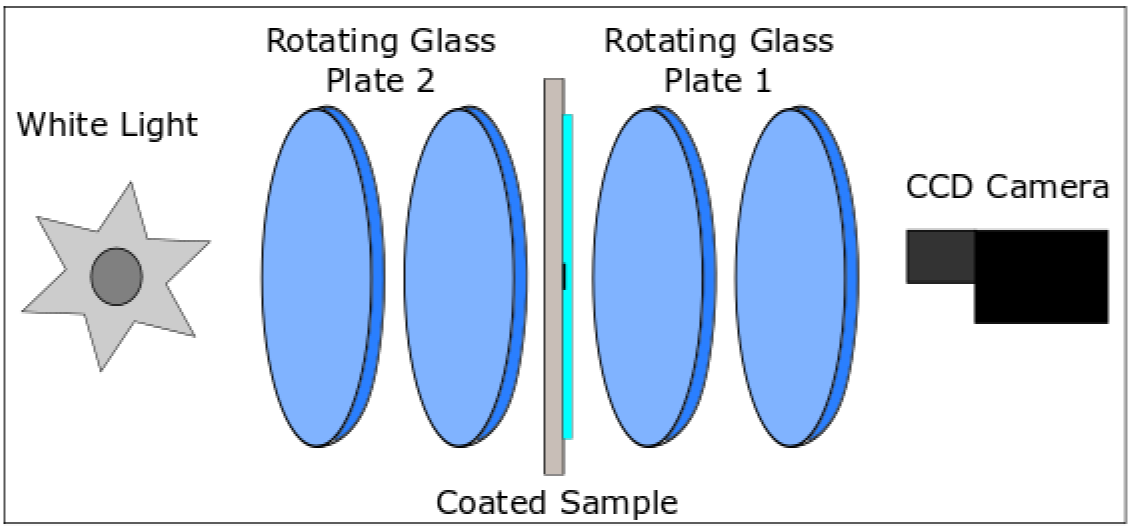

Figure 6.1 - Side view schematic of overall DP setup

Due to the drawing process, tensile residual stresses can generate in the PET. To account for this, initial digital photoelasticity measurements are made on uncoated PET in an unstressed state to characterize the residual stresses in each sample. After the measurement of each uncoated PET substrate, EVA 250 coating is applied and cured using the protocol stated above. Then, the EVA 250 coated sample is placed in the UTM tool and the DP measurement is made in an unstressed state. This is followed by four strain loadings, 1%, 2%, 3%, and 5%., at which DP measurements are made. To obtain the final measurement, the residual stresses found in the PET are decoupled from the measured samples.

6.4 Results and Discussion

Wetting of EVA 250 on the tooling and substrate materials is important, to ensure good spreading and adhesion. For 3.3 wt.% EVA 250, the contact angles are 46.94° and 44.72° on stainless steel (i.e., the slot die material) and PET (i.e., the substrate), respectively. Measurements for 6.6 wt.% EVA 250 yielded similar results, 47.47° and 46.20° on stainless steel and on PET, respectively. This demonstrates that the concentration of EVA 250 has a limited impact on the wetting properties and the material can be easily coated on the substrate, since the contact angle is relatively low.

The effect of thickness and viscosity on the percent strain for low and high concentrations of EVA 250 solution coated on PET at thicknesses of 15 or 45 µm, are analyzed using Figure 6.2 to 6.4. For each DP data set, the stress in plain PET is initially measured, then stress in the encapsulated material is measured at strains of 1% to 5%, and the grab profile is extracted. Surface defects on the encapsulant can be observed from grab profiles by alteration in color of the light source passing through the film. By correlating the stress and grab profiles, the location for enhancing the encapsulation can be detected.

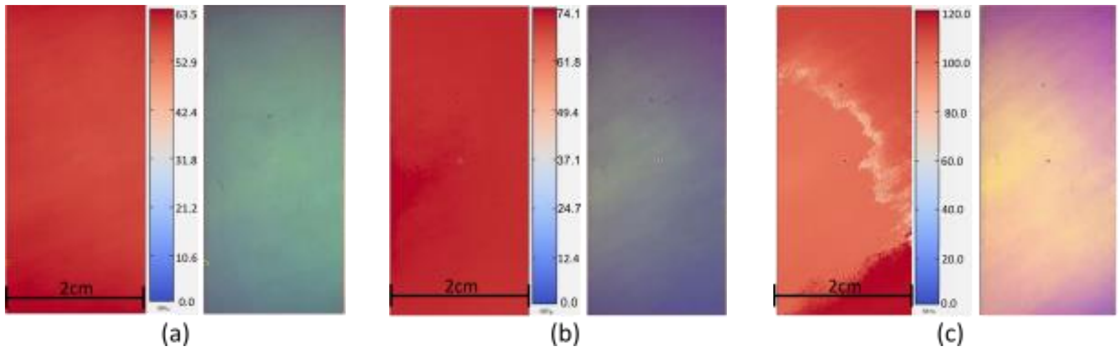

Figure 6.2 - Stress and Grab profiles of plain PET at (a) 0% strain, (b) 5% strain and (c) 10% strain.

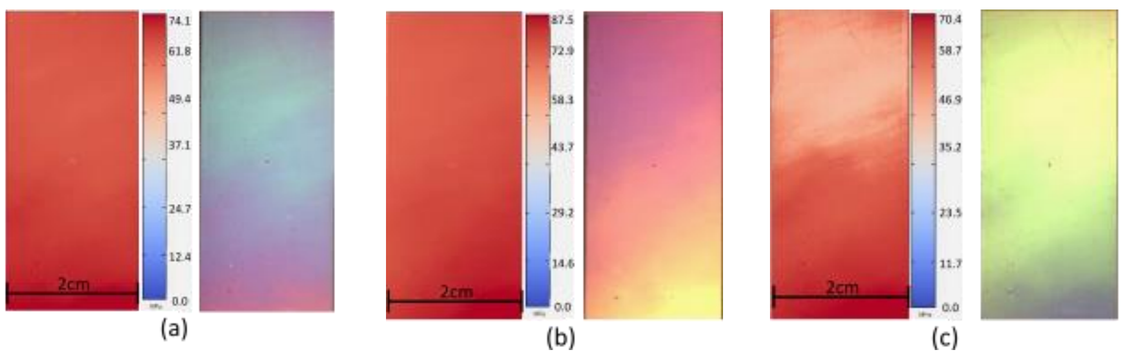

Figure 6.3 - Stress and Grab profiles of (a) plain PET and single coating (15 um) of 3.3 wt.% EVA on PET at (b) 1% strain and (c) 2% strain.

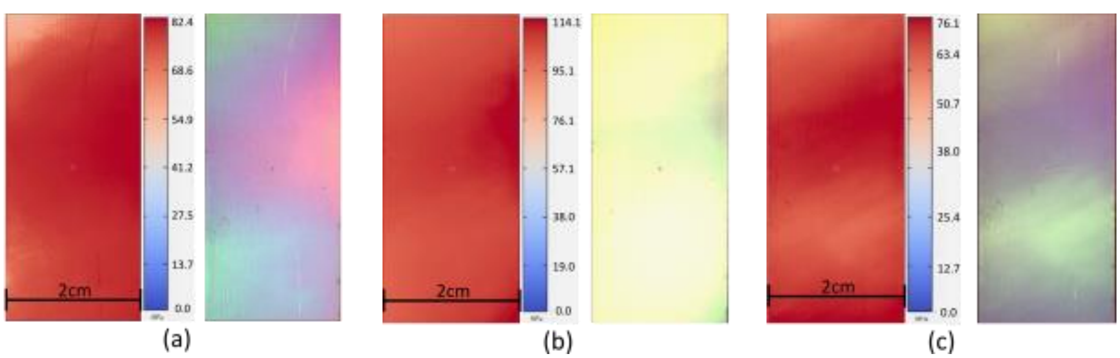

Figure 6.4 - Stress and Grab profiles of (a) plain PET and single layer coating (60 um) of 6.6 wt.% EVA on PET at (b) 3% strain and (c) 5% strain.

As observed in Figure 6.2, no significant changes occur in plain PET until 10% strain is reached; hence, delamination and other observed defects at thresholds below 10%

strain are attributed to the EVA 250 encapsulant. As shown in Figures 6.4, a single layer of 3.3 wt.% EVA 250 exhibits signs of delamination at 2% strain, along the lower right of the sample. This means that discontinuities or other defects are more likely found in this region. Thicker coating of the encapsulant extends the amount strain that the sample could undergo before delamination, by up to 40%[125]. When the concentration of EVA 250 is increased by 50% and coated PET, the percent strain to delamination also increased. When the concentration of the solution increased, the thickness also increased. At 6.6% wt. concentration, the thickness of the film was 60 um. As shown in Figure 6.3, delamination initiated between 2% to 3% strain, which is a 50% increase. However, as shown in Figure 6.4, at increased thickness, delamination was not exhibited at up to 5% strain. For all tests, the delamination started to form from the perimeter of the samples.

The interfacial strength between the coating and the samples is obtained by conducting adhesion tests, which are shown in Figure 6.8. At low concentration and thickness, the adhesion force is very low with classification of 0B. In this case, nearly 70% of the coating is delaminated, as shown in Figure 6.6 (a). Slight improvements in adhesion are observed when the thickness of 3.3 wt.% EVA coated on PET is increased; the adhesion force is then a e classification. Whereas when the concentration is high (6.6 wt.%) the adhesion strength greatly improved to a 3B classification which corroborates the stress-strain results of the DP measurements.

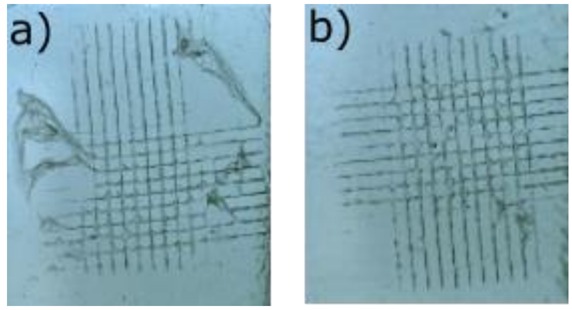

Figure 6.5 - Results of adhesion test of (a) 3.3 wt.% EVA 250 and (b) 6.6 wt.% EVA 250 solutions on PET substrate

6.5 Conclusions

Digital photoelasticity has been found to be an effective method of analyzing the strain percent of flexible transparent encapsulations. The optical measurements allow for low cost, quick and accurate assessment of delamination due to strain. For encapsulants that cover a wide area, it has been shown that delamination initiates along the edges of the material. It has been found that increasing the viscosity of the coating material can significantly reduce delamination as it increases the thickness. It has been found that as these metrics increase, the adhesion forces increase thereby increasing the resistance to strain. Unfortunately, due to the current software compatibility, the DP measurements in any of the previous gradient structures fabricated in Chapter 3 and 5 are unsuccessful. Therefore, in the future, when the new software compatible with the new computer systems are developed, the usefulness of gradient structure can be experimented as previous work showed the gradient structures can improve the film's mechanical properties[12,126].

CHAPTER 7. EMPIRICAL ANALYSIS OF GRADIENT STRUCTURE

7.1 Internal Passive Mixing Analysis

7.1.1 Past Contribution on Length and Time Scales

The mixing phenomenon can be explained mathematically to verify the experimental and computational results. The Pe number, given in Equation 3.1, plays a critical role in determining the onset of mixing. The previous experimentation was based off the statement that for the mixing to occur, the range of Pe is from 5,000 to 15,000, however, as found by Ottino et al.[127] if the value ranges from 10 to 100,000, mass transfer of the fluid is faster than that of the diffusion. However, this does not mean that there is no diffusion.

The time it takes for diffusion to occur depends on the diffusion coefficient (D) of the material and the width of the channel. The diffusion time to cover half the flowing width, t_D, can be calculated using Equation 7.1.[128] To obtain this equation, it was assumed that the diffusion of the particles is random and the mixing only occur due to the diffusion.

$$t_D = \frac{w_c^2}{8D} \tag{7.1}$$

where, w_c refers to the width of the flow channel.

For a typical rubbery polymer, D ranges from 10^{-13} to 10^{-8} m^2/s and to induce diffusion during microfluidic flow, either a larger diffusion coefficient or narrower flow width is required. The diffusion distance (δ_x) can be specified as Equation 7.2, which predicts the width of the diffusion of one fluid into another. To obtain this relationship, it was assumed that: 1) only molecular diffusion is occurring, 2) the diffusion only happens in the cross-sectional direction of the channel and 3) due to the parabolic nature of the velocity profile, the time it takes for the side flow fluids to exit the channel is longer meaning that the mixing will not occur at the location regardless of the width.

$$\delta_x = \sqrt{Dt} \tag{7.2}$$

7.1.2 Implementation to Experimental Result

Following the investigations from the previous work, the theoretical formation of various gradient structures fabricated in this work are verified. Prior to the calculation, it is assumed that: 1) overall flow is steady state, 2) zero velocity and flux at the wall, 3) the three flows take up approximately 1/3 of the width at the microchannel and 4) leakage minimized. For PVA, the diffusion coefficient[60, 61] (D) is 2×10^{-9}. The width of larger chamber, less the converging areas, is 10 mm and following D for 20 wt.% PVA and 10 wt.% PVA stated in Section 2.3, t_D for each equal to 41,667 sec and 15,625 sec respectively. Thus, the time required for diffusion to occur in a large channel, exceeds what is plausible for the slot die coating process which is on the order of ones of seconds. Hence the importance of incorporating microchannels into the flow domain. As an example, the time required for 20 wt.% PVA and 10 wt.% PVA to start mixing at the microchannel has been measured and found to take 3 sec, which is the allotted time for diffusion to occur.

The microchannels created by the shims are $0.2\,\mu$m . Now, t_D decreases significantly in the microchannel and equals 16.67 sec and 6.25 sec for 20 wt.% PVA and 10 wt.% PVA, respectively. While significantly lower, these values still exceed the time required for diffusion to ensue. If each flow stream through the microchannel is assumed to be exactly 1/3 of the microchannel (~0.067 μm), the time for diffusion into the half the width (~0.033 μm) decreases to 1.85 sec and 0.82 sec for 20 wt.% and 10 wt.% PVA respectively, which aligns with the timescale of the coating process.

Using this information, it is expected δ_x is ~0.0236 mm at the microchannel. The diffusion width of the newly formed flow streams after mixing (Fluid 1, gradient, Fluid 2, gradient, Fluid 1), should remain constant as the fluids flow to a subsequent microchannel, because, theoretically there is no mixing occurring in the large chamber. The width of the gradient streams to the width of the overall flow stream do not have a linear correlation.

The material properties for PEDOT:PSS/PVA are analyzed. The width of the large cavities is 0.1 mm and the width of the microchannels is 0.2 mm .The diffusion coefficient (D) for PEDOT:PSS is $1.5 \times 10^{-12}\ \mathrm{m^2/s}$[129] and approximately $2 \times 10^{-9}\ \mathrm{m^2/s}$ for 7.5 wt.% PVA. Using the values for the large chamber, t_D for PEDOT:PSS is 6.94×10^9 sec and for 7.5 wt.% PVA is 370 sec, which indicates no mixing. Assuming that the flow covers around 1/3 of the microchannel width, t_D can be reduced, as shown previously. However, in the microchannel, t_D for PEDOT:PSS is still high, 3.09×10^5 sec, however, 7.5 wt.% PVA is 0.617 sec. Thus, it is expected that the PVA will diffuse into the PEDOT:PSS. Since the same geometry is maintained, δ_x is 0.0236 mm.

For PEI, D ranges from 1×10^{-10} to $2.5 \times 10^{-10}\ \mathrm{m^2/s}$[130]. However, it is important to note that the molecular weight of the reported material is different than that used in this work, thus the effect of concentration is unknown. However, in the following calculations it is assumed that the D for PEI lies within the range. Moreover, it is known that as the mass fraction of the solvent increases, the D also increases.

Given this, t_D, in the large chamber ranges from 1.25×10^5 sec to 50,000 sec for PEI depending on D and in the microchannel it ranges from 5.56 sec to 2.22 sec. The t_D of 10 wt.% PVA is 15,625 sec in the large chamber and 0.69 sec from the microchannel. Since the same geometry is maintained, δ_x is approximately 0.0236 mm in the microchannel area.

The mixing width is predicted to be approximately 0.0236 mm. Based on the results from CHAPTER 4, it is found that the mixing width for both experimental and CFD analysis are equal to 0.019 mm, which is lower than the predicted value. This error is believed to be due to the simplifying assumptions, the uniformity of the cut shim, the resolution of the imaging tool and subsequently the accuracy of the measurements. Since the error is within 20%, it is assumed acceptable.

7.2 Deposition Phase Analysis

7.2.1 Past Contribution on Slot Die Coating at Deposition

Research has been conducted to understand the behavior of coating fluids in the coating bead (the fluidic region just after deposition) during the slot die coating process. However, most of this research has been based on a single fluid. Parsekian et al[131], investigated the coating of two fluids, however, their work did not consider the behavior of the fluids in the coating bead or the formation of gradient. Kang et al[132] investigated the operating conditions of a single fluid coated in several distinct lines using slot die coating to predict the minimum thickness and the width of the deposited film. They investigated the impact of two factors that has impact on the slot die coating: viscocapillary model (Equation 7.3) and pressure drop in terms of Capillary Number (Ca) (Equation 7.4)[133]. The Ca is dimensionless number that shows the ratio of viscous force to the surface tension which is shown by Equation 7.5.

$$\Delta P_{\mathrm{max}} = \frac{2\sigma}{\mathrm{H} - th_{min}} \tag{7.3}$$

$$\Delta P_{\mathrm{max}} = 1.34\mathrm{Ca}^{2/3}\frac{\sigma}{th_{min}} \tag{7.4}$$

$$\mathrm{Ca} = \frac{\mu V}{\sigma} \tag{7.5}$$

In the above equations, σ represents the surface tension of the material, h is the coating gap, th_{min} is the thickness of the produced film, μ is the viscosity of the material and V is the speed of the substrate. From here, thickness can be calculated by equating Equation 7.3 and 7.4 with implementing Equation 7.5 into Equation 7.4 as shown in Equation 7.6.

$$th_{min} = \frac{H}{1+1.49(\frac{\mu V}{\sigma})^{-\frac{2}{3}}} \tag{7.6}$$

Investigation of actual wet thickness (th_{wet}) can be determined using the continuity equation. To obtain Equation 7.7, it is assumed that the coating bead is in 2D steady structure[41,134,135] and the Q and V combinations do not create any known coating defects[41].

$$th_{wet} = \frac{Q}{V*w} \tag{7.7}$$

By observing the model relating to the coating parameters, V, Q and H, the width of the resultant coating can be predicted. The pinning of the fluidic materials on the die lip and the substrate. It is known that coating beads create advancing contact line that moves along the contact line which causes the spreading. Parsekian et al. creates a mathematical model based off the experimental results to predict the spreading and the overall width at the deposition of slot die coating. The dimensional analysis starts with Equation 7.8 shown below to calculate the line-of-fit represented by Π_a:

$$\Pi_a = Re^{0.5} \cdot Ca^{-1} \cdot H^{*-2} \tag{7.8}$$

where, Re is the Reynolds Number and H* represents the dimensionless length ratio at the die lip. Re has been modified by the author as shown in Equation 7.9 and H* is also shown in Equation 7.10.

$$Re = \frac{\rho {v_{avg}}^2}{\frac{\mu V}{H}} \tag{7.9}$$

$$H^* = \frac{H}{(L_u + L_d + G)} \tag{7.10}$$

where, v_{avg} is the average flow velocity followed through to the die lip represented by Equation 7.11. In Equation 7.10, L_u is the upstream die lip length, L_d is the downstream die lip length and G is the thickness of the shim.

$$v_{avg} = \frac{Q}{wG} \tag{7.11}$$

To implement the experimental data into the linear regression, a piecewise empirical model is formed for the advancing fluids as shown below:

$$w_a{}^* = A_a \ln(\Pi_a) + B_a \text{ for } 0 < w_a{}^* \leq w^*_{\text{II-III}} \tag{7.12a}$$

$$w_a{}^* = C_a \ln(\Pi_a) + D_a \text{ for } w_a{}^* > w^*_{\text{II-III}} \tag{7.12b}$$

where, $w_a{}^*$ is the dimensionless width shown as $w_a{}^* = w_a/w$ and $w^*_{\text{II-III}}$ is the range dimensionless width when the pinning starts to occur. Initially, $w^*_{\text{II-III}}$ is set to $(L_u + L_d + G)$/w. Note that only advancing calculations are investigated for this dissertation as it is assumed that the film widths created are based on a steady state, non-stopping system.

7.2.2 Implementation to Experimental Result

For 20 /10 wt.% PVA gradient structure, the thickness is measured to be 68.70 µm, 51.32 µm and 55.72 µm in the center area, side area and gradient area, respectively. The calculated th_{min} at the center area is 47 µm and at the side area is 8 µm. For the theoretical th_{wet}, it is calculated that at the center is 68.62 µm and at the side is 49.01 µm. As shown in Figure 7.2, comparing the theoretical and experimental results, the thicknesses of the center area (20 wt.% PVA) have 0.029% error but the thicknesses of the side areas have 4.71% error. Such error can be due to the fact that the calculation does not consider mixing and the creeping effect of the fluids into the space between die blocks and shim as the measured thickness is from the dried film which means that experimental th_{wet} should be larger.

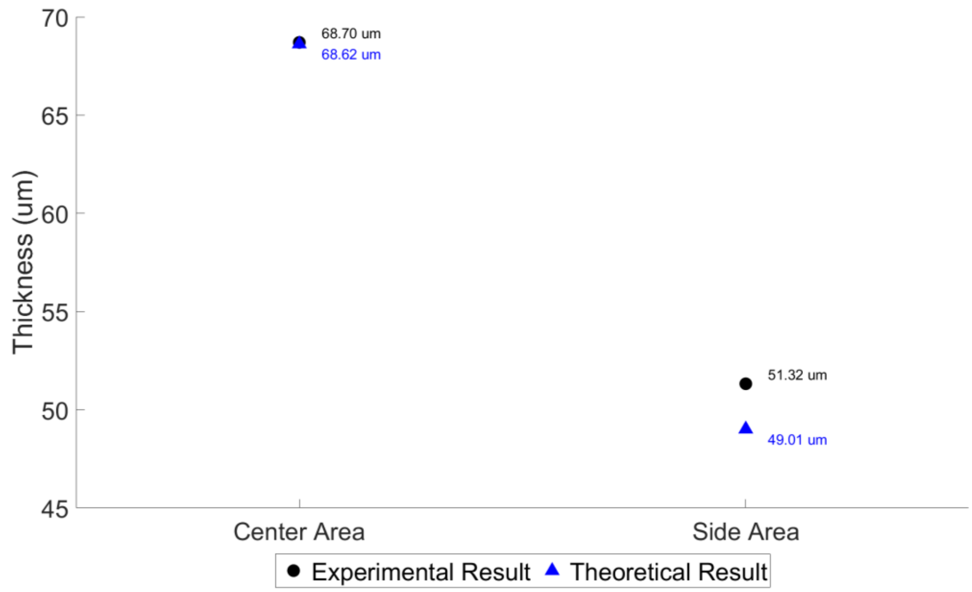

Figure 7.1 – Comparison of experimental and theoretical thickness at center area and side area

For the width, some investigations are done similar to what was done in CHAPTER 3 where Q_2 is controlled to observe effect of change in Q_1, and vice versa, on the overall, center and side width of the coating. As shown in Figure 7.3, the side widths are kept constant to 4 mm regardless of the increase in Q_1 but the total width increased from 15 mm to 16 mm then to 18 mm. The center width also increased as Q_1 increased from 5 mm to 7 mm then to 10 mm. When investigating the effect to side flow rate on the width, it is noticed that the side width increased from 3 mm to 5 mm then to 8 mm. The total width also increased from 15 mm to 18 mm then to 22 mm as Q_2 is increased. However, the center width decreased from 7 mm to 6 mm then stayed at 6 mm as shown in Figure 7.4. Such phenomenon is understandable as it is known that the spreading effect occurs with the peripheral fluids and less viscous materials spread more as discussed in CHAPTER 3.

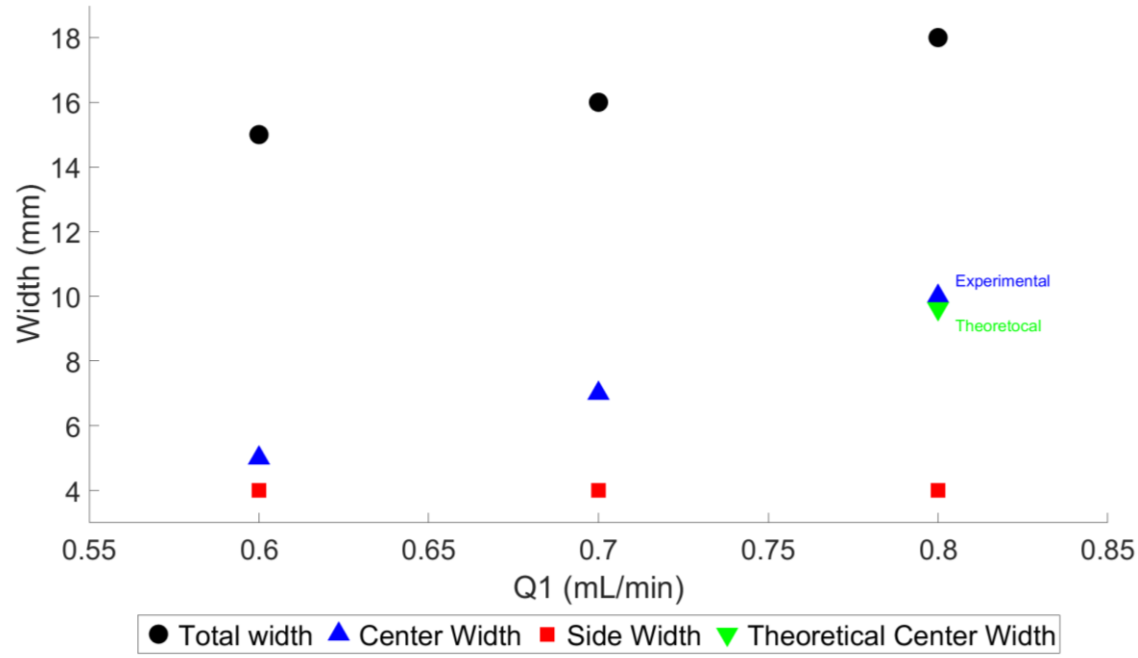

Figure 7.2 – Change in width of total, center and side coating areas when center flow rate is altered

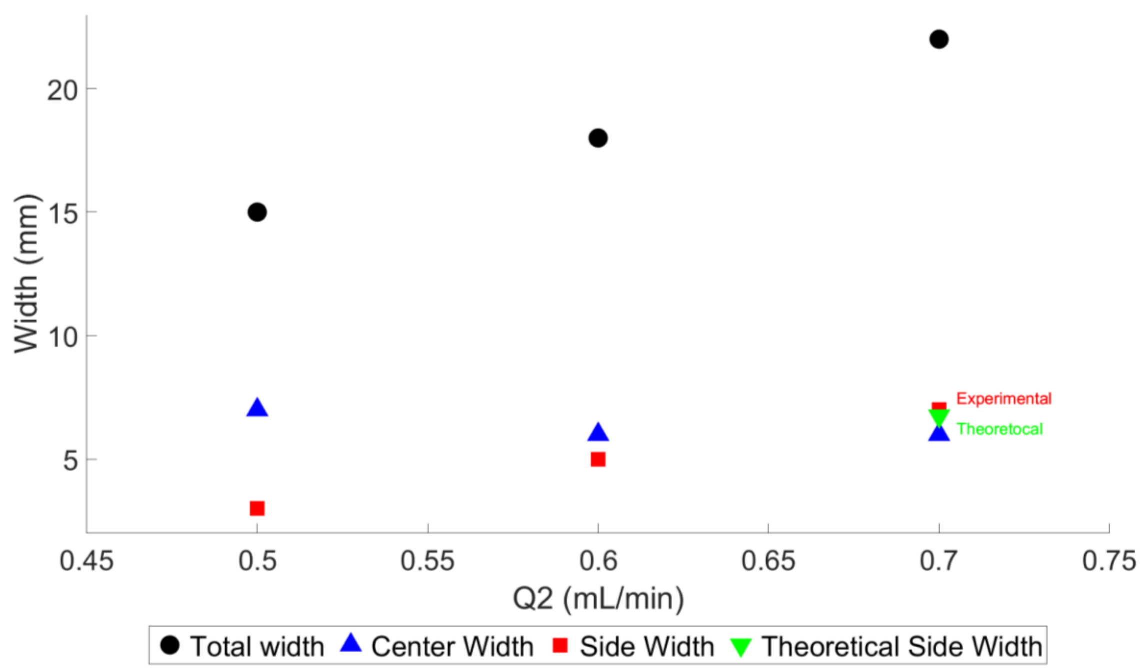

Figure 7.3 - Change in width of total, center and side coating areas when side flow rate is altered

Throughout the mathematical modeling, H and U values are consistent as 0.2 mm and 17 mm/s, respectively and only coating parameter that changes is the Q. Also, the L_d and L_u are consistent at 2 mm with G and w being 0.127 mm and 10 mm respectively as the slot die coater is rigid. From Table 2.1 and Table 2.2, μ, ρ and σ can be found. Q_1 and Q_2 used are shown in Table 7.1 where the flow rates would increase by 0.1 mL/min within the given range.

Table 7.1 – Flow rate combinations used for width analysis

Case	Center Fluid	Side Fluid	Q_1 (ml/min)	Q_2 (ml/min)
1	20 wt.% PVA	10 wt.% PVA	0.6 ~ 0.8	0.5
2	20 wt.% PVA	10 wt.% PVA	0.6	0.5 ~ 0.7

By implementing the given variables from Equation 7.8 ~ 7.11 for changing Q value, two piecewise equations for each case can be solved using the measured w values stated above. As result, Equation 7.12a and 7.12b are derived following their given conditions. For Case 1, the regression equation is shown in Equation 7.13 and Case 2 is shown in Equation 7.14.

$$w_1^* = 1.25 \cdot \ln\left(\Pi_a\right) + 4.55 \tag{7.13}$$

$$w_2^* = 1.11 \cdot \ln\left(\Pi_a\right) - 0.967 \tag{7.14}$$

Equation 7.12 shows the center width and Equation 7.13 shows the side width. To verify the two equations, one of the experimental results is used for each case as shown in Table 7.2. For Case 1, when the measured w is 10 mm, which w* is 1 and the theoretical w* is calculated to be 0.962 which can be calculated to w as 9.62 mm. The % error is calculated to be 3.95% higher than the expected value. For Case 2, when w is measured to be 7 mm and w* is 0.7, the theoretical w* is calculated to be 0.675 with w calculated to be 6.75 mm. The % error for experimental result was 3.70% higher than the theoretical.

Table 7.2 – Comparison of measured width and theoretical width

Case	**Location**	**Experimental Dimensionless Width (w*)**	**Theoretical Dimensionless Width (w*)**	**Error (%)**
1	Center	1	0.962	3.95
2	Side	0.7	0.675	3.70

CHAPTER 8. CONCLUSIONS

In this dissertation, a slot die mounted on R2R system was utilized to investigate the feasibility of scaling the fabrication of gradient thin films, based on the diffusion of fluids using microfluidics. Here, previous discoveries were used to examine the hypothesis of this dissertation. Experimental, computational and empirical investigations were performed to analyze flow in the internal cavity of the slot die and flow in the coating bead or deposition region as gradient thin film were formed.

Firstly, this dissertation analyzes the **internal mixing mechanism** in a planar geometry which Cubaud et al. has successfully shown in their work. Sudden introduction of microchannel can induce mixing as fluids flow through narrow channel in quick fashion. The Peclet Number (Pe) becomes critical in the calculation of the flow rates of the three inlets as well as the occurrence of diffusion. Although gradient structure formation has been successful using various flow channel patterns, planar geometry was specifically investigated as it deemed to have highest geometric similarity with slot die coating method. The flow channel is then transformed into 2D and 3D CAD model for CFD analysis as such computational simulation can act as a good precursor to the experimental result. Using the governing equation of ANSYS® Fluent, the two PVA materials with different concentrations (15 wt.% and 10 wt.%) were able to intermix with more viscous material entering the center and the less viscous material at the sides. From the derived result, the experimentation was continued with different combinations of PVA concentration with center always having the higher viscosity. The flow design implemented as a shim design that is enclosed by the two die blocks (upstream and downstream). Very thin PET sheet is precisely cut using a vinyl cutter connected to a designing computer software. Each combination of PVA/PVA concentration, the experimental results showed that apart from very viscous fluid combination, which was 20/15 wt.% PVA combination, internal mixing was noticed. The empirical formula also looked at the internal diffusion of two different fluids which specifically looked at the diffusion time and width to ensure the existence of gradient formation. Both calculations are dependent on channel width and diffusion coefficient of the fluidic material. The calculated values showed that at PVA and PEI materials take short time to diffuse into their conjugate materials but for PEDOT:PSS, the diffusion time is significantly longer. Therefore, it can be deduced that for PVA and PEI, the materials are diffusing into each other but for PEDOT:PSS, the PVA, which is the side fluid, is diffusing into the center fluid. Moreover, the width of mixing is dependent on the width of the flow and since the dimension of the microchannel is unchanged, it can be concluded that the width of diffusion is ~0.0236mm.

Secondly, this dissertation investigates the **flow behavior of the mixed inlet fluid through to the deposition phase** using experimental and empirical investigations. Experimentally, the gradient structure formed internally was not always maintained in the deposition phase. For the combinations of different PVA concentrations, any involvement of 5 wt.% PVA resulted in dripping, which distorted the overall dimension of the deposited film with premature mixing and wide spreading. The PEDOT:PSS/PVA combination also showed that gradient pattern was formed internally with calculated flow rates but at the deposition, erosion and overflow of center fluid were noticed. Looking at the empirical formula, the deposition of multi-striped flows follows the viscocapillary effect and pressure gradient to calculate the thickness of the resultant film. The calculation requires both the coating parameters and material properties, specifically coating gap (H), substrate speed (v), viscosity (μ) and surface tension (σ). The mass conservation at controlled volume is studied to calculate the widening effect of the deposition phase which uses the derived thickness (t) from above and the flow rate (Q). For example, the 20/10 wt.% gradient formation was calculated to have thickness of 0.008 mm at the side areas and 0.04 mm at the center area. Using an empirical approach, the equation for the width calculation can be driven which also follows the mass conservation and the surface interaction of the materials. The equation is used to predict the width of deposited coating at different inlet flow rates for both the center and the side flows. For example, the 20/10 wt.% gradient formation was calculated so that the % error for the center and side width were 3.95% and 3.70% respectively. Such method can be applied to many different combinations to verify the experimental results.

The third aspect this dissertation investigates is the **functionality of the gradient structure** in thin film form. Variety of characterization methods were utilized to investigate not only the functionality but also the existence of gradient structure. As mentioned, different materials were used as each material had their own advantages where PEDOT:PSS is a well-known electrically conductive material and PEI is a highly adhesive material. Electrical conductivity of the PEDOT:PSS/PVA gradient film is measured using the four-point probe method and it is noticed that the conductivity at the gradient structure is as efficient as 80% blended PEDOT:PSS to PVA solution. The adhesive tests between

PEI/PVA gradient structure and the PET substrate demonstrated that PVA, a material with poor adhesive properties, significantly improved in the adhesive property in gradient form with PEI. The adhesion was higher compared to the PEI and PVA fully blended coating. Using the FTIR method, the existence of gradient structure was analyzed. For PEDOT:PSS/PVA structure, the peaks measured at the gradient regions closer to PVA had more similar results to PVA peaks and gradient regions further from PVA had less similarity to PVA peaks. Moreover, the gradient structure, which had similar electrical conductivity to the 80% fully blended PEDOT:PSS/PVA ratio, had more peaks similar to PVA peaks compared to the fully blended coating. For PEI, the resulting peaks at the gradient region were in between the pure PEI and pure PVA peaks. Also, FTIR was also used to prove the high photodegradation nature of PEI material itself as PEI and different colored food dyes reacted by losing the color after time. Possible tooling for axial strain analysis is also introduced as it can visually inspect the region most vulnerable to strain stress. If this tool is utilized to gradient structures, it can be a good media to prove the usefulness of the gradient structure yet again.

In summary, the dissertation contained enough information to prove usefulness of the gradient structured film using a scalable coating method in many different fields. Creating mathematical precursors to the experimentation and proving the functionality of such structure were as important as experimentally fabricating gradated thin film structure. By utilizing this work, it can mass produce effective gradient structured thin films in efficient fashion for various industries and research fields.

CHAPTER 9. CONTRIBUTIONS AND OUTLOOK

9.1 Key Contribution

In this dissertation, the work is carried out to investigate the usage of a well-known scalable manufacturing method called slot die coating in continuous production of functional gradient patterned films. The strategy for fabricating such pattern inside the slot die coater and translating the exact pattern to the deposition is mandatory as such knowledge can decide the resultant film dimensions as well as the limitations of the method following the materials used. It is important to show the gradient patterned films not only experimentally, but also fundamentally. Moreover, the performance of the gradient structure, which in the past was proved to be a very efficient, is studied in many different aspects. The summary of this dissertation's contributions is listed below:

9.1.1 Experimental

- **Fabrication of gradient films** through a precisely calculated coating parameters can bring a lot of differences in many research fields. As very agile and scalable method was used, gradient film production can be used for many different fluidic materials that suit the user's demands.
    - **Experimental limitations of the method** can be overcome by adjustments in tooling and infrastructure which is heavily due to the highly scalable nature of the slot die coating method.

- **Mass production of gradated structured film** will be available with customizable resulting film dimensions with less material waste and time consumption.

- **Verification of functionally graded thin film,** as different functional materials were utilized to fabrication gradient patterned films.
    - **Electrically conductive polymer material** formed a gradient structure with a non-conducting polymer material and it is noted that the electrical conductivity measured over the gradient region has much efficient then blended materials.
    - **A very adhesive, cationic polymer material** also forms a gradient structure with a non-adhesive, non-ionic polymer. The gradient structured film improved the adhesive force compared to completely blended film.

9.1.2 Fundamental

- **Flow rates of the three flow inlets are mathematically calculated** using the range of Pe which would induce diffusion of the fluidic materials through the microchannel.
    - **For different combinations of the fluids**, different ranges of flow rates were derived as the calculations are heavily dependent on the viscosity ratio between the two materials and the diffusion coefficients.
    - Theoretically, any flow rate combinations outside the Pe ranges result in distorted film patterns mostly at the deposition phase. Although the

correct flow rate ranges show that the diffusion occurs internally in the die cavity, experimentally, due to the assumptions and human errors, the gradient formation is not followed through. **However, as internal mixing is noticed, the mathematical derivation stands.**

- **Investigation in mathematical derivation of internal mixing** can be a critical proof of diffusion since the internal mixing mostly focuses on the diffusing time and the diffusing width. At high diffusion time, it can be inferred that the fluids are not being diffused into each other but if the diffusion time is lower than the overall time for fluids to fully develop, it can be inferred that diffusion has occurred.
- **Carrying out the internal results to the deposition phase**, mathematical formulas can be used to predict the overall wet thickness and the widening effect of the film based on the coating parameters and the material properties. Such calculations are based on non-diffusing homogeneous coatings, which creates the error between the analytical and experimental results.
- **CFD results** also suggests the internal mixing phenomenon can be also shown with the known governing equations embedded in the software. Connecting the empirical and computational results, the experimental results can be easily backed up.

9.2 Future Work

There are still some areas in this work that could be stretched to even strengthen the feasibility of the gradient structure. As mentioned in the dissertation, DP method can easily visualize the regions most vulnerable to axial stress, especially for thin films. Adding on to the Tape Adhesion Test, it can be a great method for comparing the maximum axial stress of plain material thin films and the gradient structured thin film with existence of emulated flexible electronics. Adding on to that, the UV-vis Spectrophotometer that was used to quantitively characterize the gradient structure can be further studied to investigate percentage composition of the overall film. This can be analyzed by measuring thinner, pure colored samples and use those as calibration.

Usage of biodegradable oxygen barrier is another functional gradient structure that can be explored for its usage. Chitin Nanofiber (ChNF) is the notable material which has the ability to create an oxygen barrier layer when thinly coated[136137] but since it is not easy to process, the concentration remains very low. This is problematic in terms of coating as the material itself is very close to viscosity of water which dewets from the surface. However, following the results that if the highly wetting materials enclose the poorly wetting materials, the coating becomes available. ChNF and PVA blends have been proved to have high mechanical properties and by creating a gradient patterned film using the two materials, a strong oxygen barrier layer can be fabricated and looking at the results from this dissertation, the oxygen barrier property at the gradient region could possibly be further improved. Besides ChNF, different functionally gradient structure can definitely be fabricated using different materials not just for its structural integrity, but just for the heterogenous surface in applications like instantaneous material mixing. Not just the fluidic materials, the substrate can be changed to other functional materials. The large roll of material that creates the carrier web, which in this dissertation is set to PET, can be changed to a roll of different substrates to help certain functional fluidic materials to be coated.

The investigation of the CFD analysis at the deposition is another area the that can be improved in this work. The resultant data from the internal CFD analysis and set as the inlet of the deposition geometry so that the two calculations can be calculated. Unmentioned attempts were made in dissertation, but special user defined equations were required to consider the wetting behavior of the fluids which, in 3D geometry multiphase VOF analysis, takes considerable time for the analysis. If this is possible, the defects noticed at the deposition phase and the dimensions of the resultant films can be predicted prior to the actual experimentation. Moreover, it is important to address the different factors that affect the gradient formation as the fluid flows through the microchannel. Different variables such as viscosity, flow rate, etc. can be analyzed using the CFD models to further understand the mechanism of the mixing.

As slot die coater mounted on R2R is a very versatile manufacturing method in terms of scalability, the size of the gradient can be easily varied. However, prior calculations and simulations are mandatory to avoid any defects like internal dead zones, dripping and air entrainment. This would allow for having different sizes of the gradient structures, which would require studying the internal flow geometries. It is believed that increasing the deposition width will cause dead zones in each wide channel and decreasing the deposition will cause severe leakage of the fluids. Moreover, by improving the overall tooling, the internal leakage that occurs in between the die blocks and the shim need to be amended to improve the stability of the coating and reduce the errors between the mathematical and experimental data.

The most interesting phenomenon that still needs to be resolved is the wetting of the fluids with poor wetting properties like PEDOT:PSS and PEI when the fluid is enclosed by material with high wettability like PVA. The science behind this will be crucial in field of coating and wetting as if the good wetting material can act as a sacrificial layer to coat the non-wetting materials. The two materials being coated do not have to be diffused into each other. Also, if such phenomenon is proved to work for any types of fluidic materials, then it can eradicate one of the biggest downsides in slot die coating. This method will be much cost efficient than using surface treatment tools like corona treatment and UV treatment. However, the limits to the materials need to be specified as not all materials would be following this phenomenon.

REFERENCES

[1] N. Naserifar, P. LeDuc, and G. Fedder, "Material Gradients in Stretchable Substrates toward integrated Electronic Functionality", Advanced Materials, vol. 28, iss. 18, 2016

[2] Y. Xu, Y. Yang, D-X. Yan, H. Duan, G. Zhao and Y. Liu, "Gradient Structure Design of Flexible Waterborne Polyurethane Conductive Films for Ultraefficient Electromagnetic Shielding with Low Reflection Characteristic", ACS Applied Materials and Interfaces, vol. 10, iss. 22, pp. 19143-19152, 2018

[3] K. Estelle, D. Blair, K. Evans and B. Gozen, "Manufacturing of smart composites with hyperelastic property gradients and shape memory using fused deposition", Journal of Manufacturing Processes, vol. 28, iss. 3, pp. 500-507, 2017

[4] B. Baker, B. Trappmann, S. Stapleton, E. Toro, and C. Chem, "Microfluidics embedded within extracellular matrix to define vascular architectures and pattern diffusive gradients", Royal Society of Chemistry Lab on a Chip, iss. 16, 2013

[5] K. Estelle, D. Blair, K. Evans and B. Gozen, "Manufacturing of smart composites with hyperelastic property gradients and shape memory using fused deposition", Journal of Manufacturing Processes, vol. 28, iss. 3, pp. 500-507, 2017

[6] J.H. Kim, et al., “Temperature Gradient-Driven Multilevel and Grayscale Patterning of Tosylate-Doped Poly(3,4-Ethylenedioxythiophene) Films for Flexible and Functional Electronics”, *Advanced Materials Technologies,* vol. 6, iss. 10, 2100613, 2021

[7] K. De France, T. Hoare, and E. Cranston, “Review of Hydrogels and Aerogels Containing Nanocellulose”, ACS Chemistry of Materials, vol. 29, pp. 4609-4631, 2017

[8] Z. Lei, D. Tian, X. Liu, J. Wei, K. Rajavel, T. Zhao, Y. Hu, P. Zhu R. Sun, C-P. Wong, “Electrically conductive gradient structure design of thermoplastic polyurethane composite foams for efficient electromagnetic interference shielding and ultra-low microwave reflectivity”, *Chemical Engineering Journal*, vol. 424, 130365, 2021

[9] S-H, Hong, D-H. Jung, J-H. Kim, Y-H, Lee, S-J. Cho, S. Joo, H-W. Lee, K-S. Lee, S-Y. Lee, “Electrical Conductivity Gradient Based on Heterofibrous Scaffolds for Stable Lithium-Metal Batteries”, *Advanced Functional Materials*, vol. 30, iss. 14, 1908868, 2020

[10] X. Sun, X. Zhao, L. Ye, “Construction of gradient structure in polyetherimide/carbon nanotube nanocomposite foam and its thermal/mechanical property”, *Composites Part A: Applied Science and Manufacturing*, vol. 126, 105579, 2019

[11] W. Lu, F. Li, Y. Zhou, S. Liu, K. Wang, Q. Wang, “Effect of high hardness and adhesion of gradient TiAlSiN coating on cutting performance of titanium alloy”, *Journal of Alloys and Compounds*, vol. 820, 153137, 2020

[12] X.L. Wu, P. Jiang, L. Chen, F. Zhang, F.P. Yuan, Y.T. Zhu, "Synergetic Strengthening by Gradient Structure", *Materials Research Letters*, vol. 2, iss. 4, 2014

[13] X. Yang, X. Ma, J. Moering, H. Zhou, W. Wang, Y. Gong, J. Tao, Y. Zhu, X. Zhu, "Influence of gradient structure volume fraction on the mechanical properties of pure copper", *Materials Science and Engineering: A*, vol. 645, pp. 280-285, 2015

[14] J. Jiang, Z. Shen, X. Cai, J. Qian, Z. Dan, Y. Lin, B. Liu, C-W. Nan, L. Chen, Y. Shen, "Polymer Nanocomposites with Interpenetrating Gradient Structure Exhibiting Ultrahigh Discharge Efficiency and Energy Density", *Advanced Energy Materials*, vol.9, iss. 15, 1803411, 2019

[15] Y. Wang, D. Su, H. Ji, X. Li, "Gradient structure high emissivity MoSi2-SiO2-SiOC coating for thermal protective application", *Journal Alloys and Compounds*, vol. 703, iss. 5, pp. 437-447, 2017

[16] Y. Yoshioka, P. Clavert and G. Jabbour, "Simple Modification of Sheet Resistivity of Conducting Polymeric Anodes via Combinatorial Ink-Jet Printing Techniques", Macromolecular Rapid Communications, vol. 26, iss. 4, 2005

[17] A. de ninno, A. Gerardino, B. Girarda, G. Grenci, L. Businaro, "Top-Down approach to nanotechnology for cell-on-chip applications", Biophysics and Bioengineering Letters, vol. 3, 2010

[18] M-X. Zhao, J. Li and X. Gao, “Gradient Coating of Polydopamine via CDR”, ACS Langmuir, vol 33, iss. 27, pp. 6727-6731, 2017

[19] R. Diehm, et al., “In Situ Investigations of Simultaneous Two-Layer Slot Die Coating of Component-Graded Anodes for Improved High-Energy Li-Ion Batteries”, *Energy Technology*, vol. 8, iss. 5, 1901251, 2020

[20] B. S. Yilbas, A. Al-Sharafi, H. Ali, “Chapter 3 – Surfaces for Self-Cleaning”, *Self-Cleaning of Surfaces and Water Droplet Mobility*, pp. 45-98, 2019

[21] X. Lin, J. Kavalakkatt, M. Ch. Lux-Steiner, A. Ennaoui, “Inkjet-Printed Cu2ZnSn(S, Se)$_4$ Solar Cells”, *Advanced Science*, vol. 2, iss. 6, 1500028, 2015

[22] T. Jian, E. J. Carbone, K. W-H. Lo, C. T. Laurencin, “Electrospinning of polymer nanofibers for tissue regeneration”, *Progress in Polymer Science,* vol. 46, pp.1-24, 2015

[23] Y. Zhang, et al., “Tuning the gradient structure of highly breathable, permeable, directional water transport in bi-layered Janus fibrous membranes using electrospinning”, *RCS Advanced*, vol. 10, pp. 3259-3538, 2020

[24] H. Zhu, et al., “Gradient structure based dual-robust superhydrophobic surfaces with high-adhesive force”, *Applied Surface Science*, vol. 463, iss. 1, pp. 427-434, 2019

[25] T. Carey, C. Jones, F. Le Moal, D. Deganello, F. Torrisi, “Spray-Coating Thin Films on Three-Dimensional Surfaces for a Semitransparent Capacitive-Touch Device”, *ACS Applied Material Interfaces,* vol. 10, iss. 23, pp. 19948-19956, 2018

[26] J. Karthikeyan, “The advantages and disadvantages of the cold spray coating process”, *The Cold Spray Materials Deposition Process*, pp. 62-71, 2007

[27] A. Parsekian and T.A.L. Harris, “Scalable, Alternating Narrow Stripes of Polyvinyl Alcohol Support and Unmodified PEDOT:PSS with Maintained Conductivity Using a Single-Step Slot Die Coating Approach”, *ACS Applied Materials and Interfaces*, vol. 12, iss. 3, pp. 3736-3745, 2020

[28] N-T. Nguyen, “Micromixers: Fundamentals, Design and Fabrication, A volume in Micro and Nano Technologies”, 2nd ed., William Andrew Publishing, Ch. 4, 2012

[29] R. G. Larson, T. J. Rehg, “Spin Coating”, *Liquid Film Coating*, pp.709-734, 1997

[30] N. Sahu, B. Parija, S. Panigrahi, “Fundamental understanding and modeling of spin coating

process : A review”, *Indian Journal of Physics*, vol. 83, iss. 4, pp. 493-502, 2009

[31] M. Shibata, Y. Sakai, D. Yokoyama, “Advantages and disadvantages of vacuum-deposited and spin-coated amorphous organic semiconductor films for organic light-emitting diodes”, *Journal of Materials Chemistry C,* vol. 3, pp. 11178-11191, 2015

[32] T. Kawase, T. Shimoda, C. Newsome, H. Sirringhaus, R. H. Friend, "Inkjet printing of polymer thin film transistors", *Thin Solid Films*, vol. 438, iss. 22, pp. 279-287, 2003

[33] E. Tekin, P. J. Smith, U. S. Schubert, "Inkjet printing as a deposition and patterning tool for polymers and inorganic particles", *Soft Materials*, vol. 4, pp. 703-713, 2008

[34] M. Singh, H. M. Haverinen, P. Dhagat and G. E. Jabbour, "Inkjet Printing—Process and Its Applications", *Advanced Materials*, vol. 22, pp. 673-685, 2010

[35] Z. Qi, et al., "3D-Printed, Superelastic Polypyrrole–Graphene Electrodes with Ultrahigh Areal Capacitance for Electrochemical Energy Storage", *Advanced Materials Technologies*, vol. 3, iss. 7, 1800032, 2018

[36] M. D. Levenson, N. S. Viswanathan, R. A. Simpson, "Improving resolution in photolithography with a phase-shifting mask", *IEEE Transactions on Electron Devices*, vol. 29, no. 12, pp. 1828-1836, 1982

[37] N. Liaros, J. T. Fourkas, "Ten years of two-color photolithography", *Optical Materials Express*, vol. 9, iss. 7, pp. 3006-3020, 2019

[38] J. Li, P. Zrazhevskiy, X. Gao, "Eliminating Size-Associated Diffusion Constraints for Rapid On-Surface Bioassays with Nanoparticle Probes", *Small*, vol. 12, no. 8, pp.1035-1043, 2016

[39] Beguin AE, Inventor. Method of coating strip material. US patent No. 2,681,6941954

[40] F-H. Lin, C-M. Liu, T-J. Liu and P-Y. Wu, "Experimental Study on Tensioned-Web Slot Coating", *Polymer Engineering and Science,* vol. 47, iss. 6, pp. 841-851, 2007

[41] X. Ding, J. Liu and T.A.L. Harris, "A review of the operating limits in slot die coating process", *AlChE Journal Review Article: Transport Phenomena and Fluid Mechanics*, vol.62, iss. 7, pp. 2508-2524, 2016

[42] J. Nam and M. Carvalho, "Two-layer tensioned-web-over-slot die coating: Effect of operating conditions on coating window", *Chemical Engineering Science*, vol. 65, iss. 13, pp. 4056-4079, 2010

[43] A. Parsekian, T.A.L. Harris, "Extrusion on-demand pattern coating using a hybrid manufacturing process", *Chemical Engineering and Processing – Process Intensification*, vol. 109, pp. 20-31, 2016

[44] A. W. Parsekian, "Solution Processing of Stripes, Patches and Digital Patterns Using a Novel Slot Die Coating-Inspired Approach", *Georgia Institute of Technology*, 2020

[45] Z. Yang, S. Matsumoto, H. Goto, M. Matsumoto and R. Maeda, "Ultrasonic micromixer for microfluidic systems", Sensors and Actuators A: Physical, vol 93, iss. 3, pp. 266-272, 2001

[46] J-H. Tsai and L. Lin, "Active microfluidic mixer and gas bubble filter driven by thermal bubble micropump". Sensors and Actuators A: Physical, vol. 97-98, pp. 665-671, 2002

[47] B. Xu, T. Wong, N-T. Nguyen, Z. Che and J. Chai, “Thermal mixing of two miscible fluids in a T-shaped microchannel”, AIP Biomicrofluidics, vol. 4, iss. 4, 2010

[48] K. S. Ryu, K. Shaikh, E. Goluch, Z. Fan, C. Liu, “Micro magnetic stir-bar mixer integrated with parylene microfluidic channels”, Lab on a Chip, vol. 4, iss. 6, pp. 608-613, 2004

[49] N. Pamme, “Magnetism and microfluidics”, Lab on a Chip, iss. 1, 2006

[50] P. Yuen, G. Li, Y. Bao and U. Muller, “Microfluidic devices for fluidic circulation and mixing improve hybridization signal intensity on DNA arrays”, Lab on a Chip, vol. 3, iss. 1, pp. 46-50, 2003

[51] A. Kamholz and P. Yager, “Theoretical Analysis of Molecular Diffusion in Pressure-Driven Laminar Flow in Microfluidic Channels”, Biophysical Journal, vol. 80, iss. 1, pp. 155-160, 2001

[52] M. Holden, S. Kumar, E. Castellana, A. Beskok and P. Cremer, “Generating fixed concentration arrays in a microfluidic device”, Sensors and Actuators B: Chemical, vol. 92, iss. 1-2, pp. 199-207, 2003

[53] N. Jeon, S. Dertinger, D. Chiu, I. Choi, A. Stroock and G. Whitesides, “Generation of Solution and Surface Gradients Using Microfluidic Systems”, ACS Langmuir, vol. 16, iss 22. pp. 8311-8316, 2000

[54] D. Irmia, D. Geba and M. Toner, “Universal Microfluidic Gradient Generator”, ACS Analytical Chemistry, vol. 78, iss. 10, pp. 3472-3477, 2006

[55] J. Fan, S. Li, Z. Wu, Z. Chen, “Chapter 3 - Diffusion and mixing in microfluidic devices”, *Microfluidics for Pharmaceutical Applications,* pp. 79-100, 2019

[56] T. Cubaud, and T. Mason, “Folding of Viscous Threads in Diverging Microchannels”, Physical Review Letters, vol. 96, iss. 11, 2006

[57] T. Cubaud, and T. Mason, “Formation of miscible fluid microstructures by hydrodynamic focusing in plane geometries”, Physical Review E, vol. 78, iss. 5, 2008

[58] S. Dixit, A. Kumar, S. Kumar, N. Waghmare, H. Thakur, S. Khan, “CFD analysis of biodiesel blends and combustion using Ansys Fluent”, *Materials Today: Proceedings*, vol. 26, pp. 665-670, 2020

[59] R. Baghel, S. Kalla, S. Updhyaya, S.P. Chauraisa, K. Singh, “CFD modeling of vacuum membrane distillation for removal of Naphthol blue black dye from aqueous solution using COMSOL Multiphysics”, *Chemical Engineering Research and Design,* vol. 158, pp. 77-88, 2020

[60] A. Nguyen, G. Evans, “Computational fluid dynamics modelling of gas jets impinging onto liquid pools”, *Applied Mathematical Modelling*, vol. 30, iss. 11, pp. 1472-1484, 2006

[61] B.G.M. van Wachem, A.E. Almstedt, "Methods for multiphase computational fluid dynamics", *Chemical Engineering Journal*, vol. 96, iss. 1-3, pp. 81-89, 2003

[62] H. Zhang, W. Williams-Dalson, E. Keshavarz-Moore, P. Shamlou, "Computational-fluid-dynamics (CFD) analysis of mixing and gas–liquid mass transfer in shake flasks", *Biotechnology and Applied Biochemistry*, vol. 41, iss. 1, 2010

[63] C-C. Hong, J-W. Choi and C. Ahn, "A novel in-plane passive microfluidic mixer with modified Tesla structures", Royal Society of Chemistry Lab Chip, vol. 4, pp. 109-113, 2004

[64] K. Bhamidipati, S. Didari, P. Bedell and T.A.L. Harris, "Wetting phenomena during processing of high-viscosity shear-thinning fluid", *Journal of Non-Newtonian Fluid Mechanics*, vol. 166, pp. 12-13, pp. 723-733, 2011

[65] S. Annam N. Bontoux, H. Stone, "Formation of dispersions using "flow focusing" in microchannels", *Applied Physics Letters*, vol. 82, iss.3, pp. 364-366, 2003

[66] C.Y. Lim, Y. C. Lam, C. Yang, "Mixing enhancement in microfluidic channel with a constriction under periodic electro-osmotic flow", *Biomicrofluidics*, vol. 4, iss. 1, 014101, 2010

[67] C. G. Caro, T. J. Pedley, R.C. Schroter, W. A. Seed, "The Mechanics of the Circulation, Chapter 5", *Oxford University Press*, 1978

[68] Mowiol: Polyvinyl alcohol. Clariant GmbH, Sulzbach (1999)

[69] A. Soleimani-Gorgani, “Printing on Polymers, Fundamentals and Applications”, pp. 231-246, 2016

[70] R. Good, “Contact angle, wetting and adhesion: a critical review”, *Journal of Adhesion Science and Technology,* vol. 6, iss. 12, 1992

[71] D.Y. Kwok, and A.W. Neumann, “Contact angle measurement and contact angle interpretation”, Advances in Colloid and Interface Science, vol. 81, iss. 3, pp. 167-249, 1999

[72] Microfluidics: Modelling, Mechanics and Mathematics, Bastian E. Rapp (2017)

[73] W. Tyson, W. Miller, “Surface free energies of solid metals: Estimation from liquid surface tension measurements”, *Surface Science*, vol. 62, iss. 1, pp. 267-276, 1977

[74]Microfluidics: Modelling, Mechanics and Mathematics, Bastian E. Rapp (2017)

[75] A. Pelofsky, “Surface Tension-Viscosity Relation for Liquids”, *Journal of Chemical and Engineering Data*, vol. 11, no. 3, pp. 394-397, 1966

[76] F.M. Smits, “Measurement of Sheet Resistivities with the Four-Point Probe”, *Bell System Technical Journal*, vol. 37, iss. 3, 1958

[77] A. P. Schuetze, “A laboratory on the four-point probe technique”, *American Journal of Physics,* vol. 82, iss. 2, pp. 149, 2004

[78] M. Huysmans, A. Dassargues, “Review of the use of Péclet numbers to determine the relative importance of advection and diffusion in low permeability environments”, *Hydrogeology Journal,* vol. 13, pp. 895-904, 2005

[79] J. T. Adeosun, A. Lawal, “Numerical and experimental studies of mixing characteristics in a T-junction microchannel using residence-time distribution”, *Chemical Engineering Science,* vol. 64, iss. 10, pp. 2422-2432, 2009

[80] O. Kaspar et al., “Influence of channel height on mixing efficiency and synthesis of iron oxide nanoparticles using droplet-based microfluidics”, RCS Advanced, vol. 10, pp. 15179-15189, 2020

[81] K-J. Choi, J-Y. Lee, J. Park, Y-S. Seo, “Multilayer slot-die coating of large-area organic light-emitting diodes”, vol. 26, pp. 66-74, 2015

[82] C. Galaup et al., “Blue wine, a color obtained with synthetic blue dye addition: two case studies”, *European Food Research and Technology,* vol, 245, pp. 1777-1782, 2019

[83] S. Kohl, J. Landmark, D. Stickle, “Demonstration of Absorbance Using Digital Color Image Analysis and Colored Solutions”, *Journal of Chemical Education*, vol. 83, no. 4, pp. 644-646, 2006

[84] G-E. Kim et al., “Effect of surface morphology of slot-die heads on roll-to-roll coatings of fine PEDOT:PSS stripes”, *Organic Electronics*, vol. 66, pp. 116-125, 2019

[85] J. Lee, X. Li, J. Park, “Suppression of Capillary Flow in Slot-Die Coating for the Fabrication of Fine OLED Stripe”, *IEEE Transactions on Electron Devices*, vol. 66, no. 12, pp. 5221-5229, 2019

[86] L.Dietsche, P. Lee, J. Dooley, “CFD-Based Optimization Methods Applied to Polymer Die Design”, *The 15th World Multi-Conference on Systemics, Cybernetics and Informatics*, pp. 130-135. 2011.

[87] Fluent, I., 2012, "User Guide Fluent 12.0.," Lebanon, NH.

[88] X. Wu, P. Jiang, L. Chen, Y.T. Zhu, “Extraordinary strain hardening by gradient structure”, *Applied Physical Science*, vol. 111, no. 20, pp. 7197-7201, 2014

[89] L-H. Zhao et al., “Simultaneously improved thermal conductivity and mechanical properties of boron nitride nanosheets/aramid nanofiber films by constructing multilayer gradient structure”, *Composites Part B: Engineering*, vol. 229, iss. 15, 109454, 2022

[90] Y. Zhang et al., “PVDF-Based Dielectric Composite Films with Excellent Energy Storage Performances by Design of Nanofibers Composition Gradient Structure”, *ACS Applied Energy Material*, vol. 1, iss. 11, pp. 6320-6329

[91] J. Yang, et al., “Gradient structure design of lightweight and flexible silicone rubber nanocomposite foam for efficient electromagnetic interference shielding”, *Chemical Engineering Journal*, vol. 390, iss. 15, 124589, 2020

[92] L. Zhu, G. He, Y. Long, B. Yang, J. Lv, “Eco-Friendly, Water-Induced In2O3 Thin Films for High-Performance Thin-Film Transistors and Inverters”, *IEEE Transactions on Electron Devices*, vol. 65, iss.7, 2018

[93] J.T. Ok, et al., “Water-resistant AgBiS2 colloidal nanocrystal solids for eco-friendly thin film photovoltaics”, *Nanoscale*, vol. 11, pp. 9633-9640, 2019

[94] Z. Yu, Y. Ji, V. Bourg, M. Bilgen, J. C. Meredith, “Chitin- and cellulose-based sustainable barrier materials: a review”, *Emergent Materials*, vol. 3, pp. 919-936, 2020

[95] N. Satoh, M. Otsuka, T. Ohki, A. Ohi, Y. Sakurai, Y. Yamashita, and T. Mori, “Organic π-type thermoelectric module supported by photolithographic mold: a working hypothesis of sticky thermoelectric materials”, *Science and Technology of Advanced Materials*, vol. 19, iss. 1, pp. 517-525, 2018

[96] M. Cinquino et al., “Effect of surface tension and drying time on inkjet-printed PEDOT:PSS for ITO-free OLED devices”, *Journal of Science: Advanced Materials and Devices*, vol. 7, iss. 1, 100394, 2022

[97] C. Dong, X. Yuan, M. He, K. Yao, "Preparation of PVA/PEI ultra-fine fibers and their composite membrane with PLA by electrospinning." Journal of biomaterials science. Polymer edition, vol. 17, pp. 631-43, 2006

[98] C. Ehrhardt, M. Schmolke, A. Matzke, A. Knoblauch, C. Will, V. Wixler, S. Ludwig, "Polyethylenimine, a cost-effective transfection reagent", *Signal Transduction,* vol. 6, iss. 3, pp. 179-184, 2006

[99] Y.Yang et al., "Polyethylenimine coating to produce serum-resistant baculoviral vectors for in vivo gene delivery", *Biomaterials*, vol. 30, iss. 29, pp. 5767-5774, 2009

[100] Y. Zhou et al., "A Universal Method to Produce Low–Work Function Electrodes for Organic Electronics", *Science,* vol. 336, no. 6079, pp. 327-332, 2012

[101] N. Akhtar, "Gelatin-polyethylenimine composite as a functional binder for highly stable lithium-sulfur batteries", *Electrochimica Acta*, vol. 282, pp. 758-766, 2018

[102] S. Choi, M. L. Gray, C. W. Jones, "Amine-Tethered Solid Adsorbents Coupling High Adsorption Capacity and Regenerability for CO2 Capture From Ambient Air", *Chemistry Europe,* vol. 4, iss. 5, pp. 628-635, 2011

[103] Y. Yuan, M. H. Guo, F. Y. Liu, "Preparation and Evaluation of Green Composites Using Modified Ammonium Lignosulfonate and Polyethylenimine as a Binder", *BioResources*, vol. 9, no. 1, pp. 836-848, 2014

[104] I. Verbove et al., “Ultrasonic spray coating of polyethylenimine (ethoxylated) as electron injection and transport layer for organic light emitting diodes: The influence of layer morphology and thickness on the interface physics between polyethylenimine (ethoxylated) and the Al cathode”, *Nano Select*, vol 3, iss.4, pp. 851-863, 2022

[105] J.H. Kim et al., “Electrospun nanofibers composed of poly(ε-caprolactone) and polyethylenimine for tissue engineering applications”, *Material Science and Engineering: C*, vol. 29, iss. 5, pp. 1725-1731, 2009

[106] Epomin® Polyment, Nippon Shokubai Co.LTD

[107] J. Ortiz-Bustos, M. Fajardo, I. del Hierro, Y. Perez, “Versatile titanium dioxide nanoparticles prepared by surface-grown polymerization of polyethylenimine for photodegradation and catalytic C-C bond forming reactions”, *Molecular Catalysis*, vol. 475, 110501, 2019

[108] J.W. Buck, J.H. Andrews, “Localized, Positive Charge Mediates Adhesion of Rhodosporidium toruloides to Barley Leaves and Polystyrene”, *Applied Environmental Microbiology*, vol. 65, iss. 5, pp. 2179-2183, 1999

[109] F.M. Smits, “Measurement of Sheet Resistivities with the Four-Point Probe”, *Bell System Technical Journal*, vol. 37, iss. 3, 1958

[110] A. P. Schuetze, “A laboratory on the four-point probe technique”, *American Journal of Physics,* vol. 82, iss. 2, pp. 149, 2004

[111] H. Shi, C. Liu, Q. Jiang, J. Xu, “Effective Approaches to Improve the Electrical Conductivity of PEDOT:PSS: A Review”, *Advance Electronic Materials,* vol. 1, iss. 4, 2015

[112] C. Dong, X. Yuan, M. He, K. Yao, “Preparation of PVA/PEI ultra-fine fibers and their composite membrane with PLA by electrospinning.” *Journal of biomaterials science. Polymer edition,* vol. 17, pp. 631-43, 2006

[113] Y-F. Zhang et al., “Flexible, stretchable and conductive PVA/PEDOT:PSS composite hydrogels prepared by SIPN strategy”, *Polymer Testing,* vol. 81, 106213, 2020

[114] N. Liu, G. Fang, J. Wan, H. Zhou, H. Long, X. Zhao, “Electrospun PEDOT:PSS–PVA nanofiber based ultrahigh-strain sensors with controllable electrical conductivity”, *Journal of Materials Chemistry,* vol. 21, iss. 47, pp. 18962-18966, 2011

[115] M. Reyes-Reyes, I. Cruz-Cruz, R. Lopez-Sandoval, “Enhancement of the Electrical Conductivity in PEDOT:PSS Films by the Addition of Dimethyl Sulfate”, *Journal of Physical Chemistry C,* vol. 114, iss. 47, pp. 20220-20224, 2010

[116] Y. Wang et al., “Biscarbamate cross-linked polyethylenimine derivative with low molecular weight, low cytotoxicity, and high efficiency for gene delivery”, *Int J Nanomedicine,* vol. 7, pp. 693-704, 2012

[117] O. van der Sluids, R.A.B. Engelen, P.H.M. Timmermans, and G.Q. Zhang, Microelectron Reliab, 49, 853 (2009)

[118] D. Vella, J. Bico, A. Boudaoud, B. Roman, and P. Reid, P Natl Acad Sci USA, 106, 10901 (2009)

[119] U. Welzel, J. Ligot, P. Lamparter, A. C. Vermeulen, and E. J. Mittemeijer, J Appl Crystallogr, 38, 1 (2005)

[120] K. Ramesh, Meas Sci Technol, 11, 12 (2000)

[121] R.G.R. Prasath, S. Danyluk, and S. Zagarola, Polym-Plast Technol Mater, 58, 1802 (2019)

[122] R.G.R. Prasath, T. Newton, and S. Danyluk, Mfg Let, 15, 9 (2018)

[123] R.G.R. Prasath, K. Skenes, and S. Danyluk, J Electron Mater, 42, 2478 (2013)

[124] M. Kempe, Sol Energ Mat Sol C, 94, 246 (2010)

[125] D. Perera, “On adhesion and stress in organic coatings”, *Progress in Organic Coatings*, vol. 28, pp. 21-23, 1996

[126] Z. Wei, X. Xu, "Gradient design of bio-inspired nacre-like composites for improved impact resistance", *Composites Part B: Engineering*, vol. 215, iss. 15, 108830, 2021

[127] J. M. Ottino, S. Wiggins, "Introduction: mixing in microfluidics", *Phil. Trans. R. Soc. Lond. A*, vol. 362, pp. 923–935, 2004

[128] P. K. Sahu, A. Golia, A. K. Sen, "Analytical, numerical and experimental investigations of mixing fluids in microchannel", *Microsystem Technologies*, vol. 18, pp. 823-832, 2012

[129] L. Zhanshayeva, V. Favaron, F. Lubineau, "Macroscopic Modeling of Water Uptake Behavior of PEDOT:PSS Films", *ACS Omega,* vol. 4, iss. 26, pp. 21883-21890, 2019

[130] T. A. Beu, A. Farcas, "Structure and dynamics of solvated polyethylenimine chains", *AIP Conference Proceedings*, 020001, 2017

[131] A. W. Parsekian, T.-J. Jeong, T. A. L. Harris, "A process model for slot coating of narrow stripes", *Journal of Coatings Technology and Research*, iss. 16, pp. 1653-1661, 2019

[132] H. Kang, J. Park, K. Shin, "Statistical analysis for the manufacturing of multi-strip patterns by roll-to-roll single slot-die systems", *Robotics and Computer-Integrated Manufacturing*, vol. 30, iss. 4, pp. 363-368, 2014

[133] L. Landau, B. Levich, "Dragging of a Liquid by a Moving Plate", *Dynamics of Curved Fronts,* pp. 141-153, 1988

[134] W-J. Yu, T-J. Liu, T-A. Yu, "Reduction of the minimum wet thickness in extrusion slot coating", *Chemical Engineering Science*, vol. 50, iss. 6, pp. 917-920, 1995

[135] S. J. Le, H. J. Koh, B. K. Ryu, S. J. Kim, H. W. Jung, J. C. Hyun, "Operability coating windows and frequency response in slot coating flows from a viscocapillary model", *Chemical Engineering Science*, vol. 66, iss. 21, pp. 4953-4959, 2011

[136] C. W. Irvin, C. C. Stam, J. C. Meredith, M. L. Shofner, "Mechanical reinforcement and thermal properties of PVA tricomponent nanocomposites with chitin nanofibers and cellulose nanocrystals", *Composites Part A: Applied Science and Manufacturing*, vol. 116, pp. 147-157, 2019

[137] C.C. Stam, C. W. Irvin, C. J. Coffey, R. K. Geran, R. Ibarra-Rivera, M. L. Shofner, J. C. Meredith, "Controlling Barrier and Mechanical Properties of Cellulose Nanocrystals by Blending with Chitin Nanofibers", *Biomacromolecules*, vol. 21, iss. 2, pp. 545-555, 2019